MEASUREMENT OF THE NEUTRON BETA DECAY LIFETIME USING MAGNETICALLY TRAPPED ULTRACOLD NEUTRONS

Evan Robert Adamek

ProQuest Number: 10269872

ProQuest 10269872

Accepted by the Graduate Faculty, Indiana University, in partial fulfillment of the requirements for the degree of Doctor of Philosophy.

Doctoral Committee

_____

Chen-Yu Liu, Ph.D.

_____

William M. Snow, Ph.D.

_____

Joshua Long, Ph.D.

_____

Charles Horowitz, Ph.D.

Date of Defense: 1 February 2017

ACKNOWLEDGEMENTS

Evan Robert Adamek

Measurement of the Neutron Beta Decay Lifetime Using Magnetically Trapped

Ultracold Neutrons

The neutron lifetime is an important parameter in the Standard Model of particle physics, with influences on the electroweak interaction and on Big Bang nucleosynthesis. Measurements of this quantity in cold beam experiments and in experiments using ultracold neutrons (UCN) disagree; this discrepancy may indicate that these measurements possess unaccounted-for systematic errors. The UCNτ experiment at Los Alamos Neutron Science Center (LANSCe) utilizes an asymmetrical magneto-gravitational storage volume with an in-situ vanadium detector. This setup is designed to either avoid or control many of the weaknesses that reduce systematic precision in other UCN lifetime experiments. Controlling for the many measurable errors requires detailed calculation and simulation, aided, for example, by the Geant4 Monte Carlo particle transport toolkit, which has been used to create a high fidelity model of the UCNτ experiment for modeling UCN transport, storage, and detection. Through the course of running the experiment, improvements in knowledge of particle measurement have led to improvements to the transport and to the detectors used in various parts of the experiment. With the experimental setup optimized to account for the subtleties of the measurement, the 2014-2015 beam period at LANSCe generated 85 measurement runs from which we could calculate the storage lifetime. Careful analysis of the effects of background on the vanadium detector assembly allowed for elimination of undesired signal and allowed for the extraction of a preliminary value for the neutron lifetime and the determination of areas to improve for the following run cycle.

Chen-Yu Liu, Ph.D.

William M. Snow, Ph.D.

Joshua Long, Ph.D.

Charles Horowitz, Ph.D.

TABLE OF CONTENTS

LIST OF APPENDICES

LIST OF FIGURES

LIST OF TABLES

CHAPTER 1

INTRODUCTION AND MOTIVATION

1.1 Introduction

Ever since the discovery of the neutron, it has been suspected to have possible decay channels into lighter elementary particles. The measurement of the free neutron mass at $M_n = 1.0090$ amu [12] gave rise to the possibility of decay into a proton through emission of an electron and antineutrino, which is referred to as beta decay:

$$n \rightarrow p + e^- + \overline{\nu}_e + 0.782 MeV \tag{1.1}$$

The mass values of the neutron mass has since been improved to 939.565379(21) MeV/c^2 [17], and neutron decay has been directly observed in numerous experiments. Nuclear reactors and modern accelerators have provided vastly improved neutron flux to facilitate increasingly precise neutron experiments.
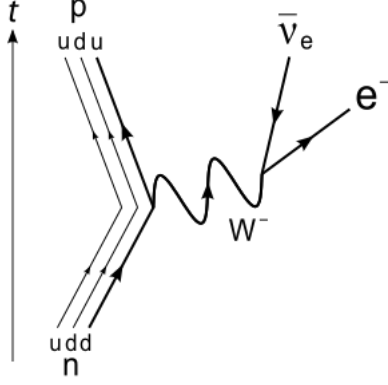
Figure 1.1: Feynman diagram of the beta decay interaction.

1.2 Importance of the Neutron Lifetime

Within the Standard Model of particle physics, beta decay is mediated by the emission of a charged W boson, which subsequently decays into the leptonic products (See Fig. 1.1). If we write out the probability amplitude for this transition, we see that the matrix element for this ineteraction is dominated by a vector minus axial vector (V-A) term:

$$M = [G_V \bar{p}\gamma_\mu n - G_A \bar{p}\gamma_5\gamma_\mu n] \left[\bar{e}\gamma_\mu(1 + \gamma_5)\nu\right] \tag{1.2}$$

where $\bar{p},n,\bar{e}$, and ν are the corresponding spinors for each particle and G_A and G_V are the coupling constants for the axial vector and vector forces. The two coupling constants are directly proportional to the Cabbibo-Kobayashi-Maskawa (CKM) matrix term V_{ud}. We can find the decay probability rate using Fermi's golden rule:

$$dW = (2\pi)^{-5}\delta(E_e + E_\nu - (m_n - m_p))\frac{1}{2E_e}\frac{1}{2E_\nu}d^3\boldsymbol{p}_e d^3\boldsymbol{p}_\nu |M|^2, \tag{1.3}$$

By integrating this over the antineutrino momentum and electron solid angle we can

determine the decay constant, incorporating vector and axial vector coupling constants G_V and G_A:

$$\frac{dW}{dE_e} = \frac{G_V^2|<1>|^2 + G_A^2|<\sigma>|^2}{2\pi^3} E_e|\boldsymbol{p}_e|((m_p - m_n) - E_e)^2 \tag{1.4}$$

$$\implies W = \frac{1}{\tau_n} = \frac{(G_V^2 + 3G_A^2)}{2\pi^3} f_R, \tag{1.5}$$

where f_R is the integral over the Fermi energy spectrum. The neutron lifetime is then the inverse of Equation 1.5, and so this equation gives us a means by which to experimentally determine the vector and axial vector coupling constants [18]. The f_R factor is computed based on the Coulomb spectrum, recoil order, and radiative corrections, and is found to be $2\pi^3/f_R = 4908.7(1.9)G_F^2$, where G_F is the Fermi weak coupling constant $1.16637(1) \times 10^{-5}GeV^{-2}$ and the units are defined to yield 1/s when introduced into Equation 1.5. [16]

The link between τ_n and V_{ud} also serves as a means of testing the unitarity of the CKM matrix. With greater precision on the values of the matrix elements, the unitarity condition can provide a constraint on the existence of yet undiscovered amplitudes, beyond V-A, coupled to quark states beyond the Standard Model.

The physical processes governed by G_A and G_V are not limited to neutron beta decay. Notably, superallowed $0^+ \to 0^+$ nuclear beta decays provide an alternate measurement of their values for various nuclei with low uncertainties arising from nuclear structure. While this is reliable for determining the vector coupling constant, the axial vector current is not conserved and the ratio G_A/G_V can be influenced by several strong interaction processes. Combining G_V from nuclear processes with measurements such as correlation coefficients in

neutron beta decay offers a competing method to experiments which measure the neutron lifetime.

Other weak current interactions which these constants influence include the proton-neutron oscillations in the early universe, proton-proton fusion in solar reactions, and neutrino/antineutrino detection. The first of these is particularly interesting, as the formation of nucleons during big bang nucleosynthesis (BBN) gives a prediction of light nuclei abundances that tie into astrophysical observations. In the early universe (t<0.1s), the universe consisted of a hot plasma of all standard model fundamental particles kept in thermal equilibrium through exchange of force bosons. Once the quarks fused to form protons and neutrons, they remained in equilibrium through the reactions:

$$n + e^+ \leftrightarrow p + \bar{\nu}, \qquad p + e^- \leftrightarrow n + \nu \tag{1.6}$$

The rates of these reactions are proportional to the strength of the charged weak interaction discussed above. As the universe expanded and cooled, the reactions fell out of equilibrium at a time $t_{freeze} \approx 1s$ and temperature $T_{freeze} \approx 1 MeV$. At this freeze-out time, the ratio of neutrons to protons is $n/p = e^{-(m_n - m_p)/T} \approx 1/6$. As the universe cooled further, this ratio shrinks as the neutrons decayed until all free neutrons were gone either through beta decay or through capture on protons to form deuterium and helium. Since these final abundances, especially that of ^{4}He are directly tied to the neutron lifetime and the weak interaction, the experimentally measured value of τ_n is an important input to the BBN model and in fact comprises the dominant uncertainty in the predicted primordial helium abundances. [18]

1.3 Ultracold Neutrons

During his work on neutrons, Enrico Fermi realized that cold neutrons interact with matter in a way that could be described as an effective potential, known as the Fermi psuedo-potential or simply as the Fermi potential V_F, which would be positive for most materials. These potentials typically are around $V_F \approx 10^{-7}eV$, which is orders of magnitude lower than the energy of thermal and even cold neutrons. Neutrons with energies at or below this energy region are referred to as ultracold neutrons, or UCN, and exhibit useful experimental properties as a result. We define the cutoff energy for UCN to be 300neV, which corresponds to a neutron velocity of 7.6 m/s. UCN see the Earth's gravitational potential as $V_g/h = m_n g = 102neV/m$. In addition to influencing the kinematics of UCN motion, this also gives an upper limit on vertical travel, as a 300 neV UCN loses all its kinetic energy after rising a height of 2.94m.

The neutron is a spin-1/2 particle with a magnetic moment $\mu_n = -1.913\mu_N \approx -60.3neV/T$. UCN traveling through a magnetic field gradient experience a force of $F_m = -\nabla V_m = \pm|\mu|\nabla|\mathbf{B}(\mathbf{r})|$, where we have simplified to the adiabatic case due to the low neutron velocity. Notice that a magnetic gradient will provide a force on the UCN parallel to the gradient. For a sufficiently high field, the UCN with spin states aligned with the field will be repelled and those anti-aligned with the field will be attracted. We describe the first category as "low-field seeking" and the second as "high-field seeking" neutrons. If the UCN are incident on a sufficiently strong field gradient, then the low field seeking UCN will interact with the field as an insurmountable barrier and be reflected, while the high field seeking UCN will transmit through the medium, creating a highly spin-polarized population of UCN. For a completely polarized population of low field seeking UCN, a magnetic barrier can be used as a trapping volume.

When considering the interaction of the neutron with a collection of nuclei, such as when a UCN encounters a material surface, it is helpful to treat the effective potential as the sum of the potentials within the bulk:

$$V(\mathbf{r}) = \frac{2\pi\hbar^2}{m} \sum_i a_i \delta(\mathbf{r} - \mathbf{r_i}), \tag{1.7}$$

where $\mathbf{r_i}$ is the position of the ith nucleus and the sum is over all nuclei in the bulk. We can solve the Schrödinger equation for the wavefunction under the approximation that the wave incident on each nucleus is simply the wavefunction at that nucleus, and arrive at the expression for the Fermi effective potential of the bulk:

$$V_F = \frac{2\pi\hbar^2}{m} N a, \tag{1.8}$$

where a is the scattering length and N is the number density in the material [14]. This is extremely useful for describing the motion of UCN because any material surface can be approximated as a step potential of height V_F. A natural consequence of this is that any UCN with energy below the Fermi potential are totally reflected from that surface, and as such can be trapped in material bottles. This forms the basis for one class of neutron lifetime experiments.

1.4   Current Status of the Field

Precision measurements of the neutron lifetime follow two main experimental strategies. The first measurements employed beams of slow neutrons for their measurement. When a beam with known density ρ_n is directed through a known volume V, the rate of neutron

decay can be described by the differential equation $dN/dt = -\rho_n V/\tau_n$. The rate of decay is determined through the detection of protons and/or electrons from decays occurring within the decay volume. The leading beam experiment for measuring the neutron lifetime is the NIST beam experiment, which utilizes a segmented Penning trap as the decay volume to capture the decay protons and guide them to the detectors. The segmentation allows differing numbers of electrodes to be activated as a means of altering the trap volume. The most recent measurement by this experiment is $\tau_n = 887.7 \pm 1.2_{stat} \pm 1.9_{syst} s$, with the leading systematic uncertainty coming from neutron flux measurements[10].

The other method of measuring the neutron lifetime utilizes the trappable nature of ultracold neutrons. Since UCN can be confined by material, magnetic, and gravitational interactions, it is possible to store them in a material bottle and measure the surviving neutrons at successive points in time. A typical bottle experiment utilizes a two point measurement in which two storage times are prescribed, t_1 and t_2 from a baseline filling time. Since we expect the trapped population to follow a curve $N(t) = N_0 e^{-(t-t_0)/\tau}$, we can write the lifetime based on the two measurements as:

$$\tau = \frac{t_2 - t_1}{log(N_1/N_2)} \tag{1.9}$$

Note that since the lifetime value depends on the ratio N_1/N_2, we need only take relative measurements and the detection efficiency cancels to first order. While this gives the lifetime of a neutron within the bottle, it is not a priori known that the only mechanism for loss is beta decay. We generally encounter additional loss terms which impact the bottle lifetime, such as material and residual gas interactions and alternative escape trajectories. The lifetime is therefore extracted by measuring all loss terms and computing:

$$\frac{1}{\tau} = \frac{1}{\tau_n} + \sum_{loss\,sources} \frac{1}{\tau_{loss}} \tag{1.10}$$

Following the development of improved sources for ultracold neutrons, bottle experiments rose in viability for competitive precision measurements of the neutron lifetime. An early example of this was the MAMBO experiment[3] at the Institut Laue-Langevin national laboratory. The apparatus, seen in Figure 1.2, has a storage volume consisting of glass walls coated in Fomblin Y Vac18/8 oil ($[F_3CCF_2OCF_2CF_5]_n$), a fluorinated polyether with a Fermi potential of 106.5 neV. Fomblin oil is a highly viscous liquid with an average molecular weight of 2650amu, a relative vapor pressure of 2×10^{-8} at room temperature, a loss probability of 3×10^{-5} on reflection, and a high level of uniformity and film renewability on the glass substrate. The glass volume is a rectangular box with h=30cm, w=40cm, and variable length x < 10cm. To vary the length, the far wall was mounted on a piston with better than 0.05 mm precision in linear movement. Furthermore, this wall had a surface of sinusoidal corrugations to redirect the forward-biased incoming flux of UCN to be isotropic within the storage volume. The adjustable length of the box serves to control the volume-to-surface-area ratio of the storage volume, which in turn influences the mean free path between wall collisions $\lambda = 4V/S$. Since the wall loss rate is described by $1/\tau_{wall} = \mu(v)v/\lambda$ and is therefore energy dependent, the storage times for each run can be chosen to be directly proportional to λ to return the same average number of wall interactions per storage cycle. This number could then be extrapolated to zero. The resulting lifetime measured after corrections was published in 1989 as $\tau_n = 887.6 \pm 3.0s$.[3]

The MAMBO group repeated the experiment with a new apparatus called MAMBO II[1] (Fig. 1.3) which aimed to follow up on the preceding experiment with additional controls over the systematic errors. To ensure the UCN spectrum was independent of trap volume
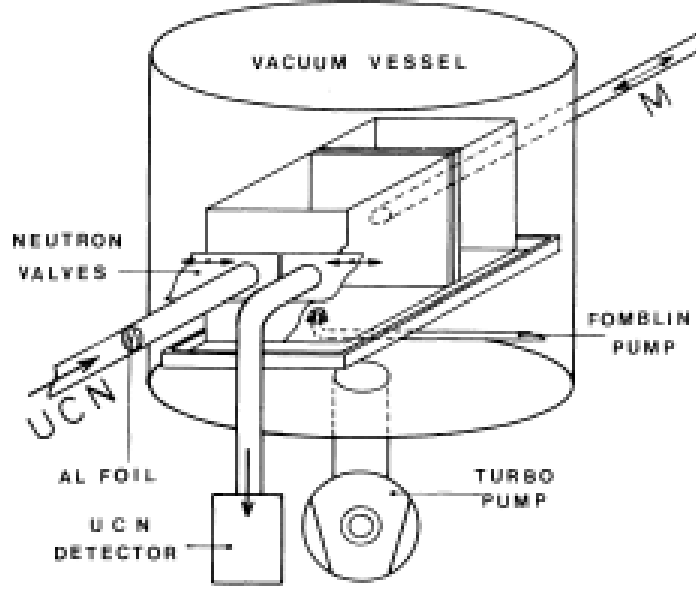
Figure 1.2: Diagram of the MAMBO experiment apparatus.[3]

and to reduce the upper limit of UCN energies, the storage population was conditioned by use of a prestorage volume with an adjustable polyethylene absorber forming the upper surface. Once the high energy UCN were eliminated, the population was fed into the storage volume and the experiment proceeded identically to MAMBO I. The outcome of this experiment came to $880.7 \pm 1.8s$, significantly lower than the MAMBO I result. The newer value was determined to be more trustworthy due to the results of the systematic studies on $\mu(v)$ as well as the greater agreement of the counts per storage time to a decaying exponential.[1]

Another noteworthy bottling experiment is the Serebrov Gravitrap[2] developed at the Petersburg Nucler Physics Institute and performed at ILL, which followed up on an earlier Gravitrap measurement done by Kharitonov *et al.* The apparatus (Fig. 1.4) consisted of a low-temperature Fomblin (LTF) coated storage spherical or cylindrical volume with a window at the end, which could be rotated to various angles. With the window pointing down, the trap could be loaded from the source or unloaded into the detector. This storage

9
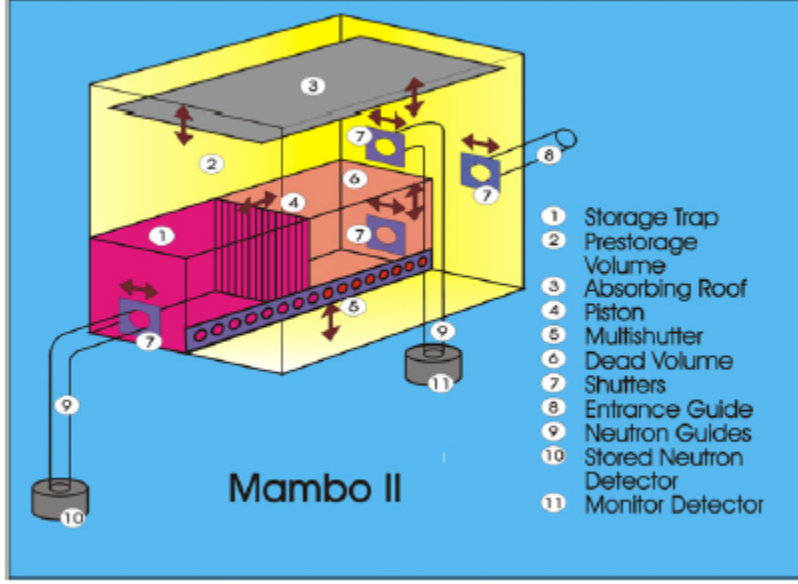
Figure 1.3: Diagram of the MAMBO II experiment apparatus.[1]

volume would trap UCN through the LTF wall potential from the bottom and sides, and by gravity above. The angle of the window determined the upper limit on the trappable population of UCN. As such, the trap could be emptied in steps of successively lower window angles to measure any spectrum dependence in the UCN storage. An example of a typical run cycle can be seen in Figure 1.5. The gravitational spectroscopy allowed for control over multiple spectrum based systematic effects. A detailed Monte Carlo simulation was performed to investigate the accuracy and reliablility of the experiment. The 2005 result was published as $878.5 \pm 0.7_{stat} \pm 0.3_{syst}$, significantly less than the PDG average of all lifetime values from previous experiments.[2]

The deviation of the Serebrov result from the world average by 5.6 σ called into question the results up to that point. However, further investigation into the type of experiment from recent years shows a further discrepancy. If one averages the beam experiment lifetimes, the result comes to a world average of 887.1(2.2) s, whereas an average of bottle experiments comes to 878.5(0.8) s, in line with the Serebrov result (Figs. 1.6, 1.7). This
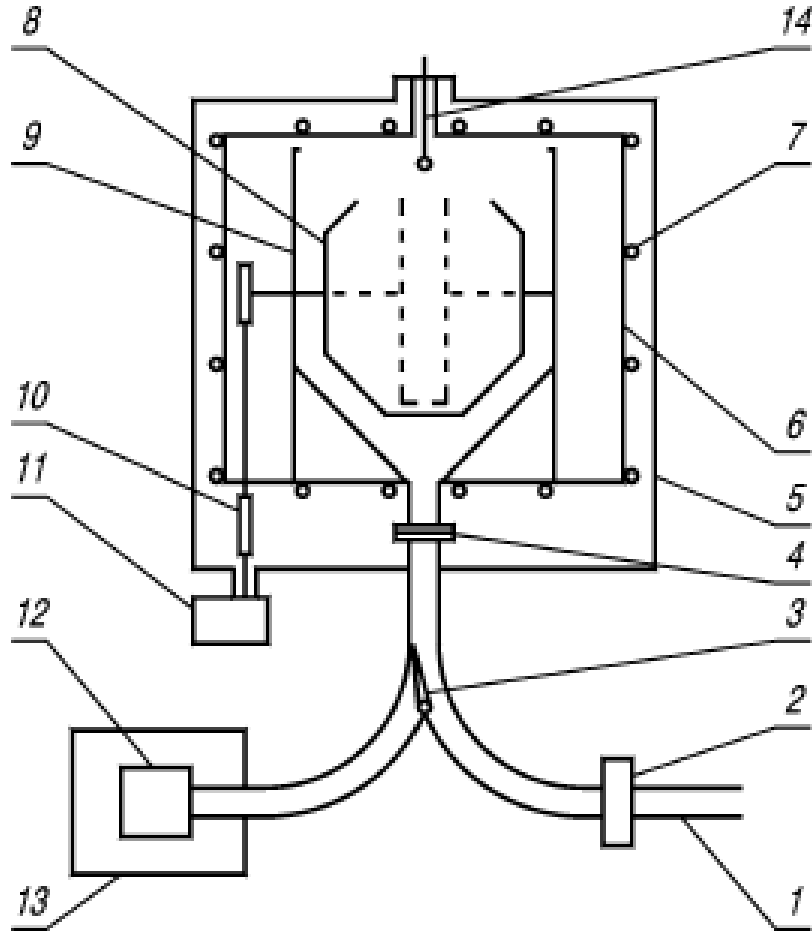
Figure 1.4: Gravitrap II storage apparatus used by Serebrov.[2]

shows that there exist either confounding systematics or unaccounted-for physical processes which are different between the two measurement methods. Since the beam experiments are appearance measurements while the bottle experiments are disappearance measurements, one such example might be a seperate decay branch of the neutron into products other than $p + e^- + \bar{\nu}_e$. As a means of resolving this discrepancy, it is necessary to perform new experiments which avoid the systematic errors associated with the previous experiments. If the discrepancy is an artefact of the experimental design, then careful consideration of these systematics should reveal the source of the discrepancy in lifetime
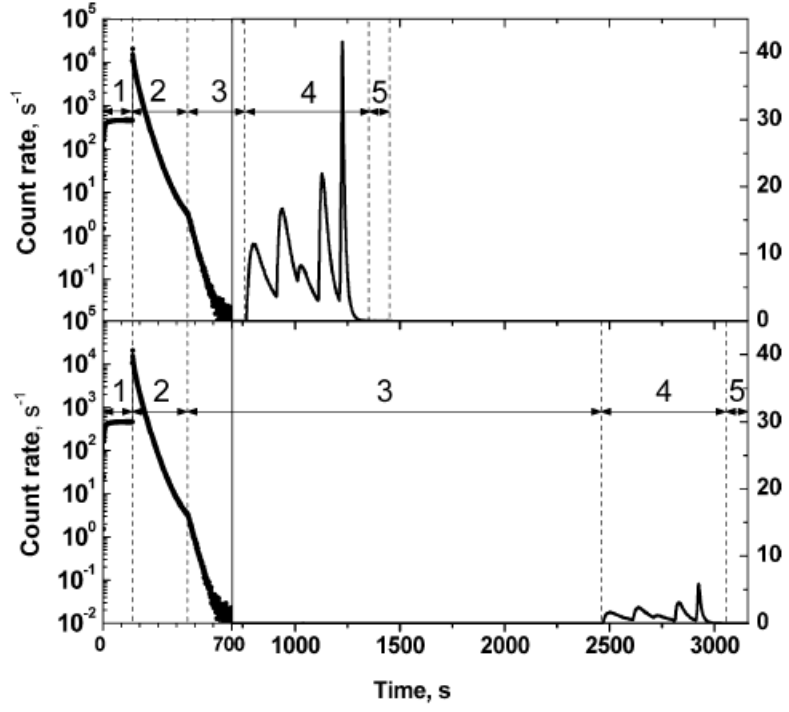
Figure 1.5: Timing diagrams for the short and long storage cycles used in the GravitrapII experimental run.[2]

values obtained by beam and bottle methods.

Reference	Neutron lifetime (s)	Uncertainty (s)
Beam Experiments		
Robson, 1951	1110	220
Spivak *et al.*, 1956	1040	130
D'Angelo, 1959	1100	160
Sosnovsky *et al.*, 1959	1013	26
Christensen *et al.*, 1972	918	14
Last *et al.*, 1988	876	21
Spivak, 1988*	891	9
Kossakowski *et al.*, 1989	878	30
Byrne *et al.*, 1996*	889.2	4.8
Nico *et al.*, 2005*	886.3	3.4
Bottle Experiments		
Kosvintsev *et al.*, 1980	875	95
Kosvintsev, Morozov, and Terekhov, 1986	903	13
Morozov, 1989	893	20
Mampe *et al.*, 1989*	887.6	3.0
Alfimenkov *et al.*, 1992	888.4	3.3
Mampe *et al.*, 1993*	882.6	2.7
Arzumanov *et al.*, 2000	885.4	0.98
Serebrov *et al.*, 2005*	878.5	0.76
Pichlmaier *et al.*, 2010*	880.7	1.8
Magnetic Trap Experiments		
Paul *et al.*, 1989*	877	10
Ezhov *et al.*, 2009	878.2	1.9

Figure 1.6: List of results from various notable lifetime measurement experiments.[18]
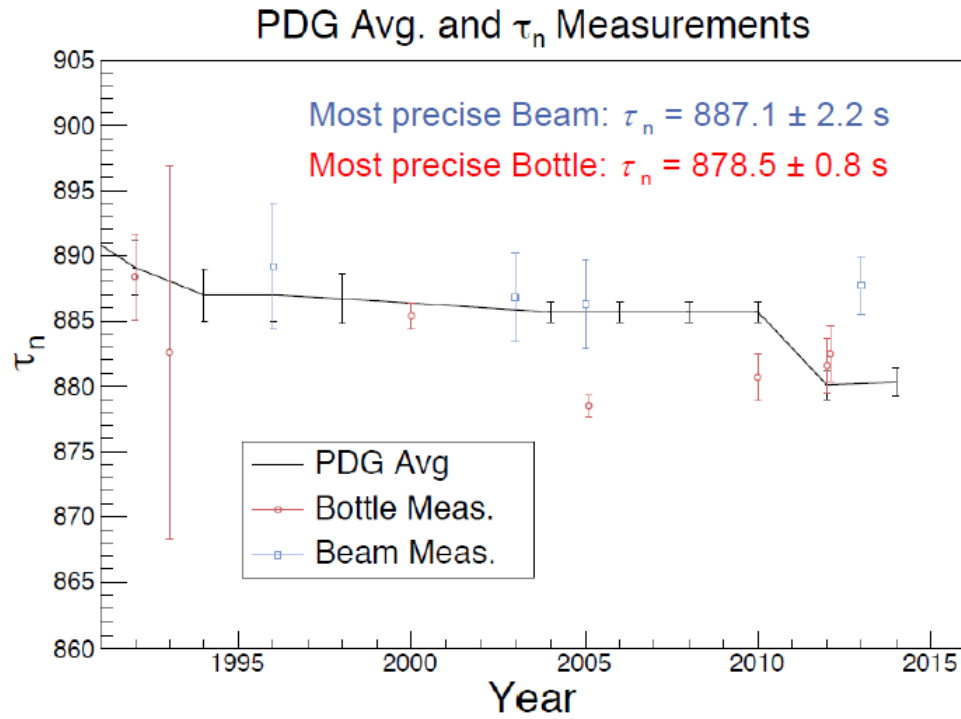
Figure 1.7: Plot of recent lifetime experiments, with distinction between bottle experiments (red) and beam experiments (blue). The delay between the 2005 Serebrov result and its acceptance into the PDG world average can be seen in the post-2010 drop in the line.

CHAPTER 2

EXPERIMENTAL SETUP OF UCNτ

2.1   Overview of the UCNτ Experiment

The UCNτ experiment located at Los Alamos Neutron Science Center (LANSCe) aims to provide a precision measurement of the free neutron lifetime using a novel bottling technique that maximizes storage volume and experimental flexibility. The UCN storage volume consists of a 670 L asymmetric magneto-gravitational trap formed by a bowl-shaped halbach array of NdFeB permanent magnets, with a maximum depth of 50cm from the lip of the trap. This open-topped setup allows both the storage of UCN with E<50neV with minimal wall interactions and access to the storage volume for in-situ measurement of surviving neutrons. This in-situ detector makes use of neutron capture on vanadium, and will be discussed in greater depth in Chapter 4.

2.1.1   UCN Production

The neutron source at LANSCe creates neutrons from a tungsten spallation target. These neutrons are thermally cooled to around 4K and subsequently slowed by downscattering through a solid deuterium (D_2) crystal, producing neutrons with a continuous energy
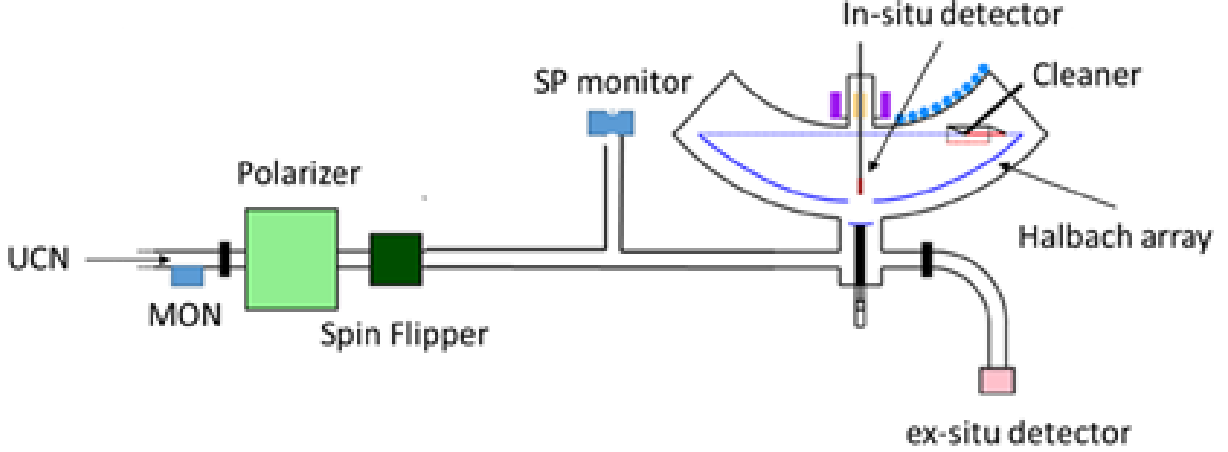
Figure 2.1: Schematic layout of the UCNτ experiment and UCN transport system.

distribution, trappable within the source volume up to 300 neV. There is a flapper above the D_2 crystal at the entrance of the source storage volume which remains open for a 0.2s time window after each beam pulse during normal operation. Once in the source storage volume, the UCN diffuse into the transport guide system through a 3 inch stainless steel guide ($V_F = 250$neV) and exit the source shielding wall with a density around 60 UCN/cm^3[4]. The shield wall exit point is immediately followed by a gate valve backed by a downstream neutron absorber as well as an aperture upstream of the gate valve which leads to a drop guide and a neutron detector for relative monitoring, which is referred to as the gate valve monitor. The spectrum at this point has been measured through downstream monitoring to be weighted by velocity v as $N(v) \propto v^{2.7}$ according to fits, with an angular distribution $N(\cos(\theta)) \propto \cos(\theta)^{1.5}$ (see Fig. 2.2). These values are useful for transport simulation, as will be discussed later.
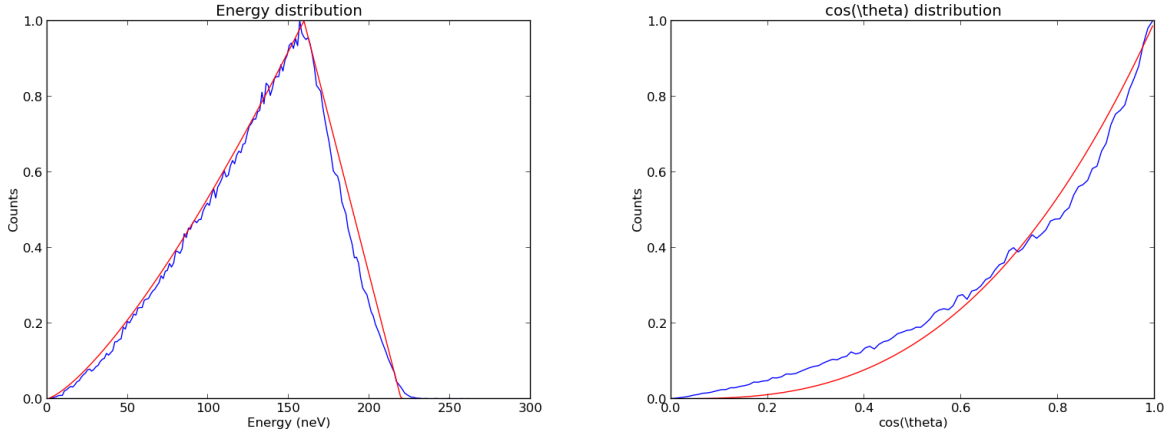
Figure 2.2: UCN energy (left) and angular (right) distributions, measured at source exit.

2.1.2 UCN Spin Polarization

In order to polarize the UCN population for magnetic storage, a 1m long prepolarizing magnet (PPM) is placed immediately downstream of the gate valve monitor. The PPM is a superconducting electromagnet which generates a field of 7 T parallel with the neutron guides at that point. At the center of the field region, the guide contains a Zr window ($V_F \approx 100$ neV). When the field is applied, low field seeking UCN are repelled and high field seeking UCN are accelerated through the window. Hence, downstream of the PPM the UCN are 100% polarized in the high field seeking spin state. Since the magnetic trappability of the UCN relies on them all being low field seeking, it is necessary to flip the spin states using a low-field adiabatic fast-passage spin flipper with $B_0 \approx 140G$ and $f \approx 0.4MHz$. A major component of the transport efficiency relates to ensuring that the UCN do not spontaneously flip spin states during transport, which can occur during wall interactions or upon passing through a region of zero magnetic field. To prevent such field zeros from occuring, a series of holding field coils carrying 300A provides a 60 to 90 Gauss field along the long radius of the trap (See Figure 2.3) to create a constant nonzero field

perpendicular to the Halbach field gradient.
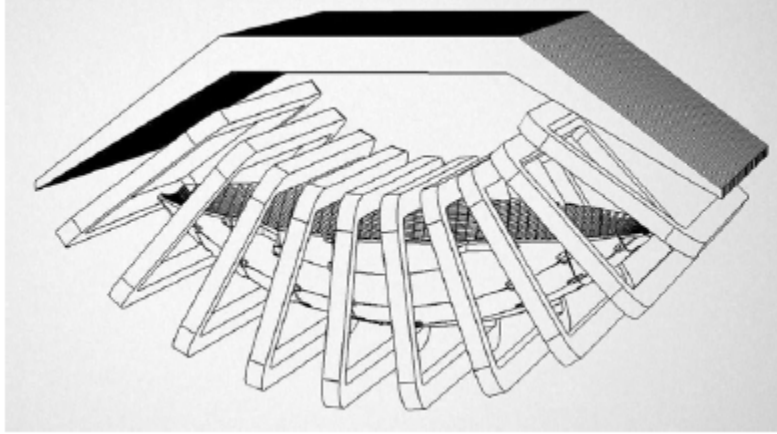
Figure 2.3: Orientation of the electromagnetic field coils used to prevent field zeros within the trap volume. The iron flux return pictured was not included in the final experimental setup.[7]

2.1.3 Detection Methods

Several UCN detectors are installed along the transport system to determine UCN trap population stability and quality of source production. Upstream of the gate valve, there is a vertical 3/8" aperture with a drop guide into a ^{3}He MWPC detector. This exists as the primary means of monitoring the beam level and assessing the stability of the UCN flow out of the source. Downstream of the trap opening, there is a boron coated detector which was initially appended to the end of a 1m stainless steel drop guide. This setup was later replaced with a directly appended ZnS detector. Discussion of the different varieties of detector will be presented in Chapter 4. The purpose of this detector is two-fold: first, it provides a secondary measure of beam stability subject to the various loss parameters in the guide system, and second, it provides a means of measuring the surviving UCN in the trap through a draining measurement. This type of fill-store-empty measurement is not the main means of storage measurement, but serves as a means to compare with methods used by previous experiments. Later iterations of the experiment utilized a third guide monitor

upstream of the trap which is mounted on a vertical tee off of the main guide. The ZnS detector is placed level with the Halbach array rim as a means of measuring the untrappable component of the UCN spectrum. This extra "standpipe" detector serves to improve our knowledge of any changes in the spectrum of the UCN produced by the source. Finally, there is a vanadium based in situ detector which is placed on top of the trap and can be lowered into the storage volume for detection of trapped UCN. More details on this setup will be described in Chapter 4.

2.1.4 Spectral Cleaning

One prevailing issue with bottle measurements of the neutron lifetime is the existence of quasi-trapped or marginally trapped neutrons. These are neutrons which are above the energy threshold to be trapped, but which have orbits that remain within the trap for times on the order of the neutron lifetime. Failure to control for these marginally trapped UCN results in an additional loss component which prevents a reliable lifetime value to be ascertained. The design of the UCNτ trap is such that the trappable energy threshold is 50neV and UCN above that threshold will escape predominantly by falling out of the trap through the open top. An effective means of eliminating this marginally trapped population is through spectral cleaning to eliminate UCN above the threshold energy. This is accomplished by the use of a cleaner consisting of a polyethylene surface which is lowered to a specified height below the trap rim for a short time just after the trap is populated. Any UCN which interact with the cleaner surface upscatter with high probability and are removed from the trap population. In accordance with simulation, this cleaner is set to a height of 42.5 cm for the duration of the cleaning, which is expected to achieve full cleanout within 30s (See Figs. 2.4 and 2.5). While these predictions utilize a cleaner which fully occupies half of the trap cross section, the cleaner used for actual studies is much

smaller, at around 2' by 1.5'. To supplement this smaller area, a larger, immovable polyethylene cleaner surface was installed over the other half of the trap volume to provide a larger area cleaning at a cleaning height of 50cm. The two cleaners in tandem achieve the 30s cleaning prediction for marginally trapped UCN.
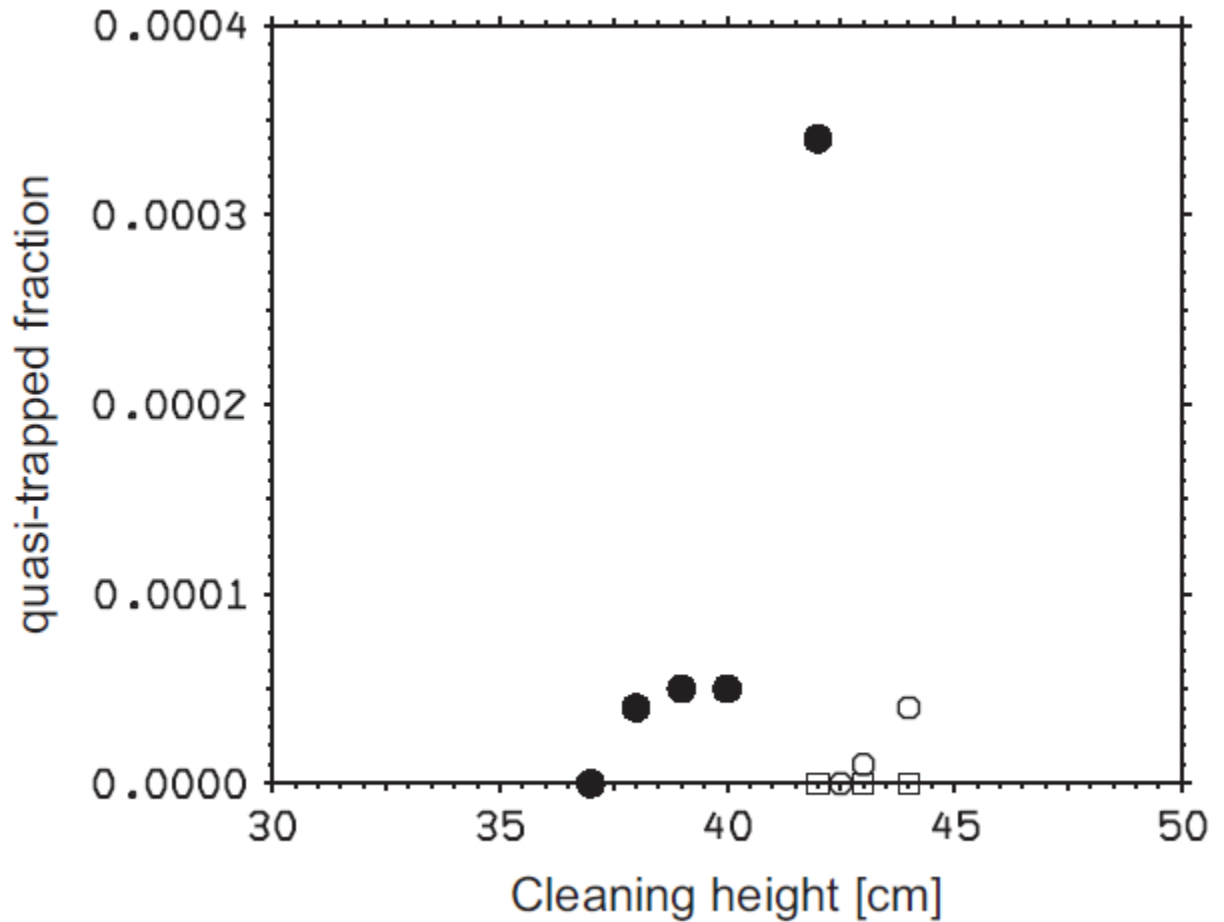
Figure 2.4: Simulated fraction of marginally trapped UCN as a function of cleaning height. Results are shown for smooth field (closed circles), one-way ripple (open circles), and two-way ripple (open squares) models of the surface magnetic field. The one-way ripple model (open circles) is representative of the field used in UCNτ.[7]
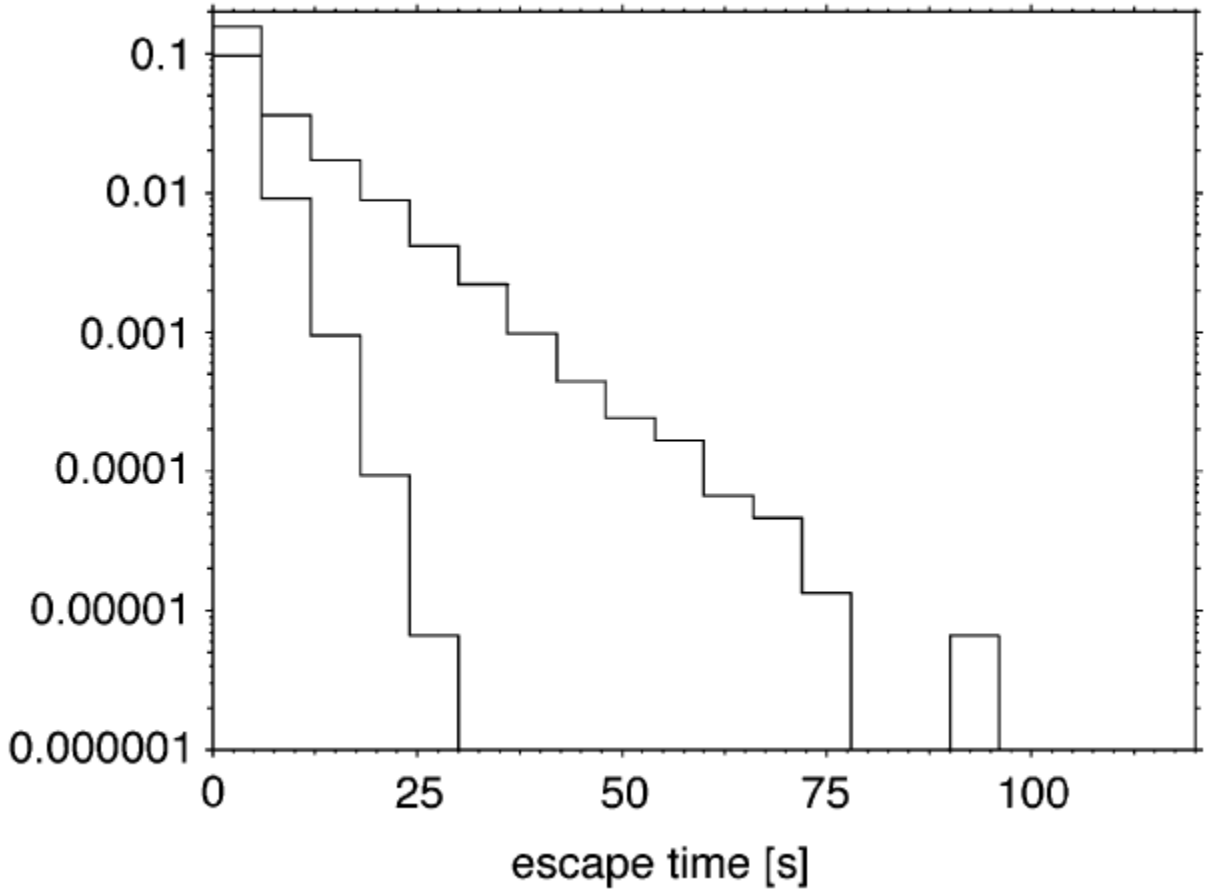
Figure 2.5: Predicted population curve for marginally trapped UCN at cleaning heights h=44cm (upper curve) and h=42cm (lower curve).[7]

2.1.5 Trapping UCN

In order to compute the neutron storage lifetime within the trap, a typical experimental run proceeds as follows. The UCN source is turned on with the gate valve open for a specified filling time to allow the UCN to diffuse down the transport guides. During this time, the flux of the UCN is monitored through several guides split perpendicularly off the main beam line. Below the trap, the UCN encounter a junction in the guides which will henceforth be referred to as the cross assembly. The purpose of the cross assembly is to provide a mechanism by which a 6.75 in by 7 in section of magnets (i.e., a trapdoor) is

21

lowered out of the Halbach array to allow the UCN to access the storage volume. The UCN are allowed to diffuse upward through the trapdoor during the fill until the trap population saturates. After this point, the trapdoor magnets are returned to the array sealing the trap off from the guide system, the gate valve is closed, and the beam is disabled. After a certain amount of storage time t_1, the remaining UCN are measured using the vanadium absorber and the number of counts is recorded as N_1. Once the trap is confirmed to be empty, the process is repeated for $t_2 > t_1$ yielding a count of N_2 neutrons, with the relative flux monitors ensuring that the source and transport quality are unchanged. In the absence of backgrounds, the lifetime is given by:

$$\tau = \frac{t_2 - t_1}{\log \frac{N_1}{N_2}} \tag{2.1}$$

We can simplify our mathematics by defining $t \equiv t_2 - t_1$ as the time between measurements. Treating each measured quantity as independent, the uncertainty in τ is:

$$\sigma\tau^2 = \left|\frac{\partial\tau}{\partial t}\right|^2 \sigma t^2 + \left|\frac{\partial\tau}{\partial N_1}\right|^2 \sigma N_1^2 + \left|\frac{\partial\tau}{\partial N_2}\right|^2 \sigma N_2^2 \tag{2.2}$$

where $\sigma t^2 = \sigma t_1^2 + \sigma t_2^2$ is the combined uncertainty for the time measurements. Note that

$$\sigma N_i = \sqrt{N} \tag{2.3}$$

for UCN counts.

The partial derivatives are found to be

$$\frac{\partial \tau}{\partial t} = \frac{\partial}{\partial t}\left(\frac{t}{\log \frac{N_1}{N_2}}\right) = \frac{1}{\log \frac{N_1}{N_2}} \tag{2.4}$$

$$\frac{\partial \tau}{\partial N_1} = t\left(\frac{1}{\log \frac{N_1}{N_2}}\right)^2 \frac{N_2}{N_1}\frac{1}{N_2} = \frac{t}{N_1 \log \frac{N_1}{N_2}^2} \tag{2.5}$$

$$\frac{\partial \tau}{\partial N_2} = \frac{\partial}{\partial N_2}\left(\frac{t}{\log \frac{N_1}{N_2}}\right) = \frac{\partial}{\partial N_2}\left(\frac{-t}{\log \frac{N_2}{N_1}}\right) = \frac{-t}{N_2 \log \frac{N_1}{N_2}^2} \tag{2.6}$$

Combining the above equations gives the uncertainty

$$\sigma\tau^2 = \frac{\sigma t^2}{\log\left(\frac{N_1}{N_2}\right)^2} + \frac{t^2}{\log\left(\frac{N_1}{N_2}\right)^4}\left(\frac{\sigma N_1^2}{N_1^2} + \frac{\sigma N_2^2}{N_2^2}\right)$$

$$= \frac{1}{\log\left(\frac{N_1}{N_2}\right)^2}\left(\sigma t^2 + \left(\frac{t}{\log \frac{N_1}{N_2}}\right)^2\left(\frac{1}{N_1} + \frac{1}{N_2}\right)\right) \tag{2.7}$$

Now, since we wish to consider the minimum of $\sigma\tau$ as we vary t_2 (and therefore t), we need to consider the functional relationship between the measured observables. In particular[1],

$$N_2 = N_1 e^{\frac{-t}{\tau}} \tag{2.8}$$

---

[1]In truth, this statement only holds true for the actual values of N_i and t. For the measured values, we propose that the real values are found as $X = X + \mathcal{O}(\sigma X)$. Then $N_2 + \mathcal{O}(\sqrt{N_2}) = \left(N_1 + \mathcal{O}(\sqrt{N_1})\right)e^{\frac{-(t+\mathcal{O}(\sigma t))}{\tau}} = N_1 e^{\frac{-t}{\tau}}e^{\frac{-\mathcal{O}(\sigma t)}{\tau}} + \mathcal{O}(\sqrt{N_1})e^{\frac{-t}{\tau}}e^{\frac{-\mathcal{O}(\sigma t)}{\tau}}$. Expanding the exponentials (and dropping the $\mathcal{O}$ functions for readability) gives $N_2 + \sqrt{N_2} = N_1 e^{\frac{-t}{\tau}}\left(1 + \frac{\sigma t}{\tau} + \frac{\sigma t^2}{2\tau} + \ldots\right) + \sqrt{N_1}e^{\frac{-t}{\tau}}\left(1 + \frac{\sigma t}{\tau} + \frac{\sigma t^2}{2\tau} + \ldots\right)$. We later make the assumption that $N_1\sigma t \ll \tau$, which reduces the expression to $N_2 + \sqrt{N_2} = \left(N_1 + \mathcal{O}(\frac{N_1\sigma t}{\tau})\right)e^{\frac{-t}{\tau}} + \left(\sqrt{N_1} + \mathcal{O}(\frac{\sqrt{N_1}\sigma t}{\tau})\right)e^{\frac{-t}{\tau}} = \left(N_1 + \mathcal{O}(\sqrt{N_1}) + \mathcal{O}(\frac{N_1\sigma t}{\tau})\right)e^{\frac{-t}{\tau}}$. For a sufficiently large storage volume, $\sqrt{N} \ll N$, and the expression reduces to equation (2.8)

Equations (2.1) and (2.8) may be used to simplify (7), yielding

$$\sigma\tau^2 = \frac{1}{\log\left(\frac{N_1}{N_2}\right)^2}\left(\sigma t^2 + \tau^2\left(\frac{1}{N_1} + \frac{1}{N_1 e^{\frac{-t}{\tau}}}\right)\right) \tag{2.9}$$

$$\Rightarrow \sigma\tau = \frac{\tau}{t}\sqrt{\sigma t^2 + \frac{\tau^2}{N_1}\left(1 + e^{\frac{t}{\tau}}\right)} \tag{2.10}$$

Therefore, we minimize the lifetime uncertainty when

$$\frac{\partial\sigma t}{\partial t_2} = \frac{\partial\sigma t}{\partial t} = 0 \tag{2.11}$$

$$\Rightarrow 0 = \frac{\partial}{\partial t}\left(\frac{\tau}{t}\sqrt{\sigma t^2 + \frac{\tau^2}{N_1}\left(1 + e^{\frac{t}{\tau}}\right)}\right)$$

$$= \frac{-\tau}{t^2}\sqrt{\sigma t^2 + \frac{\tau^2}{N_1}\left(1 + e^{\frac{t}{\tau}}\right)} + \frac{\frac{\tau}{t}\frac{\tau}{N_1}e^{\frac{t}{\tau}}}{2\sqrt{\sigma t^2 + \frac{\tau^2}{N_1}\left(1 + e^{\frac{t}{\tau}}\right)}} \tag{2.12}$$

$$\Rightarrow 2N_1\left(\sigma t^2 + \frac{\tau^2}{N_1}\left(1 + e^{\frac{t}{\tau}}\right)\right) = \tau t e^{\frac{t}{\tau}} \tag{2.13}$$

Defining $x = \frac{t}{\tau}$ yields the equation

$$2N_1\sigma t^2 + 2\tau^2 + 2\tau^2 e^x = \tau^2 x e^x \tag{2.14}$$

If we perform a measurement with sufficiently precise timing that $N_1\sigma t \ll \tau$, the τ^2s cancel and this result simplifies to

$$2 + 2e^x = xe^x \tag{2.15}$$

$$\Rightarrow \frac{2}{e^2} = (x - 2)e^{x-2} \tag{2.16}$$

$$\Rightarrow x = 2 + W\left(\frac{2}{e^2}\right) \tag{2.17}$$

where W is the Lambert W function[2]. We can evaluate numerically $W\left(\frac{2}{e^2}\right) \approx 0.2177\ldots$. We substitute back for the variables t_1 and t_2 to determine that the minimum lifetime uncertainty is obtained whenever[3]:

$$t_2 = t_1 + 2.2177\tau = t_1 + 1951.8s \tag{2.18}$$

As such, we plan for the long storage runs to be roughly 2000s longer than the short storage runs to maximize our statistical precision. A treatment of the case in which there is nonzero background is given in Appendix 1.

2.1.6   Data Acquisition

In order to obtain detector signals with accurate timestamps from the detectors during the running of the UCNτ experiment, a data acquisition system was created using Versa Module Europa (VME) computer bus modules. The signal processing chain is detailed in Figure 2.6 and will be described in further detail in this section. Front end control of the DAQ hardware and data recording was performed using sofware based on the MIDAS

---

[2]The Lambert W function is defined as the inverse function of $y = xe^x$. In general, it is a complex function with multiple branches; however, for real, positive values the result is real and single-valued, so there is no issue with solving the equation in this manner.

[3]Using the 2012 PDG value of $\tau = 880.1 \pm 1.1$

framework with ROME-based online analysis and data visualization based on the signal data. The anode signals from the ten NaI detectors are fanned out to the QADC, the discriminator, and the digitizer using FIFO NIM modules. The QADC line is amplified using a PS/777 variable linear amp and passes through a 64ns passive delay line to align the signal with the global trigger gate. The signal from the beta PMTs are fanned out to the discriminator and the linear amplifier, the latter of which sends the signal to the fADC and the QADC. Finally, the signals from the UCN detectors (gate valve, downstream monitor, standpipe monitor) are sent to the FADC, discriminator, and PADC. The analyzer arranges the data from the 17 channels and submits the channel, realtime, timestamp, energy, and IO register to both .root and .flat output files for further analysis. The online analyzer displays histograms of signals from each channel for the sake of monitoring the progress of each run.

The slow DAQ synchronizes the data acquisition with the output signals to the various components of the experiment. A typical structure of the slow DAQ signal generation for an experimental run is seen in Figure 2.7. The start signal from the slow DAQ activates the ROME online analyzer and the data acquisition routines, and sets each of the togglable settings to their default states. At t=0, the beam veto is disabled, the gate valve is opened, and the trapdoor is set to the down position in preparation of a fill. After the filling is complete, these settings toggle their state and the cleaner is lowered into the now closed trap. After the specified cleaning time, the cleaner is raised and the experiment enters its storage phase. Following this, the vanadium dagger is lowered into the trap and alllowed to absorbe the UCN for the saturation time, and then the trap is open and the vanadium is raised into the detector housing for counting. Upon the termination of the counting phase, the slow DAQ records the timing parameters and other useful information and returns to the default state.
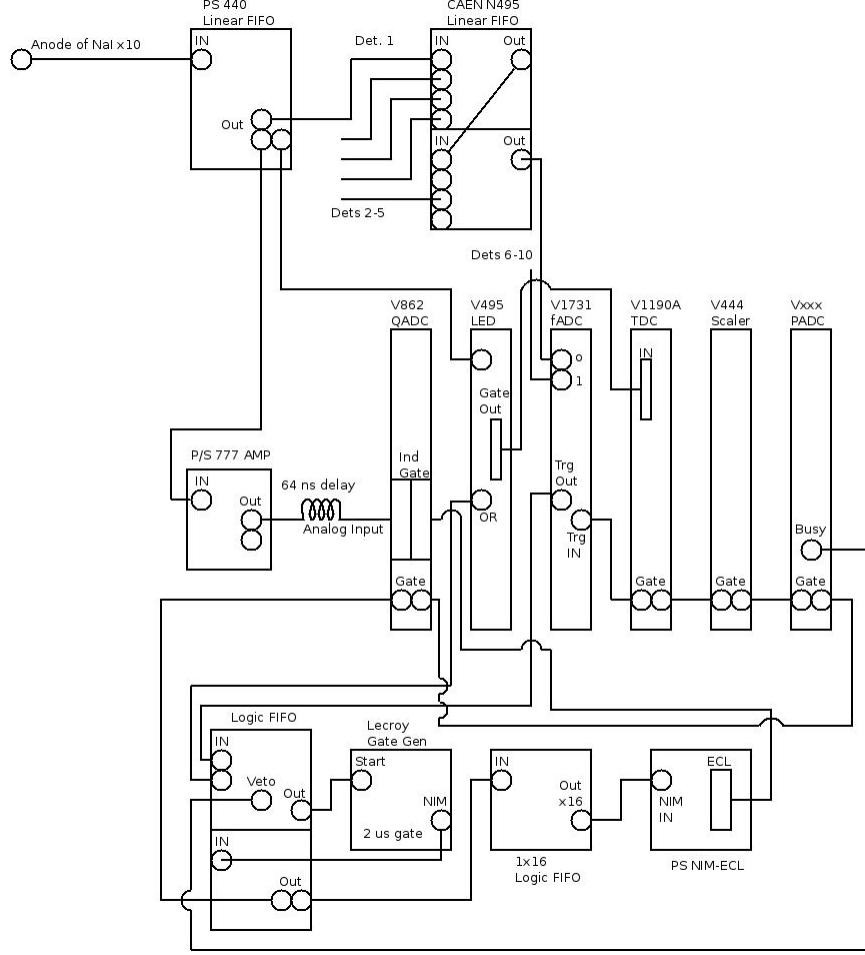
Figure 2.6: Diagram of the signal pathways in the data acquisition hardware.

2.2 2013 - 2014 Run: Proof of concept

In the Fall of 2013, the experimental apparatus was assembled and a series of trial runs were carried out. During these runs, the fill time was set to 180s, the cleaning time was set to 30s, and the storage time was varied between 100s and 2000s, with the former two values determined by simulation. After storage, the Al shutter downstream of the cross assembly was opened and the surviving UCN were drained into the downstream ^{10}B detector, which was used for monitoring during the fill. Figure 2.8 shows the histogrammed output from the detector in a typical run with $t_{store} = 150s$. The count rate for the background during the

27
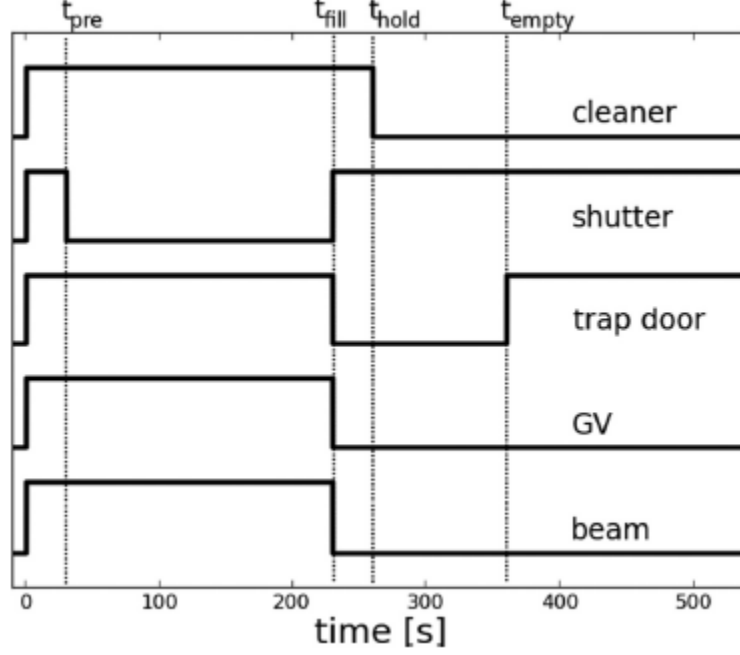
Figure 2.7: A typical timing pattern for each moving component controlled by the slow DAQ.

holding period fits to the function $B(t) = B_0 e^{-\beta t} + B_1$, where the second term represents the constant background and the first term represents the slow drain ($\beta \approx 0.15 s^{-1}$) of UCN from the filling phase. The mean rate R during the fill between t_{pre} and t_{fill} (the flat region from Fig. 2.8) gives a normalization factor for the trap population during one run for a sufficiently stable UCN beam; this stability is determined by cuts on the fluctuation of the ratio of shutter-open counts to R. The signal is then found by integrating:

$$S = \frac{1}{R} \frac{1}{\delta t} \int_{t_{empty}}^{t_{empty}+100} [D(t) - B(t)]dt \tag{2.19}$$

where δt is the integration bin width and D(t) is the detector rate while emptying. After 20 hours of running, the signal was plotted against t_{store} and fit to an exponential by least squares. The result, as seen in Figure 2.9, is a storage lifetime of 860 ± 19 s ($\chi^2/\nu = 0.87$)

28
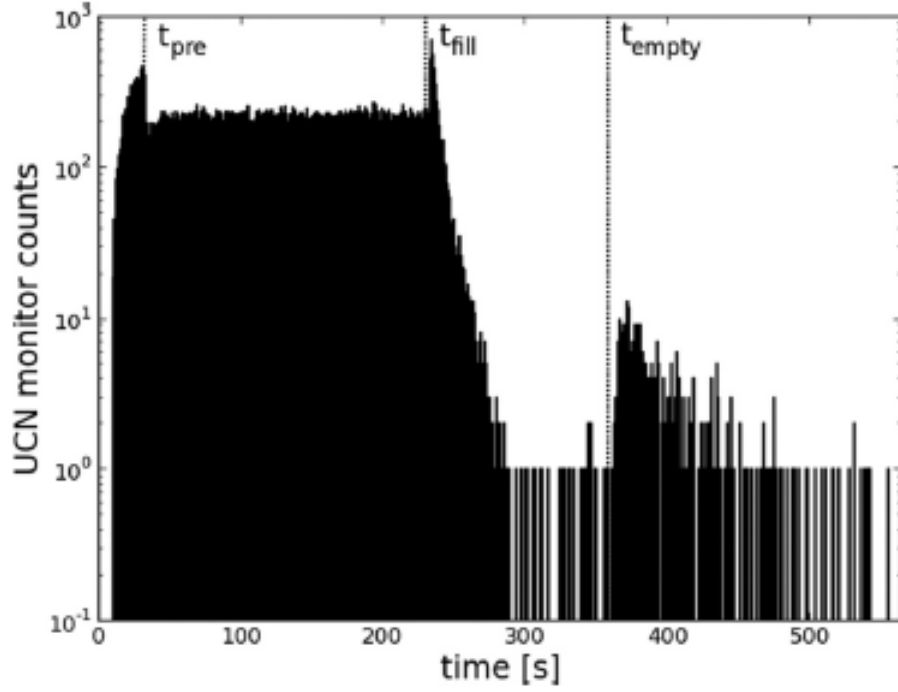
Figure 2.8: Typical timing plot of received counts by the downstream detector during a typical run. $t_{empty} - t_{fill} = 150s$. Note the drop in detected UCN at the time of shutter closing t_{pre}

with the holding field active and 470 ± 160 s $(\chi^2/\nu = 1.17)$ with it inactive. The fit is in agreement with the computed two-point measurement of τ as well as with the PDG global average for τ_n. The estimated trap population was on the order of 10^4 UCN per storage. This result demonstrates that the trap volume functions as desired to hold UCN for periods of 2000s and suggests areas for improving on the experimental run, such as improvement of transport and use of in-situ detection, both of which are subsequently incorporated.[5]
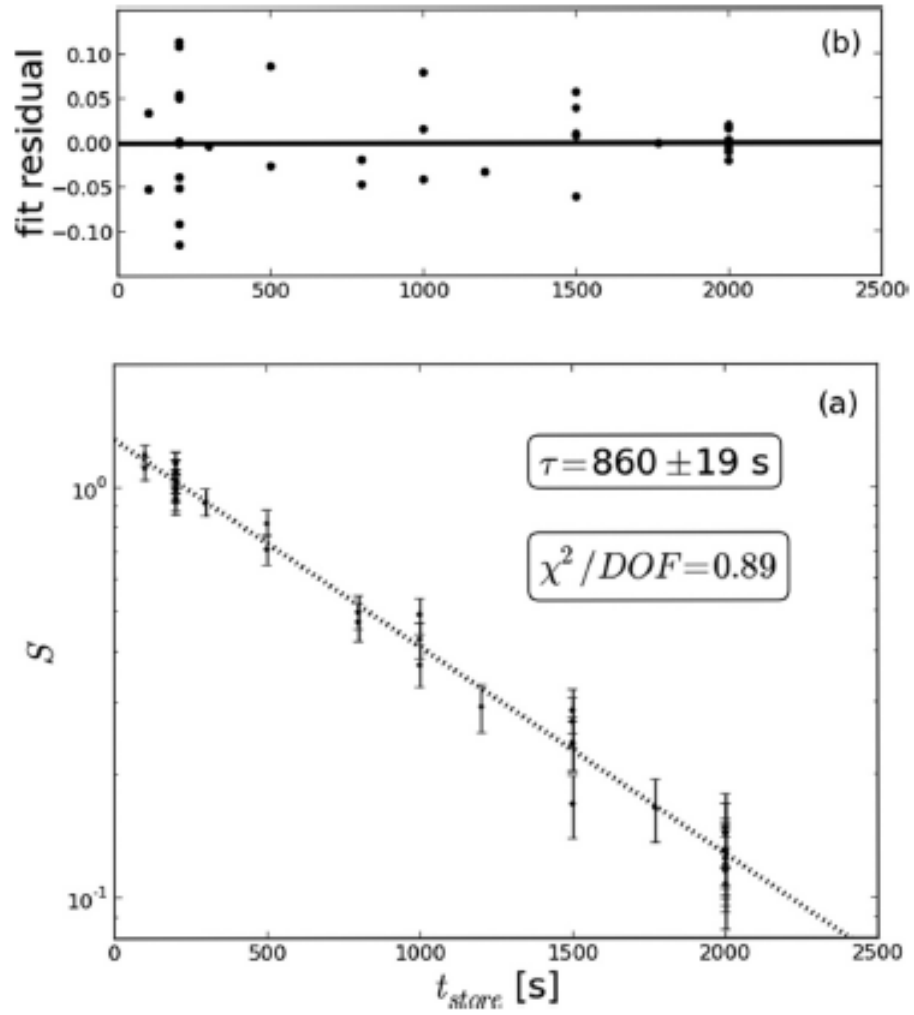
Figure 2.9: Fit of storage measurements to exponential. The fit demonstrates the efficacy of the storage volume.[5]

CHAPTER 3

GEANT4 SIMULATION WORK

3.1   Geant4 Overview

Geant4 is a C++ toolkit for particle transport first published in 1998 by a CERN-based
team of researchers based on the previous Geant3 code as a means of simulating the
transport of particles through matter. It provides a framework for creating a wide range of
computational studies, including full scale detector Monte Carlo simulations. The base
code contains a set of physics models which can be incorporated into the simulation as
needed to describe the relevant physical processes to be used. The abstract representation
of a set of physical processes to be simulated is referred to as an event. The event exists in
the G4Event class and contains all relevant physical and organizational parameters for
describing the state of the simulation, such as primary event vertices and particles, while
avoiding the retention of transient information. As a particle propagates within an event, it
follows a track described by a series of steps which discretize the application of relevant
physics. These processes apply in three cases; "at rest" for stationary particles, "along
step" for particle behavior that happens continuously along a given step, and "post step"
for behavior which relies on the final state of the step. Geant4 also allows for the creation of
geometries, which are coded first as logical volumes which define the shape and attributes

independent of its physcial location, and secondly as physical volumes which places the logical volume within the world volume at a particular location. The logical volume geometries are defined through the boolean combination of simple solids such as rectilinear boxes, spherical and cylindrical sections, toroid sections, and paralellepipeds. The material and detector properties are defined based on the logical volume within the code, and can be used to define sensitive detectors to extract track parameters upon interaction[9].

To facilitate the development of simulations for UCN detection and transport, a package known as Geant4UCN was developed by Gabriele Cosmo et al. This package compiles the relevant physical processes for low energy neutrons into easily modifiable classes. In particular, it incorporates neutron beta decay, forces from gravity and time dependent magnetic fields, 1/v absorption and upscattering cross sections, multiple scattering, spin tracking, and material boundary interactions. Spin tracking is handled in the adiabatic case, and records a plus or minus spin relative to the UCNTimeDependentMagneticField as defined in the code. The material boundary parameters are of particular importance for transport simulations, and Geant4UCN simplifies these interactions into the parameters: Fermi Potential, Reflectivity, Diffusivity, Loss, Spinflip Probability, and the various cross sections for bulk propagation. Furthermore, shutter definition is enabled such that physical volumes have these parameters toggled during particle transport[6].

3.2   A Simulated Lifetime Experiment

Prior to the completion of the UCNτ experimental apparatus, it was necessary to simulate the experiment's performance in Monte Carlo. To accomplish this, a Geometry Description Markup Language (GDML)[8] geometry definition file was created to model the planned experiment for use in Geant4. Particles were created in the primary generator with the $v^{2.7}$
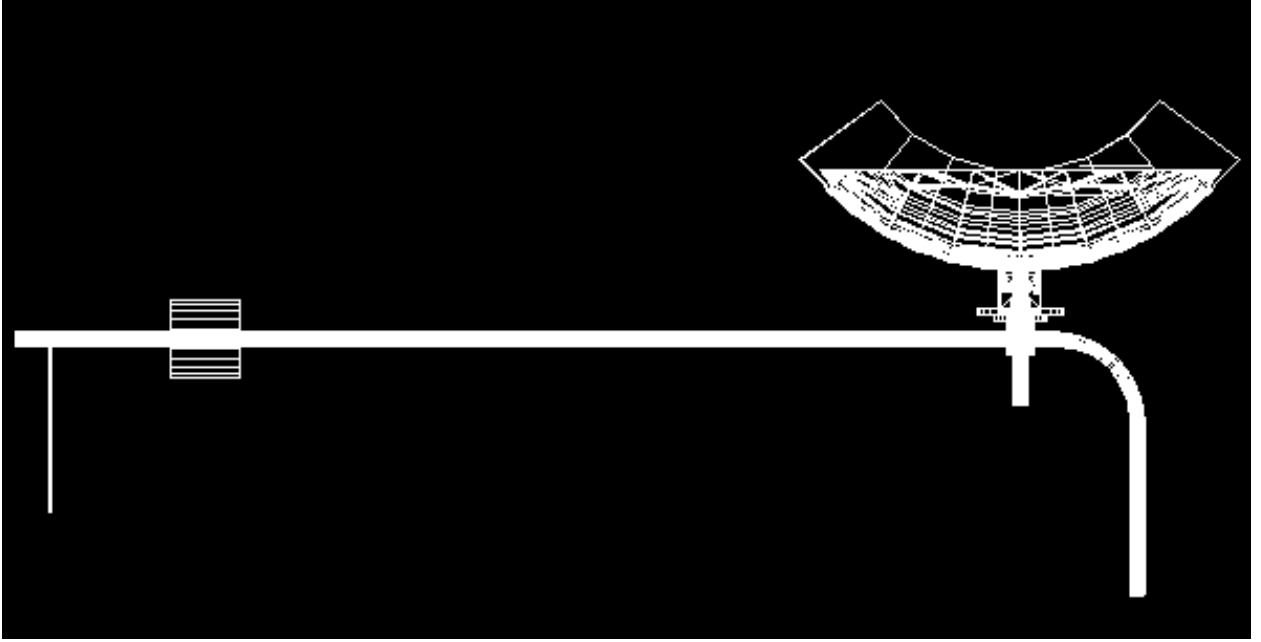
Figure 3.1: Wireframe visualization of the Geant4 model of the UCNτ experiment.

distribution fit mentioned in the previous chapter (Fig. 2.2) uniformly across a 2d plane 20cm upstream of the gate valve monitor aperture. The rest of the geometry maps the guide structure planned to be used, with a straight stainless steel guide with a meter of diamond-like carbon (DLC) in place for the spin flipper field, the cross assembly at the end of the steel guide, an approximated trap volume above the cross assembly, and an elbow down to a far detector on the downstream exit of the cross assembly, as seen in Figure 3.1. The materials used have been summarized in Table 3.1. Any zero values within the table indicate that these parameters have little impact on the simulation results. Notably, as the polarization was set through definition in the primary generator as opposed to arising through physical acceleration, the Zr window within the PPM magnetic field region was set to a Fermi potential of zero to account for the acceleration of the particles. The geometry within the cross assembly was reproduced exactly from chematic models, aside from hexagonal bolts being coded as cylindrical. While the vacuum jacket was able to be coded in a highly accurate manner in the areas in the path of UCN, the asymmetric array was

unable to be simply defined. The shape of the Halbach array is defined as two toroid sections, one from a toroid with major radius 1m and minor radius 0.5m and the other with major radius 0.5m and minor radius 1m. Since the improper torus is unable to be defined as a physical volume in the GDML file, that half of the array was procedurally generated to follow the appropriate shape; the other half had no such issue and was defined as a normal toroid section. For similar reasons, the magnetic field interaction of the UCN with the Halbach array was not coded, but rather the magnets were defined as perfect reflectors with a spin value check on interaction to incorporate the effect of spinflips on trappability. Given this deviation from reality, any finer details of in-trap particle trajectory simulation were handled by a parallel non-Geant4 simulation carried out by Dan Salvat.

Material	V_F (neV)	Diffusivity	Loss per bounce	Spin Flip
Stainless Steel	186	0.03	1.25×10^{-4}	1.25×10^{-3}
Copper	168	0.04	1.55×10^{4}	1.7×10^{-5}
Aluminum	54	0	1.86×10^{-5}	0
Nickel	252	0	2.6×10^{-4}	0
Zirconium	80	1.0	8.09×10^{-6}	0

Table 3.1: Properties used in the material definitions for Geant4.

The detectors in the physical apparatus were simulated as sensitive detectors which recorded the position, momentum, energy, spin, particle ID, and timestamp of any particle that encounters those volumes and then removed the particle track. The geometry was irrelevant beyond the exposed surface to the UCN volume so these detectors were modeled as a totally absorbing disk covered by a window of the appropriate thickness. In addition, a scorer was placed at the trapdoor with the same outputs but without destroying the particle for the sake of tracking the flux through the trapdoor. This scorer allowed for the measurement of particle states as the UCN enter the trap as well as a means of tallying the trap population together with the particle death timestamps for those UCN which decayed or were otherwise destroyed within the trap. To track the population, 50000 UCN were

34

generated at t=0 and the momentum and timestamp of each particle was recorded. The interval for a particle within the trap could be extracted by identifying all points at which the particle crossed the scorer with $p_z < 0$ as well as the final timestamp in the particle track. By matching each of these points with the most recent preceding value for that particle ID crossing the scorer with $p_z > 0$, summing the collection of intervals, and dividing by the total number of events, we obtain the probability over time $P(t')$ that a particle can be found in the trap, as seen in Figure 3.2. If we establish a generation curve G(t), then we can infer the trap population by convolving:

$$P * G(t) = \int_{-\infty}^{\infty} P(T)G(t - T)dT. \tag{3.1}$$

An example of this can be seen in Figure 3.2 (right) in which G(t) is represented by a boxcar function from t=0 to t=230 with height normalized to represent a source density of 25 UCN/cc. This trap population analysis has been improved by adding a start time in accordance with the generating function; in this case, $t'_0 = t_0 + 230.0 \cdot G4UniformRand() * s$. This yields a smoother population curve at higher statistics, and will be used for subsequent runs.

Another use for the trapdoor scorer is to investigate the phase space of the particles entering the trap. The energy of these particles is particularly relevant because any UCN with $E_{UCN} > 50$neV at the trapdoor will be untrappable or marginally trapped. Typically for the standard simulation geometry, the trap UCN spectrum extends up to around 150 neV, with a small proportion of the curve below the 50neV threshold. An investigation was made into the effects of elevating the trap height above the beamline by some additional amount. An s-bend was added to the simulation upstream of the cross assembly as shown in Figure 3.3. The length of the straight section between the two elbows was altered to
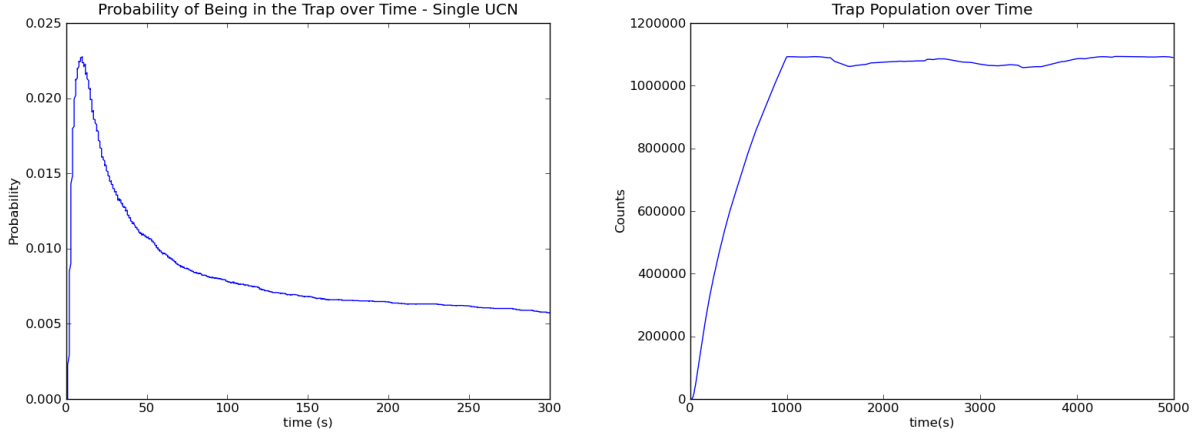
Figure 3.2: Left: Probability of a particle being in the trap vs the time since that particle's generation. Right: Trap population derived from the probability plot.

compare the h=0 case with an additional elevation of 500 mm. The resulting shift in trap spectrum can be seen in Figure 3.4. While the percent of generated particles remains comparable, there is a reduction to untrappable UCN in the spectrum, which could have some use in controlling the systematics. However, in terms of implementation, the only means by which this could be utilized to control the marginally trapped UCN population would be to either elevate the trap an additional 600 mm such that no UCN exist above the trappable range or to allow the height to be modifiable such that various proportions of untrappable to trapped populations could be measured. Both of these were physically unachievable and as such this study did not result in any alteration to the geometry.

The efficiency of transport will depend on the parameters of the guides being used to carry the UCN from the source to the trap. When planning the guide setup, 4 inch and 3 inch diamaeter guides were available; while the larger guide size offered fewer wall interactions per length, there were existing 3" diameter bottlenecks at the PPM and cross assembly entrance. On top of this, there was an option whether we would use stainless steel guides which offered a higher Fermi potential and lower loss per bounce or copper guides which offered a lower spinflip chance per bounce. We ran a simulation comparing the four guide

36
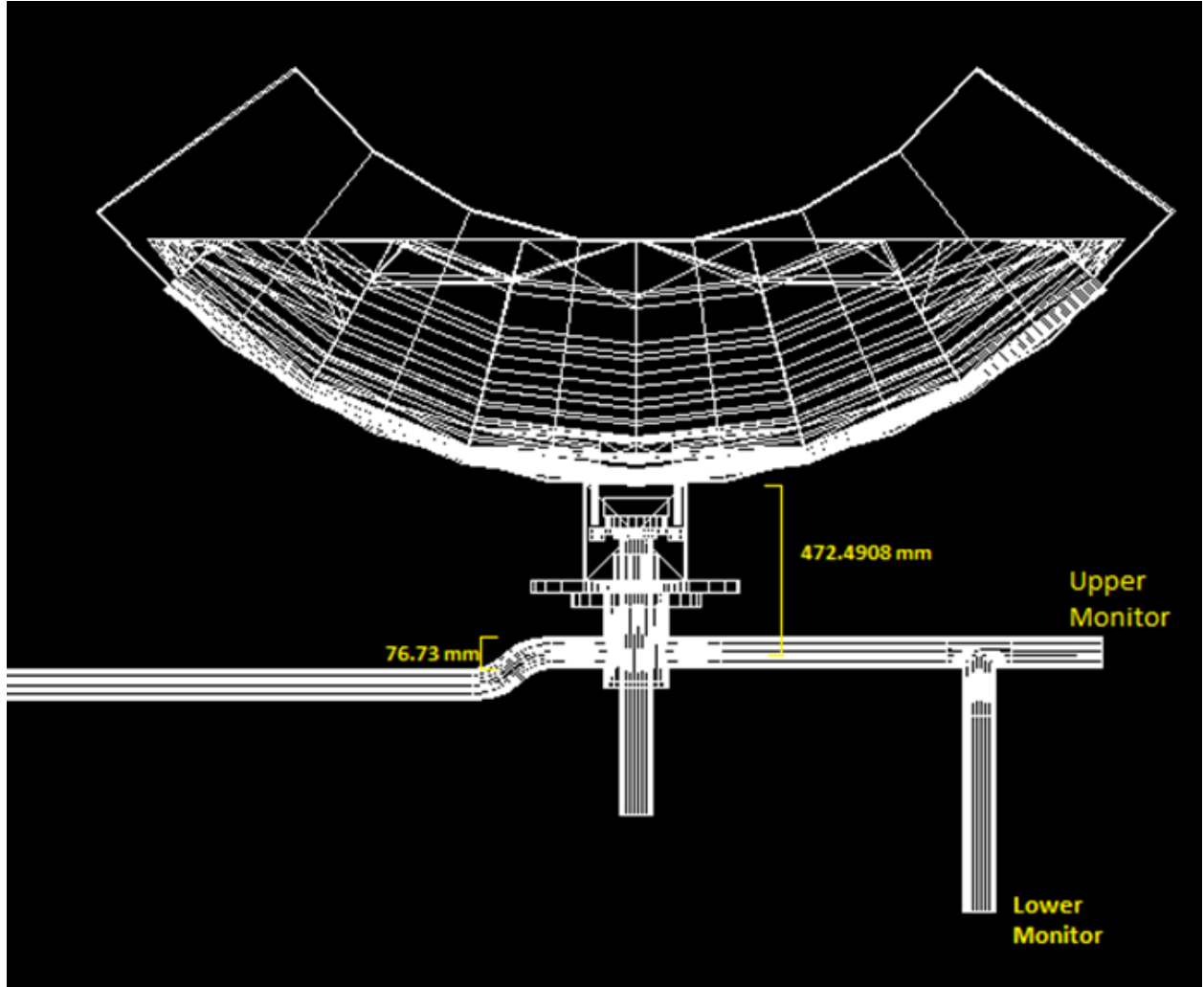
Figure 3.3: Geant4 model of UCNτ with added elbow for additional height.
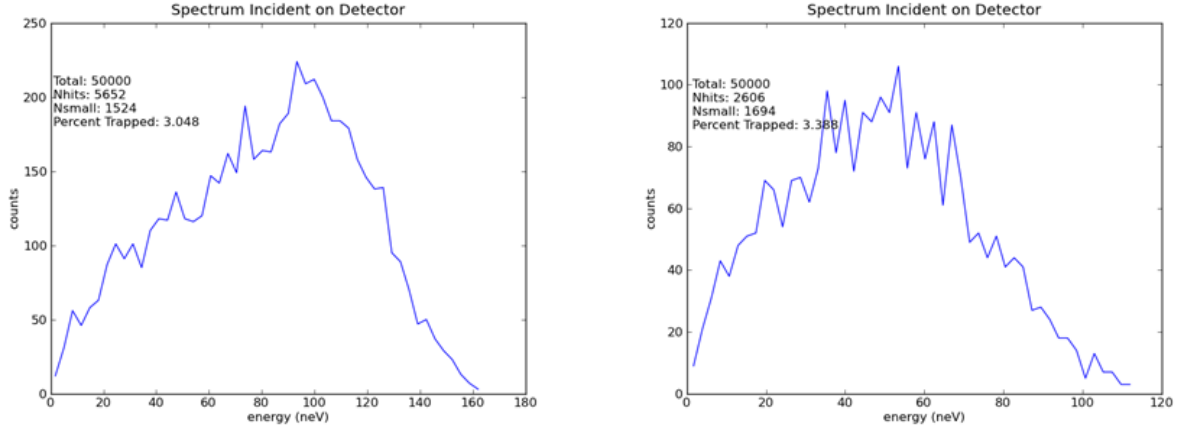
Figure 3.4: Histogram of the energy of particles at the trapdoor when h=0 (left) and h=50cm (right)

components, and the result showed that copper was superior to stainless and that the larger guide diameter resulted in an improved trappable population (see Table 3.2). However, this assumed a simple coupling between the 3 inch and 4 inch guides, which was not successfully implemented, and as such the final decision was to go with the 3 inch copper guides.

Guide	3" SS	4" SS	3" Cu	4" Cu
Guide Eff.	0.113	0.236	0.102	0.227
Polarization Eff.	0.839	0.864	0.995	0.998
Trappable E	0.182	0.192	0.228	0.242
Total Eff.	0.021	0.045	0.023	0.055

Table 3.2: Comparison of guide materials and diameters in terms of guide efficiency, polarization efficiency, and proportion of UCN within the trappable energy range. Simulation used 50,000 events per run

In the process of simulating UCN transport, it became clear that there were several issues with the cross assembly. Firstly, the cross section of access to the trap from the guides was very small, resulting in very long trajectories within the cross assembly before a UCN entered the trap. Compounding this was the fact that the cross was stainless steel which had a high depolarization probability compared to other materials in the system. Finally, the location of the trapdoor in the open position created the issue of large irregular

38

magnetic fields directly in the path of the UCN to the trap; analysis done by Chen-Yu Liu demonstrated that these errant fields would inevitably create field zeros which amplified the chance of UCN depolarization during the trap fill. In the interest of investigating alternate forms of cross assembly, several new geometries were simulated. In particular, we investigated designs which utilized a more direct line of approach into the trap which could replace the trapdoor once it had been retracted by a far greater degree. As a toy model of such a design, a geometry in which the cross assembly was replaced with a copper elbow directly feeding into the trap was created and compared to the earlier population curves. This toy model showed a factor of 4 increase in the trappable population (Fig. 3.5), which validated the concerns over UCN access to the trap.

The implementation of this idea was more involved, as the elbow prevented the trap from being able to be closed. The idea of having the trapdoor retract fully below the beamline and having a movable electropolished copper flap redirect the UCN vertically into the trap by covering the trapdoor at a 45° angle resolved the issue, and the final design is shown in Figure 3.6.

3.3   Guide Test Analysis

In September 2013, the assembly of the UCN guides was accompanied with a series of measurements to determine the relationship between UCN transport and the equilibrium density within the trap and to determine the parameters that characterize the UCN transport system. The transport system was divided into three regions of interest as in Figure 3.7 and measurements were taken at the boundary positions 1 through 4. There were four types of measurements done at each location: A simple transmission measurement through that region (NP); a transmission measurement with a spin-sensitive
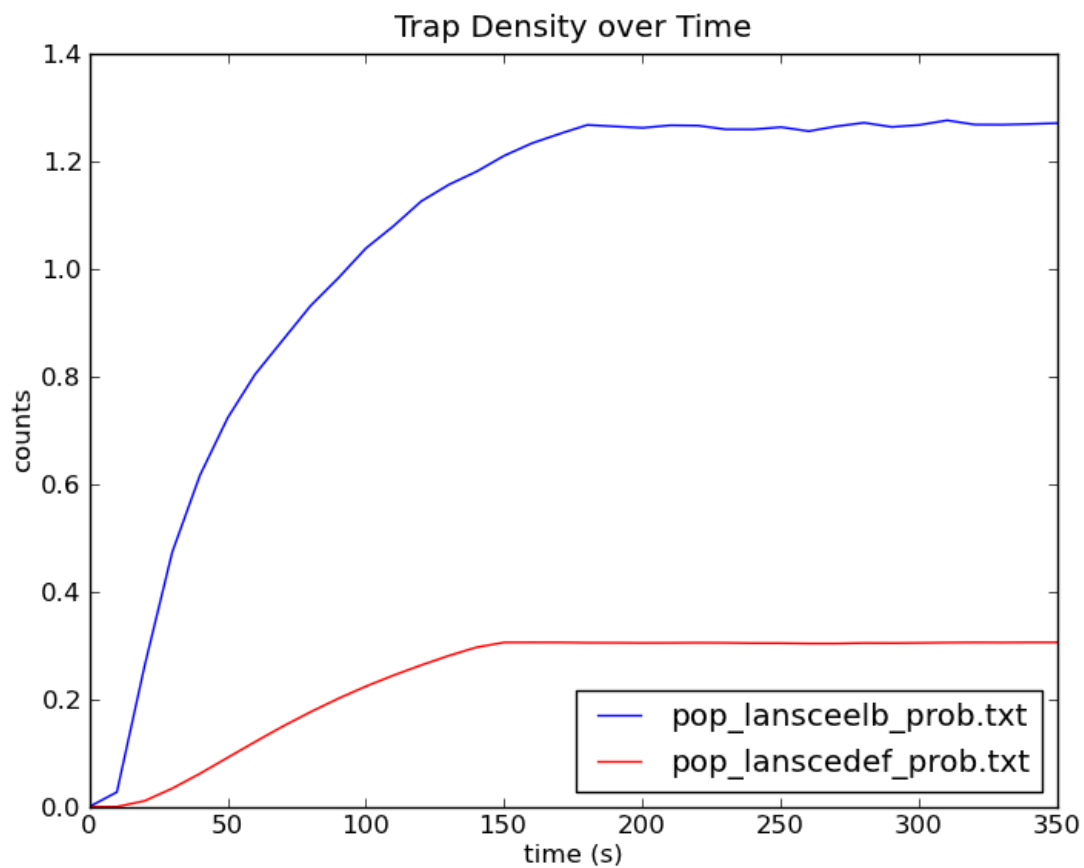
Figure 3.5: Population plot with the default cross assembly (red) and with a direct elbow into the trap (blue). Y axis scale is arbitrary.
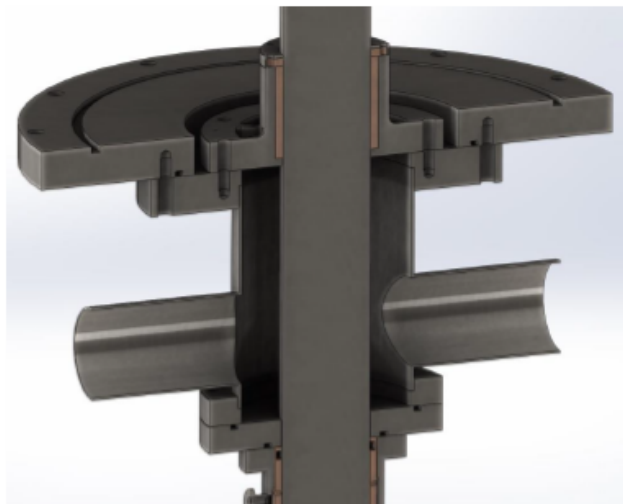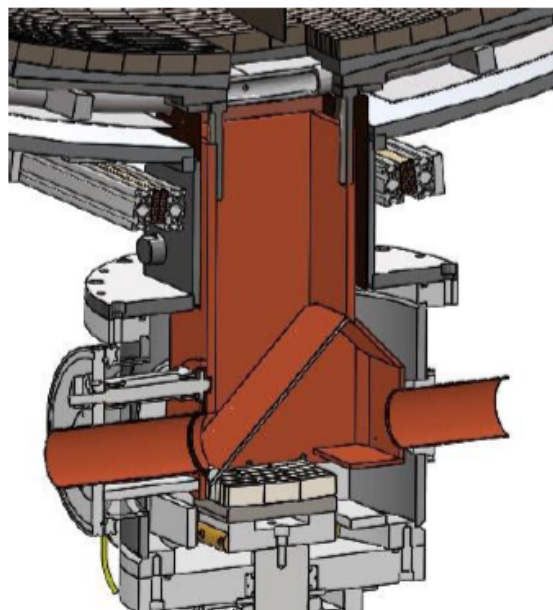
Figure 3.6: Left: Original cross assembly design. Right: Improved cross assembly with fully retracted trapdoor and moving angle flap.
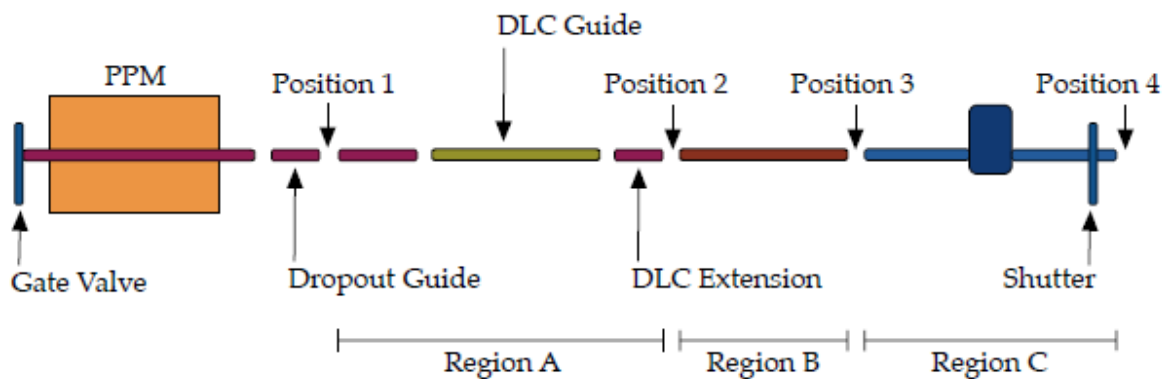
Figure 3.7: Diagram of the UCNτ guide geometry with the sections defined for the 2013 guide tests.

Region/Run	Transmission
Region 1 NP	0.4945 ± 0.0032
Region 2 NP	0.9210 ± 0.0076
Region 3 NP	0.3396 ± 0.0026
Region 1 SP	0.7512 ± 0.0053
Region 2 SP	1.0358 ± 0.0104
Region 3 SP	0.3828 ± 0.0039
Region 1 Fe	0.4524 ± 0.0024
Region 2 Fe	0.8968 ± 0.0075
Region 3 Fe	0.2142 ± 0.0019
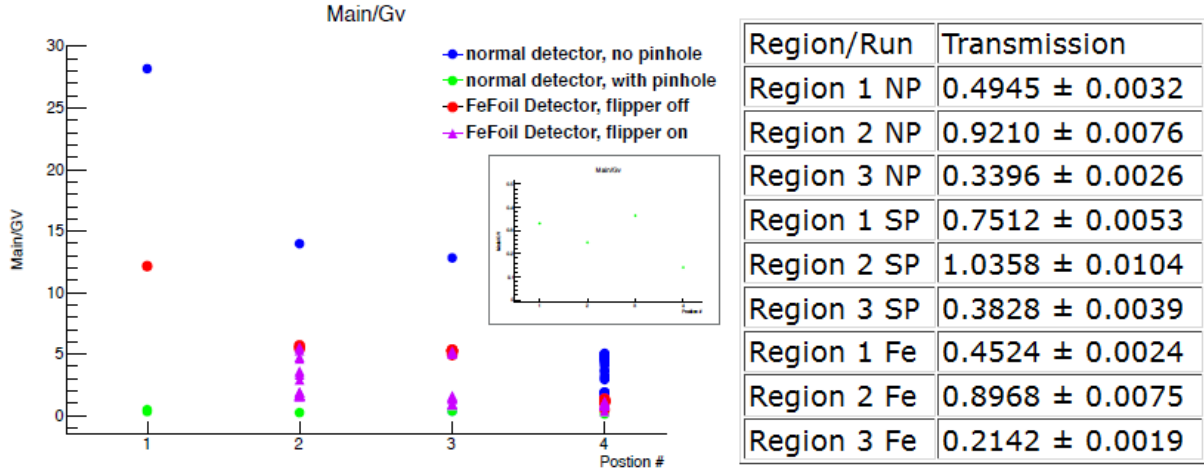
Figure 3.8: UCN detected at each position (plot) and transmission ratios (table) for each type of run from the 2013 guide tests.

detector for measuring depolarization (Fe); a transmission measurement with a pinhole present at one end (SP); and a bottling measurement, where a pinhole is present on either side of the region and the region is filled to equilibrium (DP). Each measurement was intended to separate the effects of each guide parameter as much as possible, though some overlap is still present.

The results of this test are summarized in Figure 3.8. The largest transport losses occurred in Regions A and C, with the latter expectedly demonstrating the inefficiency of the stainless steel cross assembly. The fact that the pinhole transmission measurements are significantly larger for Regions A and B suggests that the specularity of the guides is suspect. In order to determine the guide parameters, a Geant4 simulation geometry was created to match the guide test in its various positions. The parameters to be tested are the Fermi potential (FPOT), loss per bounce (LOSS), and diffusivity (DIFF). The goal is to scan the effect of modifying each of these parameters on the transmission in the various states, and to match to the experimental results to find a region of agreement. For the direct measurements, LOSS and FPOT are difficult to distinguish, as both have

42

Run#	Region	Load/Drain timing	Lifetime	Uncertainty
33	A	60s/90s	13.60	5.69
109	B	90s/120s	21.63	5.56
174	C	40s/60s	13.68	8.48
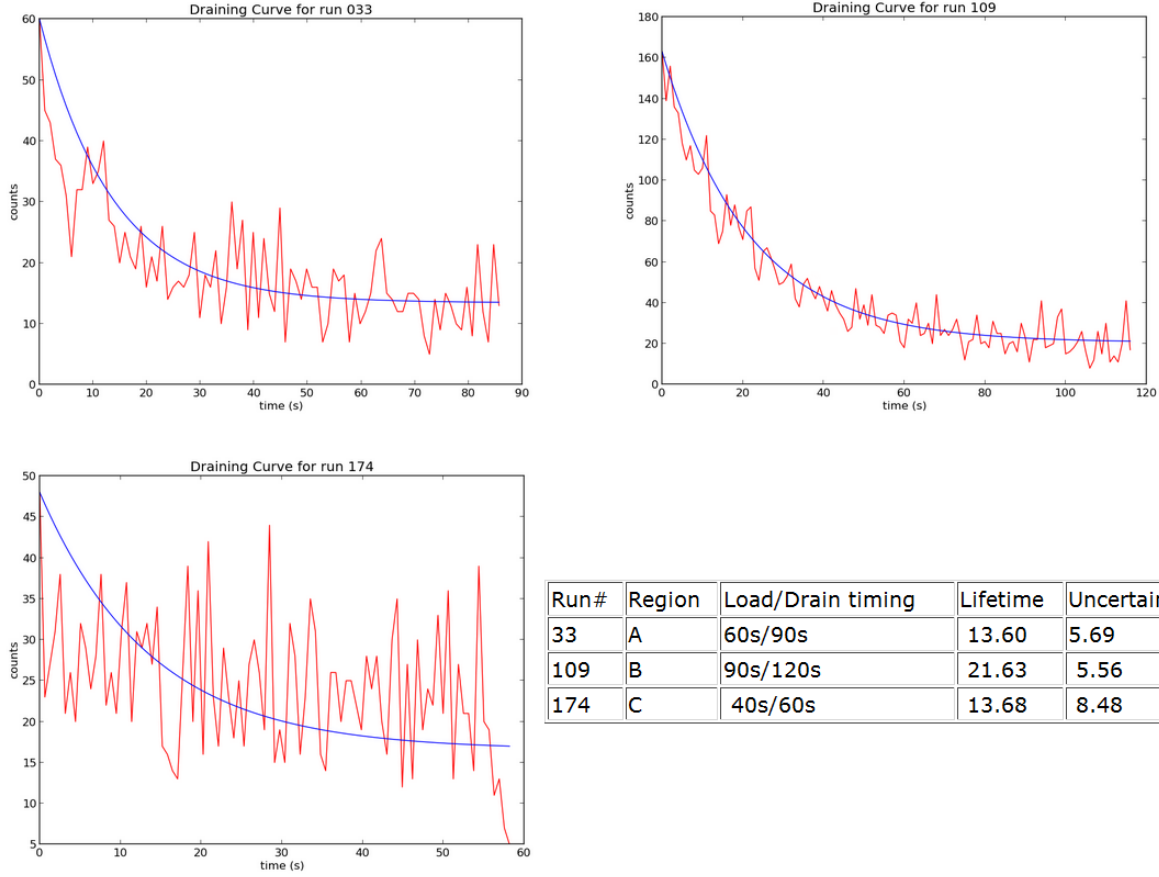
Figure 3.9: Signal from each region's bottling (two pinhole) measurement, with fits.

comparable resulting losses in the absence of spectral sensitivity in the detector. Since both can result functionally from imperfections in the guide coating, it is necessary to use the bottling measurements to determine the FPOT before proceeding with the direct transmission measurements. Figure 3.9 shows the fitted bottling lifetimes in each region. Unfortunately, the statistics for these measurements proved insufficient to establish an improvement on the bounds set by theoretical considerations.

Due to the ambiguous results from the bottling measurement, the direct measurements scan over FPOT as an effective Fermi potential with built in loss factor as a first order determining factor for guide quality. Between this effective FPOT and DIFF, a matrix of

reasonable values was created for the guide parameters and a two-variable scan was carried out on the properties of the copper guides. The resulting region of interest for a coarse scan can be seen in Figure 3.10. There are two regions of agreement, with the first occupying an area around (DIFF,FPOT) = (0.95, 120neV) and the other around (0.5,100neV). Given the pinhole results referenced above, it is likely that the lower DIFF region is trustworthy; however, in either case, the effective FPOT is much lower than the expected value of Cu ($V_F \approx 168neV$). Furthermore, the likely presence of a cuprous oxide layer ($V_F = 139.6neV$, See Appendix 2), is insufficient to explain this low value purely in terms of its effect on the Fermi potential. As such, we conclude the existence of an anomalous loss factor, supported by visible imperfections on the guide's interior surface. For the subsequent experiment, new copper guides were prepared as part of an overhaul in transport guide setup.

The spin depolarization measurement was analyzed independently to the other guide parameters. In particular, due to the ambient fields present from neighboring experimental magnets, notably the UCNτ holding field coils and the UCNA experiment's AFP magnet next to the transport system, it was necessary to make spin contrast measurements at various field configurations in order to ensure that polarization could be preserved regardless of the presence of external field sources. Figure 3.11 shows the different field configurations used in this study. The contrast was obtained by using a modified ^{10}B detector with a magnetized iron window in place of the usual aluminum window. Such a detector should accept solely high field seeking UCN, allowing the measurement of only one spin state. From Figures 3.12 and 3.13, we see that the majority of the depolarization occurs in Region C, providing another motivation for the replacement of the cross assembly as mentioned in the previous section. It is clear that some field configurations are harmful to the polarization, with the configurations providing the minimum contrast being configuration 5 when the AFP is off and configuration 10 when the AFP is on. This result
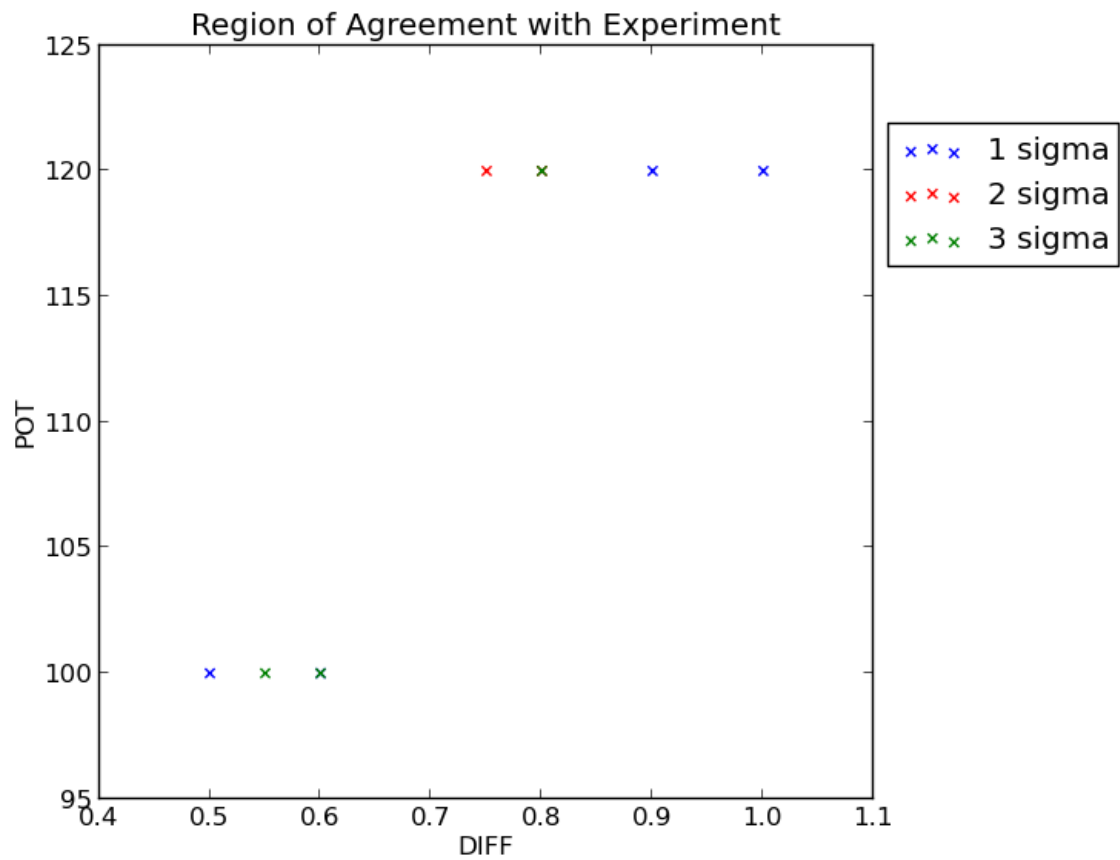
Figure 3.10: Region of interest from the two parameter coarse scan of the Cu guide parameters.

Ref#	flipper field	trap holding field	UCNA AFP Magnet
0	off	off	off
1	+	off	off
2	−	off	off
3	off	+	off
4	+	+	off
5	−	+	off
6	off	−	off
7	+	−	off
8	−	−	off
9	off	off	off
10	+	off	on
11	−	off	on
12	off	+	on
13	+	+	on
14	−	+	on
15	off	−	on
16	+	−	on
17	−	−	on

Figure 3.11: Description of each field configuration used in Figures 3.12 and 3.13.

allows us to set the field states to minimize the deleterious effects of ambient magnetic fields during an experimental UCN fill.
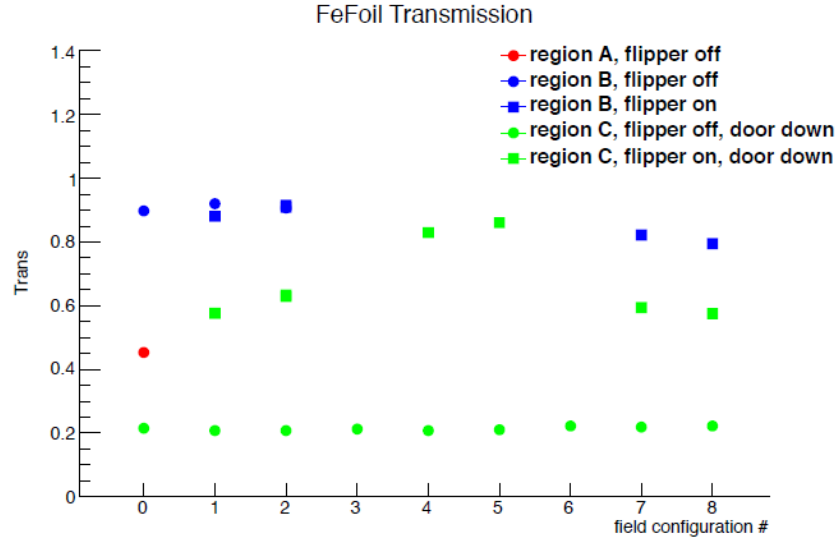
Figure 3.12: Transmission ratios through each region using spin-sensitive Fe foil detector as a function of different holding field configurations (Fig. 3.11).
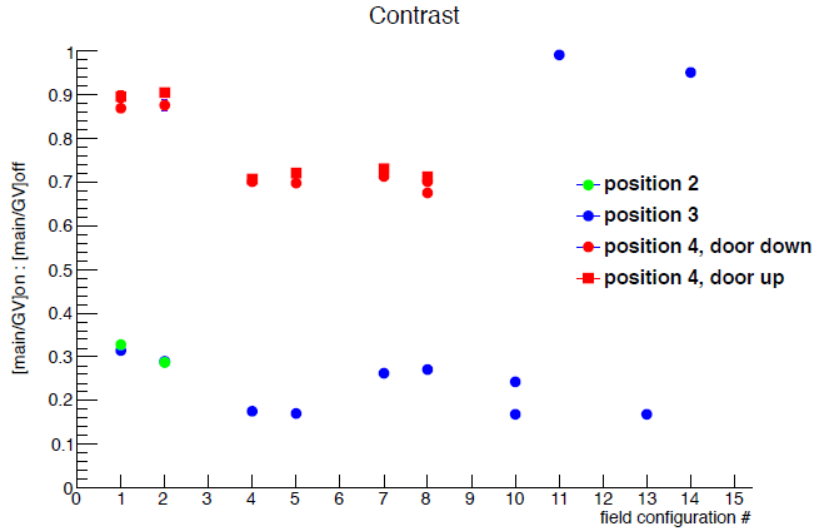
Figure 3.13: Observed spin flipper contrast as a function of different holding field configurations (Fig. 3.11).

CHAPTER 4

DETECTOR DEVELOPMENT

4.1   Boron Detector

In order to detect UCN in the experimental run, we utilize the $^{10}B(n, \alpha)$ capture reaction
at low incident neutron energies. There are two branches of particle production which can
be used to detect a capture event:

$$^{10}B + n \rightarrow \begin{cases} ^7Li + \alpha & Q = 2.792 MeV, 6\% \\ ^7Li^* + \alpha & Q = 2.310 MeV, 94\% \end{cases} \qquad (4.1)$$

Since the incoming energy is small compared to the Q value, we can approximate that the
outgoing particles carry all the energy of the reaction and are emitted in opposing
directions.[15] The capture cross section on ^{10}B for 2200 m/s neutrons is 3835 barns; in
accordance with the $1/v$ dependence of the cross section, we can infer that the cross section
on the level of 5 m/s is around 1.7 Mb, with a mean free path of 44 nm. Pure ^{10}B has a
fermi potential around $V_F = -7.4 - 39.2i$ neV and pure ^{11}B has a $V_F = 222.5$ neV. Natural
boron contains roughly 19.8% boron-10 with the rest being boron-11; however, high purity
^{10}B can be obtained at purity levels above 96%.
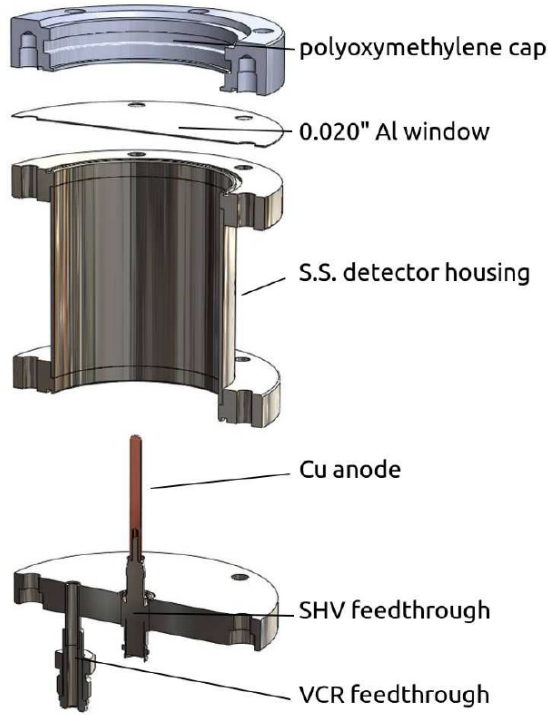
Figure 4.1: Schematic of the ^{10}B UCN detector. Connections between each component sealed with o-rings (not shown).

To utilize the boron-10 capture reaction for neutron detection, we create an ionization chamber which is coated on the interior surface with high purity ^{10}B. Exactly one of the particles should be emitted into the chamber from a wall interaction, at which point it will ionize the CF$_4$ gas within the volume. The construction of this detector is shown in Figure 4.1. The ionization chamber consists of a 7.620 cm stainless steel tube with outer diameter of 7.620 cm and 1.65 mm thick walls. The downstream cap contains a high voltage feedthrough to a 4.76 mm diameter copper anode which extends 5.080 cm into the chamber, as well as a VCR feedthrough for vacuum pumping and for introducing gas into the cell. The upstream end of the chamber consists of a 0.51 mm thick aluminum window sealed by o-ring surfaces with a polyoxymethylene cap to isolate the conducting surface of the detector from the UCN guides.

The chamber is coated using a mixture of 0.0575 ($\pm$ 30%) grams of ^{10}B powder suspended in a 4 gram mixture of acetone and polystyrene. This mixture is then sprayed manually to coat the interior of the detector volume. Three coats of this spraying process results in a layer thickness around 1.54 ± 0.46 μm, with levels of roughness which have not been measured. As this thickness far exceeds the mean free path of a UCN in boron, we can assume that the UCN do not penetrate deeply into the boron layer. As such, we can treat the Fermi potential seen by the UCN as a step potential with height $\Re(V_F)$, with the associated reflection probability $R = \frac{k_0 - k_1}{k_0 + k_1}$, where $k_i = \sqrt{\frac{2m}{\hbar^2}(V_i - E_{UCN})}$. Averaged over a smooth surface for all θ, this gives a reflection probability of 16% for a 50 neV UCN.

The ionization volume is filled with 500 mbar of CF_4 and biased to 500V. The pulses are measured using charge-sensitive preamplifiers, amplified by $6\mu s$ time constant spectroscopy amplifiers and then read into a multi-channel analyzer. Calculations using SRIM2008 code[19] yield ranges of 3.03 mm and 3.63 mm for the alphas depending on branch and 1.68 mm and 1.89 mm for the ^{7}Li ions (see table 4.1). These are small compared to the distance between the anode and the wall, and as such we expect full deposition of energy into the gas.

To test these detectors, we compare directly against ^{3}He proportional counters by installing both types of detector to either side of an electropolished guide tee mounted on the source guide at the LANSCe UCN source. A gate valve is installed at the upstream end of the tee, ahead of which a small aperture leads to a multi-wire proportional counter for monitoring the incident flux of UCN. The pulse height spectra from the two detectors can be seen in Figure 4.2. Notable features of the boron detector spectrum include two prominent edges from the α and ^{7}Li from the 94% branch, as well as a much smaller edge from the ground state α. The signal from the ground state lithium is unable to be seen above the rest of the signal around 1.02 MeV. The efficiencies are measured by looking at the spectra for each
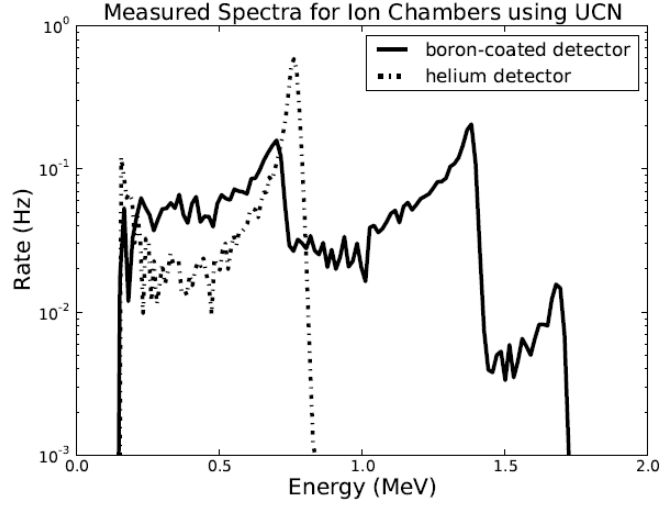
Figure 4.2: Comparison of the pulse height spectra from the ^{10}B UCN detector and the ^{3}He detector.

detector with the gate valve open and subtracting the background derived from an equivalent run with the gate valve closed. In order to calibrate energies, 5 mbar ^{3}He is introduced to the boron detector and the value of the resulting peak is matched to the known energy peak value from ^{3}He of 0.764 MeV. The resulting calculation shows that the boron detector signal is $(94 \pm 8)\%$ of that of the helium detector signal.

4.2 ZnS Detector

Ion	Probability	Energy (MeV)	Range in ^{10}B (μm)	Range in ZnS (μm)
α	47%	1.46	3.5	4.2
$\alpha(g.s.)$	3%	1.78	4.4	5.1
^{7}Li*	47%	0.84	1.8	2.3
^{7}Li	3%	1.02	2.1	2.5

Table 4.1: Maximum ion ranges for each emitted particle from ^{10}B capture with chances of being emitted in 2π, calculated using SRIM

While the boron ionization chamber detectors provide a cheap and easily constructed alternative to ^{3}He detectors, the use of a gas based detector for our experiment results in

51
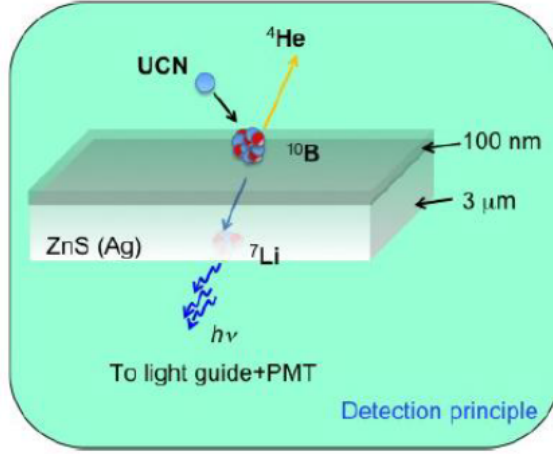
Figure 4.3: The ZnS-boron detector utilizes two thin films to produce scintillation light which is captured by a photomultiplier tube.[11]

the need to implement an aluminum window between the detector volume and the guide volume. In addition to introducing additional potential sources of leaks for the vacuum, this window creates a potential barrier for the UCN with potential $V_F = 54$ neV. As such, there is an energy-dependent efficiency loss which necessitates a 0.5 m drop distance to bypass. To remedy this issue, a new model of detector was designed which builds on the ^{10}B(n,α)^{7}Li capture reaction. Rather than using an ionization volume, the boron is coated on top of a luminescent layer of ZnS:Ag, which scintllates upon incidence of either the α or the ^{7}Li produced from the neutron capture (See Fig. 4.3). The lack of gaseous component removes the need for a material window and the outer ^{10}B film is exposed directly to the UCN volume. Based on the ion ranges from Table 4.1, we require the boron layer thickness to be on the order of 100 nm and the ZnS layer thickness to be on the order of a few microns. This will ensure full capture of UCN on the boron layer (95% at $3\lambda_{UCN}$), full escape of ions from the boron layer at most angles (no losses for $\theta < 86°$), and full deposition of energy into the ZnS layer. The light produced in ZnS is emitted at wavelengths peaking around 450 nm with a characteristic decay time of 200ns. The pulse height spectrum for

52
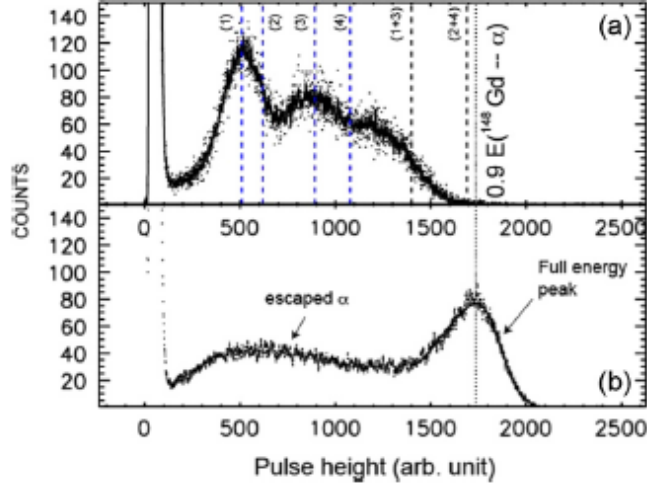
Figure 4.4: Pulse height spectrum for UCN capture on the ZnS (a) with location of peaks marked 1 through 4 for the corresponding ^{10}B capture products. Energy is calibrated to 90% of the peak from a ^{148}Gd α source, shown in (b).[11]

detected UCN is shown in figure 4.4.

In order to maximize the efficiency, it is necessary to optimize the thicknesses of each layer as well as the purity of the boron. To this end, we utilize the model of the single layer square 1D potential discussed in Appendix 2 to determine the reflection and transmission of UCN in the boron layer:

$$R = \left| \frac{(1 - \frac{k_2}{k_0}) \cos(k_1 d) - i(\frac{k_2}{k_1} - \frac{k_1}{k_0}) \sin(k_1 d)}{(1 + \frac{k_2}{k_0}) \cos(k_1 d) - i(\frac{k_2}{k_1} + \frac{k_1}{k_0}) \sin(k_1 d)} \right|^2 \tag{4.2}$$

$$T = \left| \frac{4 \frac{\Re(k_2)}{\Re(k_0)}}{(1 + \frac{k_2}{k_0}) \cos(k_1 d) - i(\frac{k_2}{k_1} + \frac{k_1}{k_2}) \sin(k_1 d)} \right|^2 \tag{4.3}$$

Where d is the thickness of the boron layer, k_i are defined as usual, and the ZnS layer is arbitrarily thick. The purity of the ^{10}B influences the value of the Fermi potential, which in turn influences k_1, the k value for the boron layer. A series of calculations was performed computationally using these formulae. The variation in boron purity showed a negligible

53
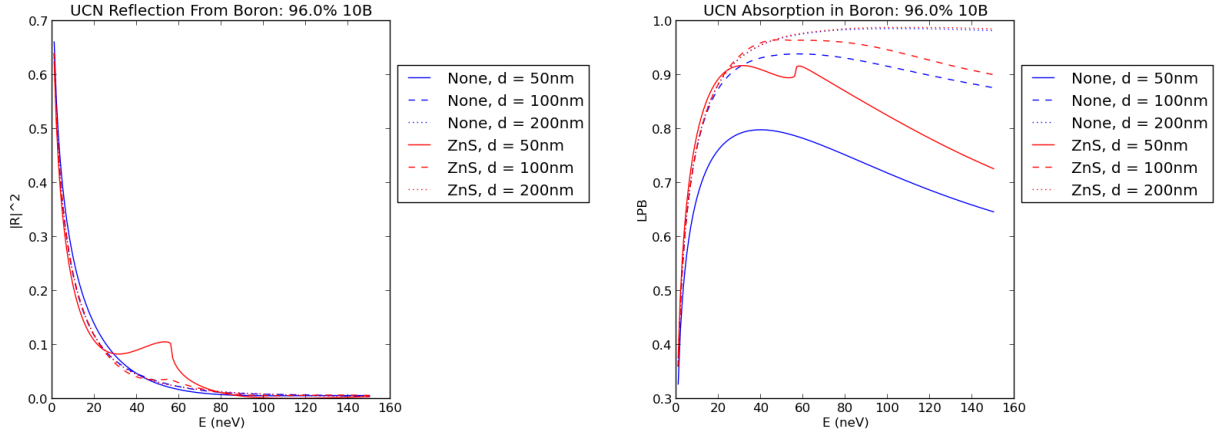
Figure 4.5: Reflectivity (left) and absorption (right) in the boron layer at 96% purity as a function of energy for various boron layer thicknesses. Red lines represent these values in the absense of substrate and blue lines represent an arbitrarily thick ZnS substrate on the far side of the boron layer.

effect above 96%, the minimum value assumed for pure ^{10}B powder. As the detector efficiency is expected to increase monotonically with boron purity, the rest of the calculations were performed with 96% purity ^{10}B (see Fig. 4.5). These calculations suggested that a minimum boron thickness of 100 nm should be used, with any increases being offset by the increased opacity of the thicker films to the ion products above 200nm. Detector films of various thicknesses were prepared to verify these data experimentally. The ZnS-boron detector was installed with one of the films onto a small aperture offshooting from the main UCN source guide for detection (see Fig. 4.6) and data were taken for a short period of time. In order to normalize the film areas seen by the incident UCN, a TPX screen (Polymethylpentane, Mitsui Chemicals) with a 6mm diameter hole was placed in front of each film to ensure consistent exposure area. The PMT was biased to -1.7kV and digitized directly. The resulting efficiency is plotted in figure 4.7, and confirms a saturation of efficiency at 100 nm. The fit depends on the thickness as $\epsilon(d) = 0.23\left(1 - e^{-d/29.3}\right)$, where d is the film thickness in nm.
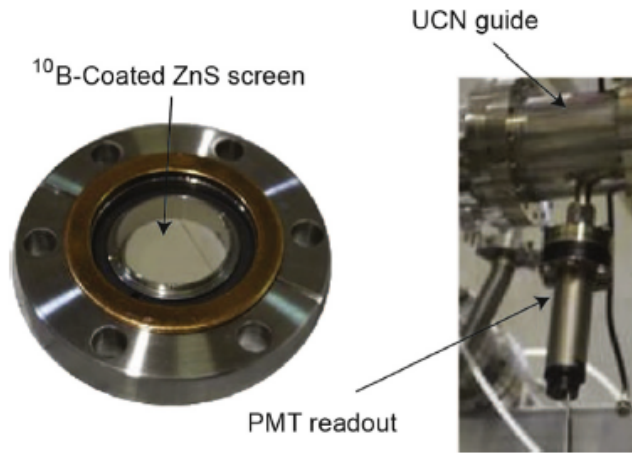
Figure 4.6: Setup for testing the various films prepared for the boron detector.[11]
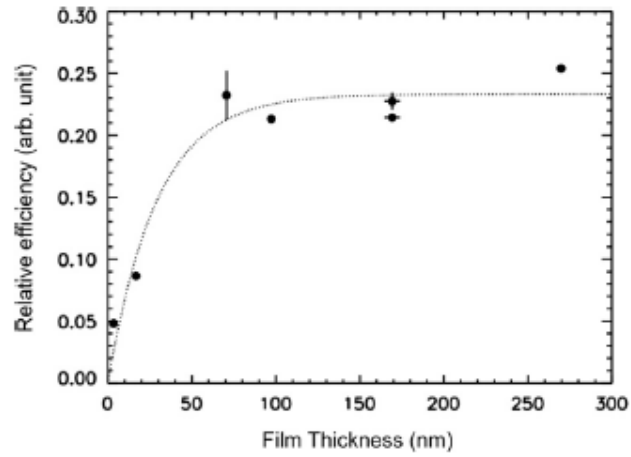
Figure 4.7: Relative UCN efficiency as a function of boron film thickness, with fit.[11]

Figure 4.8: Decay scheme of Vanadium-52 from the NNDC.

4.3   Vanadium detector

In order to measure the trapped UCN in situ, a vanadium foil based detector was designed to be inserted from above. Vanadium has a high neutron capture cross section as well as a small, negative Fermi potential, which makes it highly effective as a neutron absorber. Upon capturing a neutron, the vanadium-52 decays by beta emission into chromium-52 with a subsequent emmission of a 1434keV gamma with 100% branching ratio:

$$^{51}V + n \rightarrow ^{52}V$$

$$^{52}V \rightarrow ^{52}Cr^* + e^- + \overline{\nu}_e$$

$$^{52}Cr^* \rightarrow ^{52}Cr + \gamma(1434.06keV) \tag{4.4}$$

The lifetime of the ^{52}V beta decay is 324 s [13]. By measuring the coincident beta and gamma products, it is possible to reconstruct the UCN count from the decay curve of the Vanadium. A 12" × 4" vanadium foil is set into an aluminum frame and suspended over

56

the trap by an aluminum rod appended to an electric actuator with 1m range. In the fully extended position, the vanadium extends to the bottom of the Halbach array just above the trapdoor. When fully retracted, the vanadium sits at the center of a vertical extension of the vacuum jacket. Parallel to the foil are seated a pair of scintillator paddles for beta detection, one on either side of the vanadium. The edges of each paddle are lined with wavelength shifting optical fibers coupled to a photomultiplier tube for collection of the scintillation light. Exterior to the vacuum jacket extension are a set of ten NaI gamma detectors arranged in two stacks as seen in Figure 4.9. The full detector housing is surrounded on all sided by 2" thick lead shielding with the exception of a rectangular opening for the actuator arm. For each measurement cycle, the vanadium is lowered into the trap to absorb all surviving UCN and is then raised back into the detector housing. For a typical counting time of 1000s, the decay products from the vanadium decay are counted in coincidence and the total integrated counts are recorded. A detailed discussion of this counting and the backgrounds associated with this measurement follows in the next chapter.
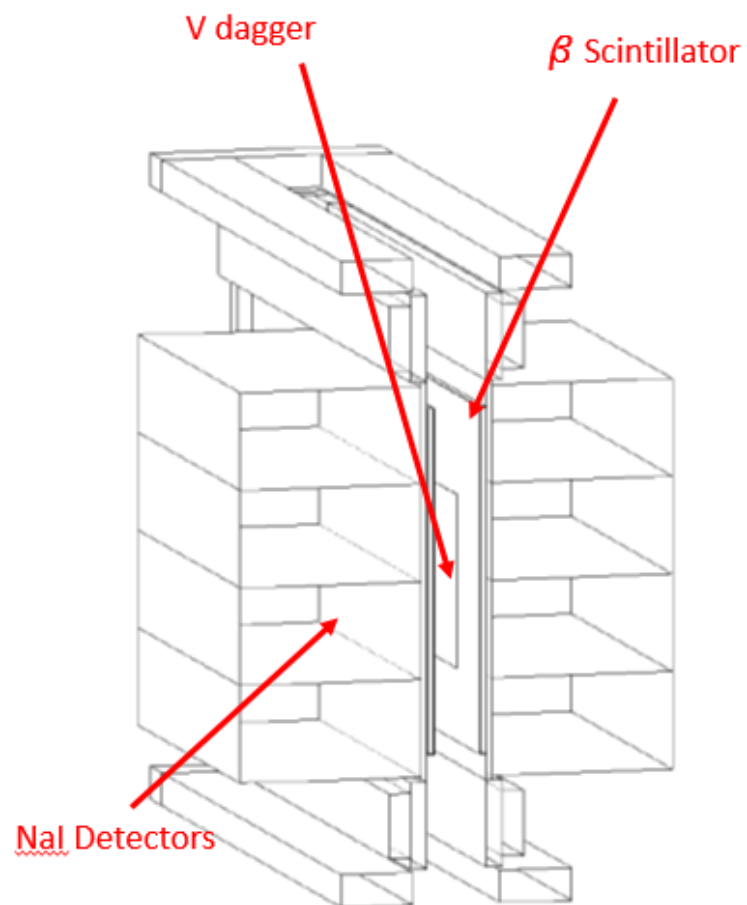
Figure 4.9: Detector housing for the vanadium detector when fully retracted. Two of the NaI detectors are not shown.

CHAPTER 5

BACKGROUND STUDY

5.1   Overview of Analysis Script

5.1.1   Data Layout and Retiming

During the 2014-2015 run cycle, we collected data on the UCNτ experiment which the
DAQ system output in both .root and .flat (plain text) formats. The latter format is the
basis for the analysis script, and records the information per run as seen in Table 5.1.

Column	Data
0	Channel
1	Real Time
2	Timestamp
3	Energy
4	IOreg

Table 5.1: Layout of data in .flat files

The first step of the analysis is the retiming. Due to a known bug in the DAQ's
reconstruction of the real time from the more reliable timestamp value, there are gaps in
the real time values in the flat files as generated. It is important to ensure accuracy in
timing to 10 ns resolution, as that is the minimum coincidence window used. Since the
timestamps are accurately recorded and the data are sufficienty dense in time, it suffices to

reconstruct the real time by implementing a rollover counter for each channel. We can greatly benefit from the inclusion of a regular 5MHz timing pulse in the DAQ system, recorded in channel 16. For each channel, we can reconstruct the realtime as:

$$t_{real} = (timestamp + (maxclock \cdot i_{rollover})) \cdot t_{bit} \qquad (5.1)$$

where $maxclock$ is the maximum timestamp value before rollover and t_{bit} is the precision of the timing clock, that is, 2 ns per bit. Whenever the timestamp decreases in value, the rollover counter $i_{rollover}$ is incremented by one. After performing this computation, the value is compared to the most recent ch16 time and, in the event of disagreement by more than the rollover time period, adjusted to the correct time window by adjusting the rollover counter.

5.1.2 Formatting and Coincidence

Once the files are retimed, it is necessary for both ease of use and for minimizing memory use during analysis to adjust the format of the data. The formatting script reads in the retimed .flat files and outputs the timing and energy of each coincident beta event in .npy format[1] . As such, the major role of this script is to perform coincidence selection on the data retimed by the previous script. To accomplish this, the data are split according to channel number, and the real time and energy are saved to that array. Each channel is then checked to verify the correct ordering by increasing time value. The relative monitoring data from the gate valve monitor (ch0) and the standpipe monitor (ch3) are then saved to their respective output files for later use in background and normalization calculations. Subsequently, an array is formed with the two beta channels (14,15) and the ten NaI

---

[1].npy formatting saves the data as a binary file in the structure of a python array, which can be read much more quickly by subsequent analysis scripts.
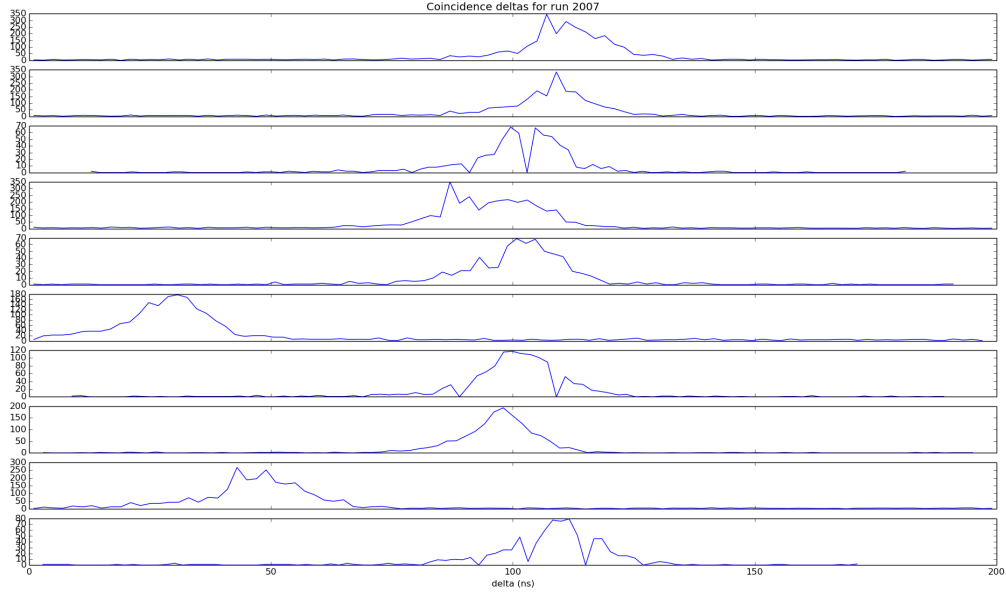
Figure 5.1: Difference in timing between beta and NaI events within the same $1\mu s$ window in each channel.

channels (4-13), with each event tagged according to detector type and the combined array sorted by increasing real time. Beta events with zero energy are ignored as nonphysical. In the first coincidence method used, the script then begins its coincidence finding subroutine, using this data array and the values for coincidence window $\Delta t = 100$s and offset $\delta t = 100$s based on Figure 5.1. The subroutine scans through the events until a beta event is found. The event immediately before and the one immediately after are then checked to see if they are (a) a NaI-type event, (b) have a time difference $|t_{beta} - t_{NaI} + \delta t| < \Delta t$, and (c) if the event energy satisfies any specified energy cuts. The time and energy of the beta event is then saved into the array of accepted coincident events, along with the energy of the coincident NaI event[2]. Once this has been done for all

---

[2]There is some explanation needed for the energy chosen. Naively, the energy of the closest event is the most "correct" value for the NaI energy associated with the coincidence. However, since the NaI spectrum of the coincident events is the focus of this analysis, this has been edited to reduce redundancies in the output spectrum. In its current form, the NaI energy for the coincidence if both surrounding events are within the window is chosen to be the value of the subsequent event if that is closer in time or if the previous event has

61

beta events, the entire output array is saved to a .npy output file.

However, this method assumes each gamma event deposits energy in just one detector. In order to account for trajectories which, due to initial angle or scattering, deposit energy in multiple detectors, the coincidence method was amended as follows. Rather than tagging the channel by detector type, the channel number is preserved in the combined array (for reasons that will become clear in the next section), and the subroutine continues as before to scan the array until it reaches a beta event. Then, it opens up a maximum window of events (I used 10 events, which is quite a large window) to search in either direction from the chosen beta event. Within the loop, the time difference is calculated and the loop is exited if the difference exceeds the window size. Then, the channel number is checked to determine the type of the coincident event. If the channel is among the list of NaI detector channels, then the energy is summed to a total energy counter. If the total sum is greater than zero after the loop completes, the coincidence passes and the NaI energy is recorded as the sum of the energies from that event.

The resulting data are then compiled into a plaintext file containing the $[t, E_{NaI}, E_{sci}, runtype]$ for each event from all runs. This file is subsequently converted into a ROOT histogram list for further analysis.

5.1.3 Investigating Coincidence Data

In order to understand the results of the coincidence routine, there are several values that we can calculate. The first task of importance is to identify the proper coincidence window to use to maximize the signal to noise. Initial investigations as well as previous work on

---

already been used in a coincidence; otherwise, it will take the value of the preceding event. Should there be a coincidence which only agrees with a value already used in a previous coincidence, then the NaI energy for that event will be taken, but the event will be recorded as a double-counted event. Such events make up between 5 and 10 percent of all NaI energies recorded, based on an arbitrarily chosen subset of a few runs. Should this be an issue, the coincidence can be rewritten to trigger on the NaI events rather than on the beta events.

this question point to 100ns being an ideal timing window, with few issues arising from expanding up to 1μs. I will hold off on posting the details for now, as many changes have been made to the coincidence routine since the initial investigation, and this analysis should be presented more precisely than current data allow.

The next task is to investigate the incidence of two beta events being within the same coincidence window, which I will refer to as beta-beta coincidences henceforth. Since the rate of beta event triggers is significantly slower than 10MHz, we do not expect a sizeable rate of beta-beta coincidences in any given run. To verify this, an additional check was added to the coincidence routine to tally the incidences of channel 14 and 15 events during the inner loop. The resulting rates showed a 3% incidence rate before coincidences and 10% after coincidences (2.5% and 15% for long runs), likely arising from background events. Further analysis shows that every incident of beta-beta coincidence has the two coincident betas being triggered in different scintillators, occurring as a pair. The timing difference between such pairs of this is shown in Figure 5.2. The NaI energy (Figure 5.3) from individual runs supports the explanation that this effect arises from background events such as cosmic rays or high energy radioactive decays which pass through both scintillator paddles. We can expect that further efforts to reduce the noise arising from cosmic ray detection in the NaI detectors will also influence these rates.

The last check for the coincidence quality is to look at the details of the NaI detector triggers. Specifically, we can tally the multiplicity during the coincidence routine and ensure that most events do not trigger multiple NaI detectors. The initial expectation is that a real event will hit one or two detectors, while cosmic ray events will deposit energy in more detectors; this would allow us to add an additional cut to improve the signal. Ideally, there will be few events with high multiplicity. What we see, however, is that there are a relatively large number of events that trigger more than two NaI channels within the same coincidence window (See Figure 5.4). Oddly, there seems to be a peak at multiplicity
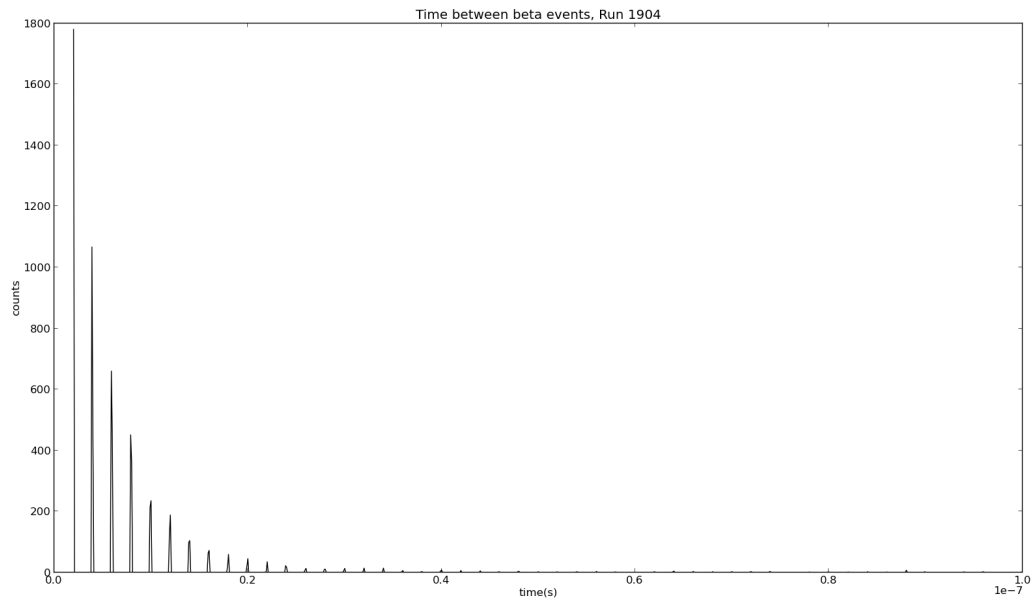
Figure 5.2: Timing difference between adjacent β-β events.
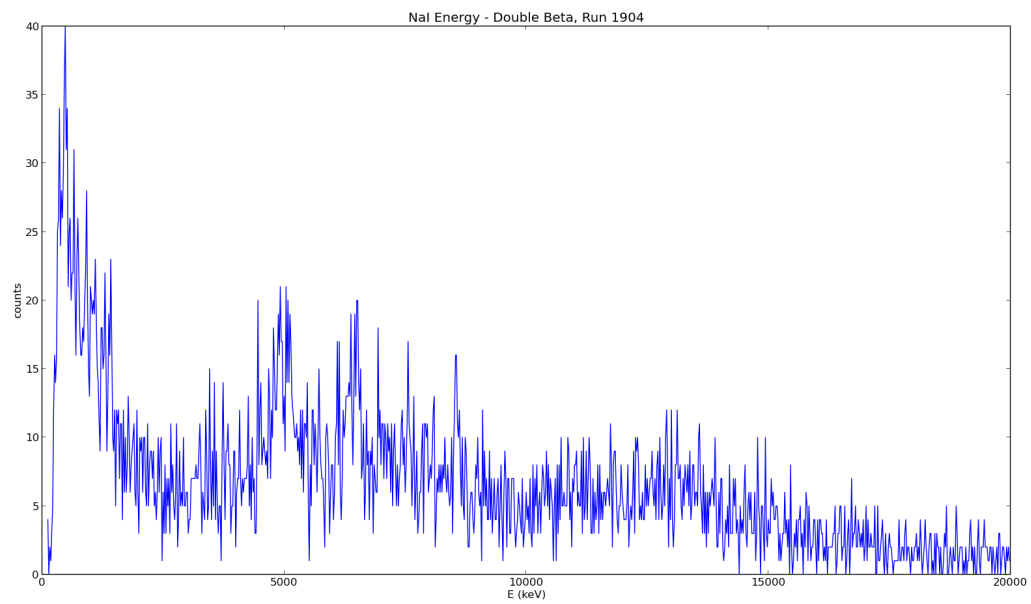
Figure 5.3: NaI energies associated with β-β coincidences.
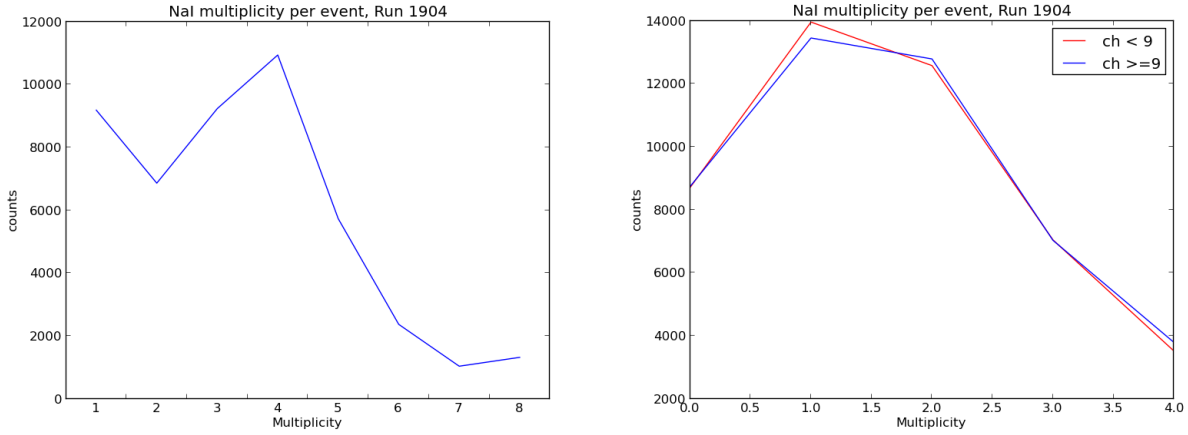
Figure 5.4: Left: Multiplicity of NaI channels during coincidence for Run 1904. Right: Same run, but with multiplicities split between halves.

4; this vanishes when the halves are divided which suggests that there are a large number of events which have a mostly horizontal incidence on the detector stack. This could also explain the large 2ns beta-beta coincidence rate discussed above. Implementing a cut which prohibits events triggering both halves of the NaI spectrum is therefore the next logical step, with a more sophisticated adjacency check to only allow for events in adjacent NaI detectors to be counted for coincidences being the sensible conclusion. Implementing this result indeed cuts the incidence of higher multiplicities by a large margin, and results in the spectrum seen in Figure 5.11.

5.1.4   Lifetime and Background calculation

Once the data for each run have been formatted and the coincidences have been applied, they are loaded into a script for finding the lifetime. The background is computed either from the dedicated background run or from the storage period of the long run and subtracted from the summed coincident data after cuts are applied. The signal count rate is input into Equation 2.1 to determine the lifetime with error for that run. Assuming that the background measurements are representative of the background during the counting

time (which will be demonstrated later), this should provide an accurate measurement of the lifetime; the lifetime values for each run are shown in Figure 5.5. Averaging these values gives a storage lifetime of $\tau = 875.92(67)s$.
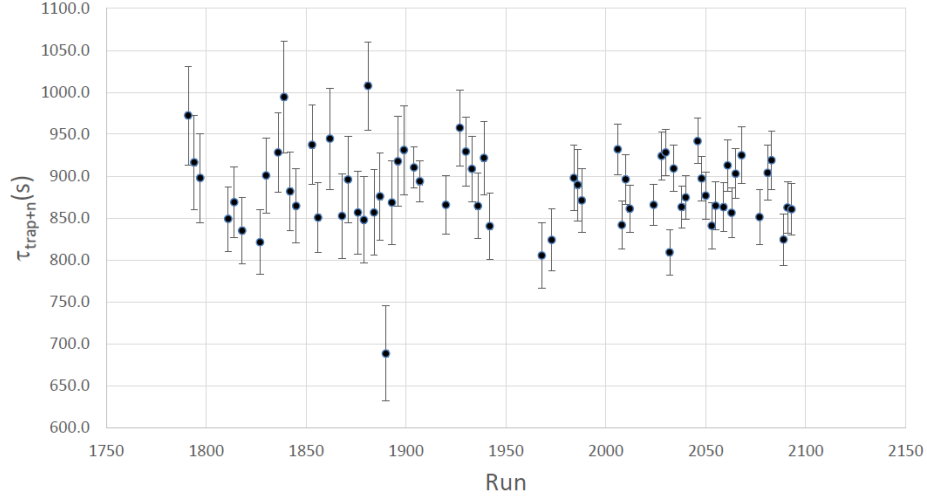
Figure 5.5: Lifetime values for all usable 2015 runs.

In order to obtain a reliable value for the lifetime, it is necessary to ensure that we are using an accurate method of background subtraction. For roughly half of the runs, a dedicated background run accompanied the short and long measurement runs (the set of these runs is referred to as a triplet), allowing direct subtraction from the normalized counts at each timing bin. For the other half, the background rate is inferred from the signal data rather than using a dedicated run. There are three particular methods of background subtraction that were analyzed in the non-triplet run pairs. The first is the independent doublets method (ID), in which the data is fit to an exponential with decay constant τ_V to determine the signal. For this fit, the background is assumed to have the sole time dependent component arising from Iodine decays and as such is a constant plus exponential function. This method assumes uncorrelated backgrounds and is less reliable in the calculation of short run background level. The second method sums the traces of the timing spectra from all runs in the same configuration, and is fittingly referred to as the

trace sums method (TS). Since this method combines multiple independent runs which often occur over a period of several days, temporal variations in the background are assumed to either be negligible or to have fluctuations which average out in the sum. The other noteworthy method is direct subtraction of background data obtained from the storage period of the long storage runs. The run plan used for the experiment results in each short run being immediately preceded and immediately followed by a long run. Hence, a background value can be determined by taking the average of these surrounding runs, which we call the sandwich method (SW). This allows us to correct the short term linear drift in the constant background over several hours. The results for the lifetime calculations performed using each of these methods can be seen in Figure 5.6.

In addition to the different background subtraction methods, there are several possibilities for cuts on the measured gamma energy spectrum. While an upper bound at around 1550 keV is apparent as a means of cutting cosmic events from the data while preserving the neutron signal, the lower bound has several possible values. A tight bound around the 1434 keV energy peak ($E_{gamma}^{min} \approx 1300 keV$) should yield the highest signal-to-noise ratio by removing lower energy background, but the loss in statistics from cutting out the compton edge may offset the precision gained over a looser cut. When considering the lower energy bound, an $E_{gamma}^{min} = 10 keV$ would leave the near entirety of the signal for the highest statistics at the cost of signal-to-noise ratio. Finally, the structure of the spectrum shows features at around 400keV and 800 keV, which can be removed by $E_{gamma}^{min} \approx 600 keV$ and $E_{gamma}^{min} \approx 1000 keV$. The lifetime value computed for each of these energy regions can be seen in Figures 5.6 and 5.7.

As Figure 5.7 shows, the different methods of background subtraction are generally in agreement when other parameters are kept fixed, suggesting that future analysis can equivalently use any of these methods. The energy window variation shows a slight upward

Method	beta singles	coincidence: 10~1550	coincidence: 600~1550	coincidence: 1000~1550	coincidence: 1300~1550	coincidence: 1350~1500
ID	876.75 ± 5.70	871.14 ± 3.59	873.65 ± 3.38	876.75 ± 3.22	879.58 ± 3.19	876.91 ± 3.09
TS	885.91 ± 5.98	876.68 ± 3.74	879.63 ± 3.55	884.89 ± 3.28	886.98 ± 3.25	884.15 ± 3.11
SW-err	879.94 ± 5.78 (881.14 ± 5.83)	872.53 ± 3.64 (873.56 ± 3.66)	874.86 ± 3.39 (874.99 ± 3.41)	877.20 ± 3.19 (877.45 ± 3.20)	880.00 ± 3.22 (880.48 ± 3.23)	878.23 ± 3.14 (878.77 ± 3.15)
SW-std	886.42 ± 6.15 (887.40 ± 6.62)	874.12 ± 4.58 (872.27 ± 4.44)	873.39 ± 4.50 (873.58 ± 4.37)	873.90 ± 3.81 (874.49 ± 3.99)	880.65 ± 3.93 (880.82 ± 3.95)	879.20 ± 4.10 (879.52 ± 4.09)

Figure 5.6: Aggregated results of lifetime analysis study for various background subtraction methods and coincidence windows. Parenthetical values use an additional weighting factor on the sandwich measurements for time proximity.

trend as the window tightens, but the lifetime values for each agree within statistics. In order to investigate whether this apparent trend results from statistical variance or from physical significance to the lower energy features, it is worth performing more thorough analysis of the gamma energies, as we will do in the following section. In addition to the quoted lifetime values from this analysis, we also have measured the systematic effects on the lifetime value through experimentation, which are reported in Figure 5.8 as 1.2×10^{-3}.

5.2 NaI Spectrum

5.2.1 Determining the spectrum

We seek to understand the overall NaI spectrum for the sake of extracting the sources of background from the signal. The data were formatted as above with a coincidence window of $\Delta t = 1\mu s$ and a timing offset $\delta t = 0.1\mu s$. While the NaI energies could be simply added up among the good runs from the 2015 data acquisition, we would like to adjust for any long term gain drifts in the detectors. As such, we would like to track the location of the known 1434.06 keV gamma peak from the $^{52}\text{V} \rightarrow \,^{52}\text{Cr*} \rightarrow \,^{52}\text{Cr} + \gamma$ decay. This calculation is done by fitting the peak region $[1300keV, 1600keV]$ to a gaussian and recording the mean and standard deviation for each run. The result, as can be seen in Figure 5.9, is that there is a steady upward drift in the peak location across runs, possibly
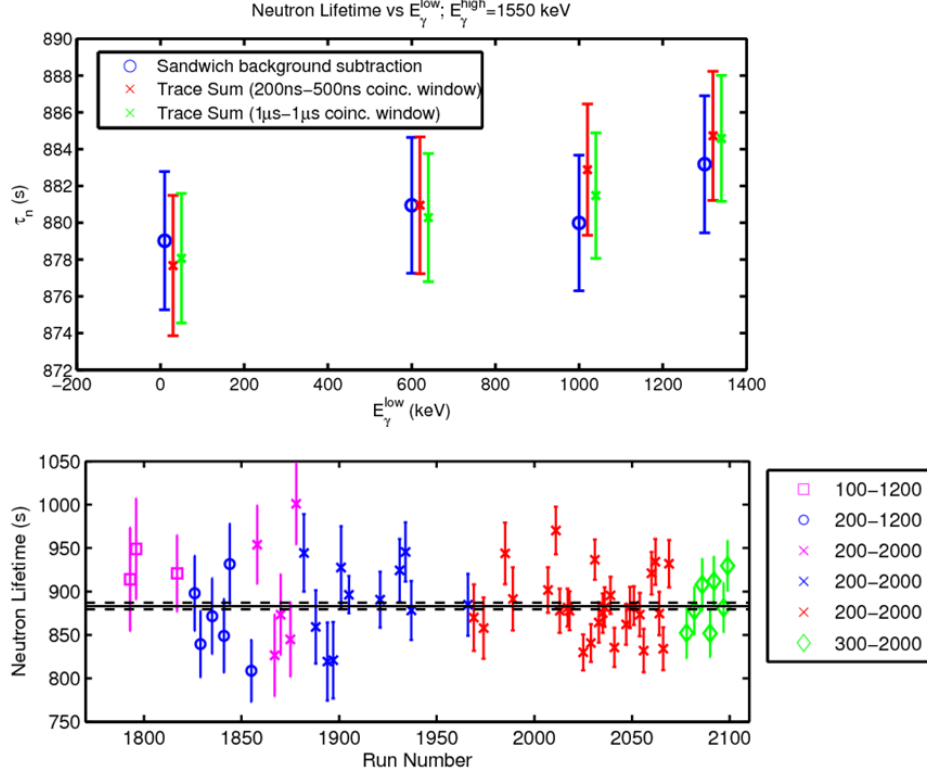
Figure 5.7: Top: Lifetime values obtained from representative runs from each background subtraction method at the various lower energy bounds. Bottom: Variance among the runs for Sandwich background subtraction method with $E_\gamma^{low} = 1350$

due to ambient temperature changes influencing the NaI gain. We can normalize each spectrum to these peaks to obtain consistent energies across runs.

From this, we can calibrate the energies of each run to match the vanadium peak to the theoretical value. By summing the results into a single plot for each type of run, we get a high statistics spectrum[3] for the short and long holding times, as in Figure 5.10.

There are several other features that we can investigate from this spectrum. In particular, there are three small peaks at the high end of the spectrum that may be useful in matching the spectra from other background sources. The same analysis from above yields high stability for these peaks despite the low statistics for each run. We will return to these in

_____

[3] 2.1 million total counts for short holding time runs and 1.4 million total counts for long holding time.

Effect	Upper Bound	Direction	Current Eval.	Method of Characterization
residual gas	$< 1 \times 10^{-4}$	+	meas	RGA/cross-section measurements
depolarization	$< 1 \times 10^{-4}$	+	calc	field map, *in situ* detection
material loss	$< 4 \times 10^{-4}$	+	calc	measure Cu tape loss-per-bounce
cleaning	$< 6 \times 10^{-4}$	+	sim	vary cleaning time/depth, active cleaner
cleaner reliability	$< 5 \times 10^{-4}$	$\pm$	sim	verify position reproducibility
microphonic heating	$< 1 \times 10^{-4}$	+	sim	accelerometer measurements
dead time/pileup	$< 1 \times 10^{-4}$	$\pm$	calc	pileup ID/artificial dead time
gain drifts	$< 2 \times 10^{-4}$	$\pm$	meas	spectral monitoring/gain monitoring
time-dep. background	$< 5 \times 10^{-4}$	$\pm$	meas	background data analysis
phase space evolution	$< 5 \times 10^{-4}$	$\pm$	sim	vanadium time studies, active detector
UCN monitoring	$< 3 \times 10^{-4}$	$\pm$	meas	measure monitor response/source stability
total	$< 1.2 \times 10^{-3}$	$\pm$		(uncorrelated sum)

Figure 5.8: Error budget for the 2015 lifetime data

the next subsection.

5.2.2 Comparison to Simulation

We can look at the NaI spectrum in Figure 5.10 and try to visually identify the source of its features from the most likely sources of background. Noteworthy peaks occur at several overlapping locations at low energies (E<600keV), the Compton edge at around 1.2 MeV, at the expected gamma peak at 1.4 MeV, and at the small triple peaks near 5 MeV. We can compare with the features noted in the simulation (Figure 5.13) and notice that very little can be seen from the ^{28}Al spectrum (though there is a chance that the 1.7 MeV peak is unresolvable from the vanadium peak) or the ^{208}Pb spectrum with the current experimental results, whereas the ^{128}I spectrum lacks any sharp peaks to investigate. Most notable is the lack of 5 MeV peaks; upon reinvestigation of earlier analysis, it is most likely that these "peaks" are actually artefacts arising from pileup in each NaI channel (see Figure 5.12), which occurs at a slightly different place in each detector resulting in the apparent multiple peaks. This would justify the near perfect consistency of the peak locations between runs. With the spectra generated from Geant4 simulation that we have in Figure 5.13, we can fit the experimental data as follows. Let us define the ^{52}V spectrum as $V(E)$, the ^{128}I

70
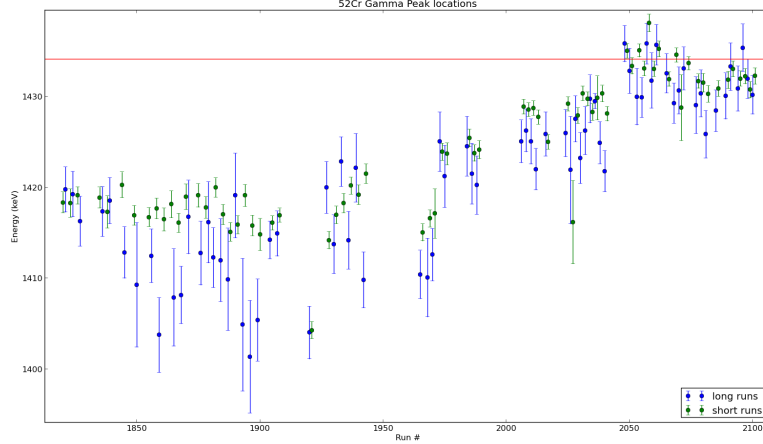
Figure 5.9: Stability of the 1434.06 keV peak from the NaI spectrum. The red line represents the theoretical peak energy. Some gain drift is visible through the run cycle.

spectrum as $I(E)$, the ^{28}Al spectrum as $A(E)$, and the data histogram as a probability function in energy and time as $N(E, t)$. Then, should exist parameters a_i such that:

$$N(E, t) = a_V V(E) e^{-\frac{t}{\tau_V}} + a_I I(E) e^{-\frac{t}{\tau_I}} + a_A A(E) e^{-\frac{t}{\tau_{Al}}} + B(E) \qquad (5.2)$$

where $\Sigma a_i = 1$, assuming proper normalization. Due to the names of the prominent elements, this will henceforth referred to as the VIAL function. In the above equation, we have allowed for a background $B(E)$ to exist which does not vary in time. Using the ROOT TH1::Fit() command, we can fix the time at either $t = 0$ for short runs or $t = T_{storage}$ for long runs. As the constant background is unknown, we shall ignore it for the current set of fits. By doing this, we obtain the fits present in Figure 5.14. Notice that neither fit is paticularly good, owing to the qualititative differences noted previously. At this point, it is worth returning to the discussion of unknown constant backgrounds. Notice that the long run, which should be dominated by the ^{128}I spectrum, is monotonically decreasing at high energies contrary to the expectation. Supposing that a

71
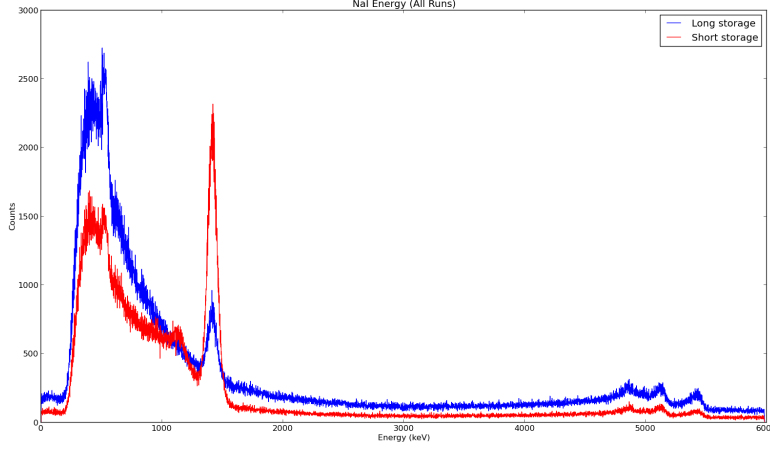
Figure 5.10: Gamma spectrum from all 2015 lifetime runs. Coincidence window is set to $1\mu s$.

background exists which can counteract this, we allow $B(E)$ to be nonzero. Since the form is unknown, we can use the time idependence of B to observe that the difference between the long and short spectra is:

$$
\begin{aligned}
N(E, t_{short}) - N(E, t_{long}) =& a_V V(E) e^{-\frac{t_{short}}{\tau_n}} + a_I I(E) e^{-\frac{t_{short}}{\tau_I}} + a_A A(E) e^{-\frac{t_{short}}{\tau_{Al}}} + B(E) + \\
& -a_V V(E) e^{-\frac{t_{long}}{\tau_n}} + a_I I(E) e^{-\frac{t_{long}}{\tau_I}} + a_A A(E) e^{-\frac{t_{long}}{\tau_{Al}}} + B(E) \\
=& b_V V(E) + b_I I(E) + b_A A(E)
\end{aligned}
\tag{5.3}
$$

where (assuming $\tau_i = \tau_n$ for the vanadium term)

$$
b_i = a_i \left(e^{-\frac{t_{short}}{\tau_i}} - e^{-\frac{t_{short}}{\tau_i}} \right)^{-1}
\tag{5.4}
$$

From this we can redo the fit on the difference of the two histograms, which yields the result in Figure 5.15. Notice that the fit is still fairly bad, but that the lack of a compton edge in the V(E) spectrum is a major culprit for this fitting issue. Furthermore we can investigate

72
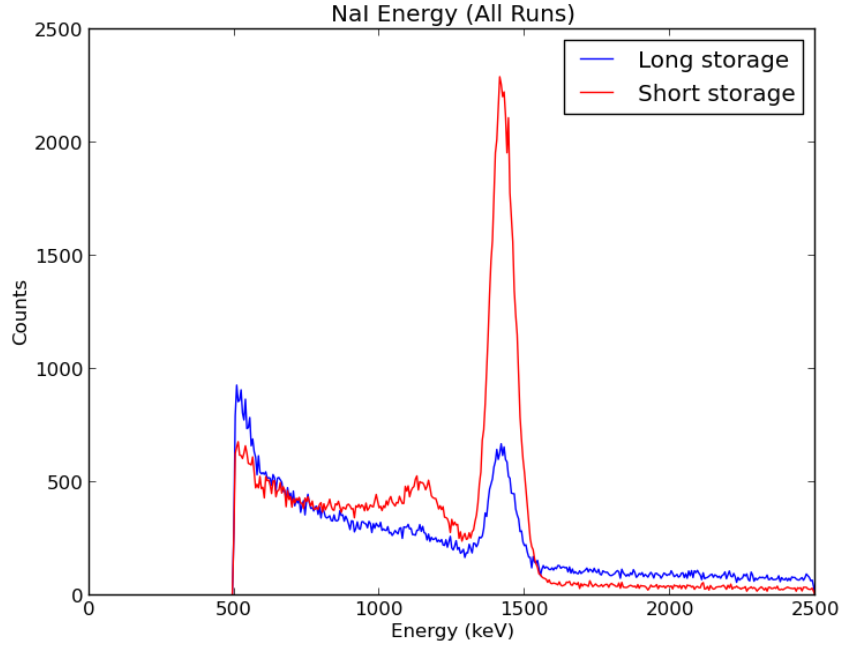
Figure 5.11: Gamma spectrum from all 2015 lifetime runs, subject to additional criteria: Coincidence window is set to 100ns, Energy is restricted between 0.5 and 2.5 MeV, the events during the filling time are ignored, and an anticoincidence is performed between the two NaI stacks.

the Compton edge for additional information on the fit; in particular, we find that the width of the main peak in $N(E)$ is broader than the peak in $V(E)$ which may indicate a calibration error which we can verify using information on the Compton edge. Finally, since the suspected issues with this fitting method are due to the $V(E)$ spectrum, we can try looking at background data to determine if we can fit the other constituent spectra. These topics will be discussed in more detail in the remaining subsections of Section 5.2.

5.2.3 Compton edge analysis

Based on the results obtained earlier, we have reason to believe that the compton edge will be an important component of the analysis. We first should figure out the theoretical
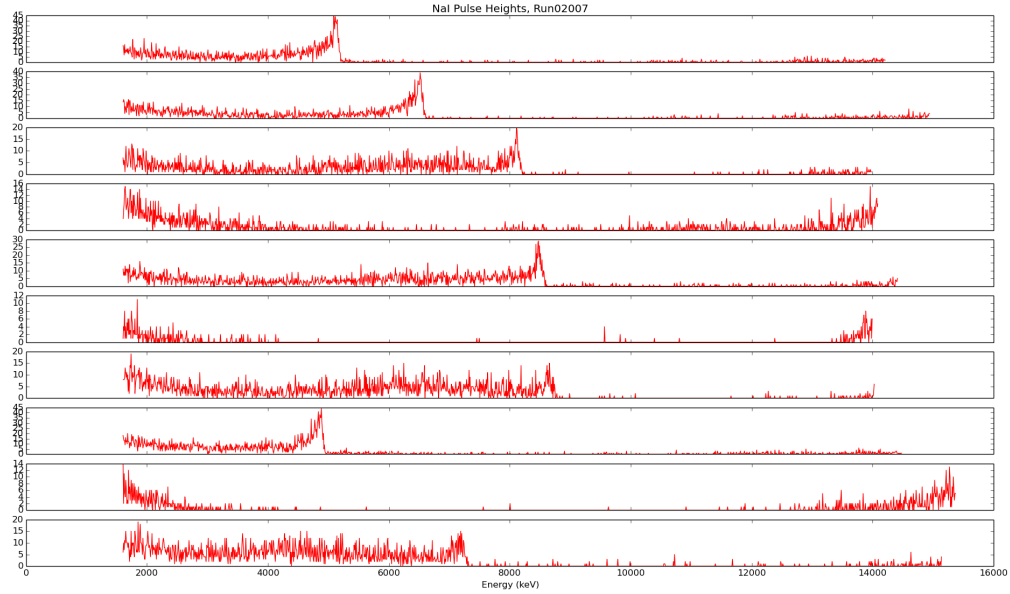
Figure 5.12: Uncalibrated singles spectrum for high energy events split between each NaI channel. Note the pileup at the high energies.
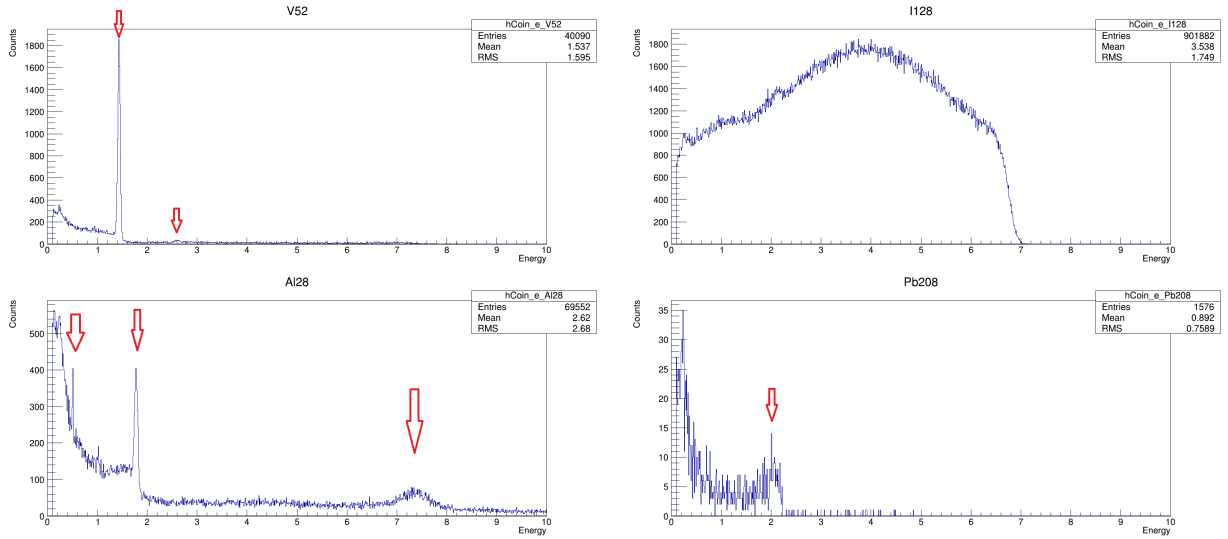
Figure 5.13: Spectra of likely decay sources in background, simulated with the full detector geometry using Geant4. From top left to lower right: ^{52}V, ^{128}I, ^{28}Al, ^{208}Pb. Energies in MeV. Notable peaks have been indicated where possible.

74
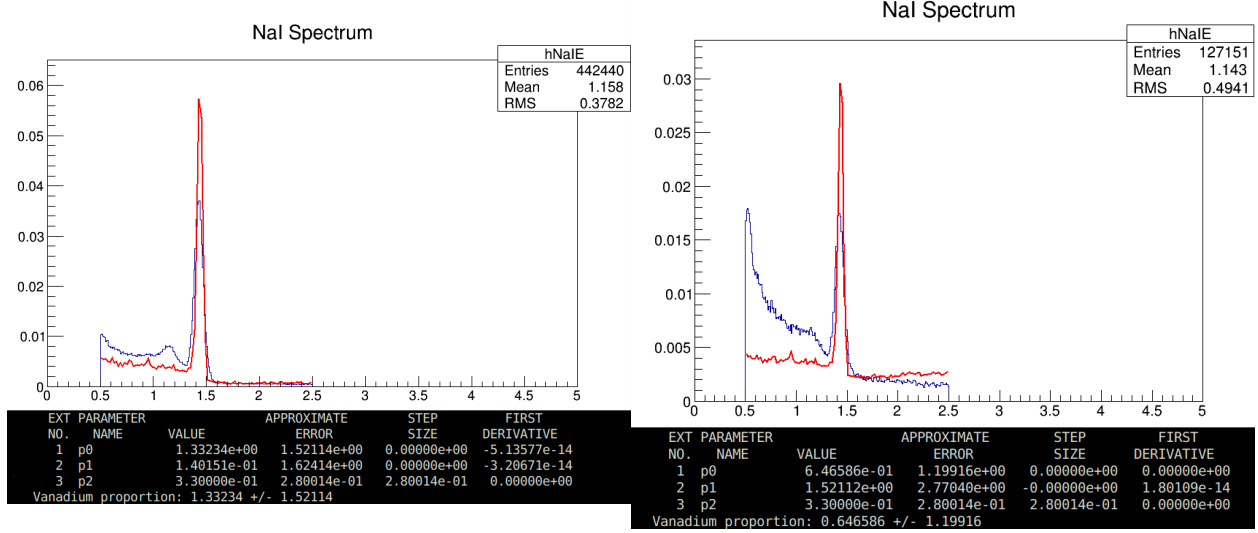
Figure 5.14: Fit to constituent spectra of all short runs (Left) and all long runs (Right).

energy value for the compton edge. To do so, we observe that the energy of the outgoing photon in a Compton scatter is given by:

$$\frac{1}{E_f} = \frac{1}{E_i} + \frac{1 - \cos(\theta)}{m_e c^2} \tag{5.5}$$

We are particularly interested in the minimum outgoing energy; that is, the maximum deposited energy $E_f - E_i$, which occurs at $\theta = \pi$. This suggests that the value of the energy at the compton edge can be given by:

$$E_c = \left(1 - \frac{m_e}{m_e + 2E_{peak}}\right) E_{peak} \tag{5.6}$$

Plugging in $E_{peak} = 1434.06$ keV and $m_e = 511$ keV$/c^2$, we expect a Compton peak to occur at $E_c = 1217.7$ keV. While the peak finding routine in the analysis script has not been yet fully implemented, it can be observed that the peak of the Compton edge is at a lower energy, closer to 1150 keV. The larger space between peak and Compton edge

75
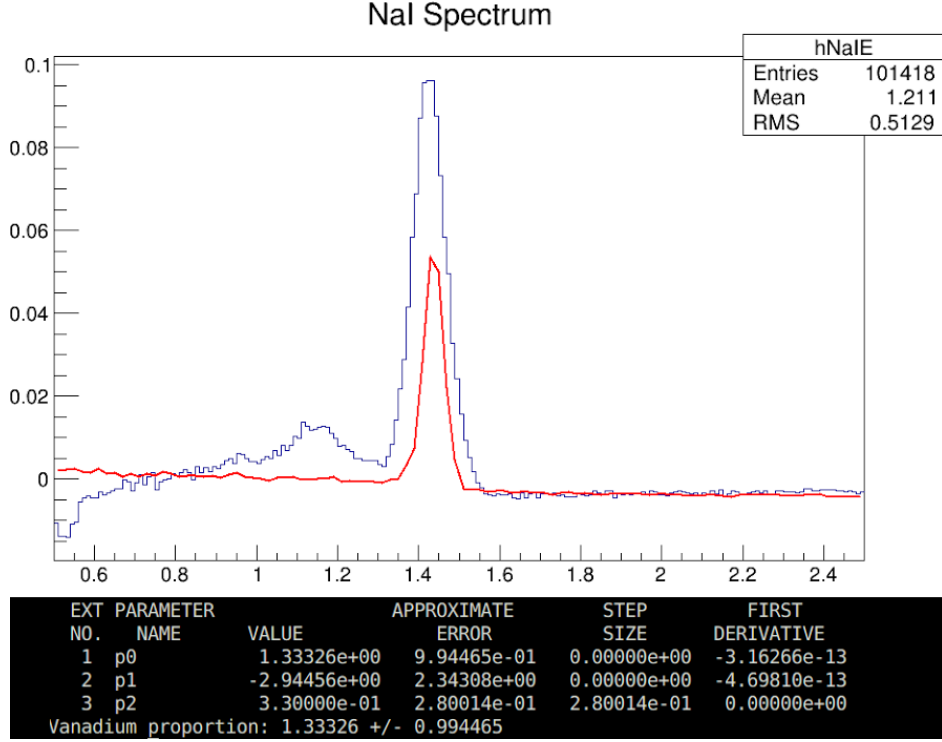
Figure 5.15: Fit to the constituent spectra of the difference between long and short run spectra.

together with the increased broadness of the peak compared to the theoretical expectation suggests that this is most likely a result of improper calibration. To fix this, we will need to implement a multiplier to match the two known values for the peak in the following way. Since we already calibrated for peak position, we can generate the histogram of event energies based on that calibration and use a peak finding routine to determine the location of E_c^{ex}, the energy of the compton peak in the experimental data. Then, each energy should be shifted according to $E' = \frac{1434.06 - 1217.7}{|1434.06 - E_c^{ex}|}(E - 1434.06) + 1434.06$, where energies are assumed to be in keV.

Using the TSpectrum::Search() class in ROOT, the peaks of the background-subtracted data could be found at $E_{peak} = 1.415$ MeV and $E_{Compton} = 1.145$ MeV as seen in figure 5.16. After adjusting the energies to match the Vanadium peak, the recalibration was
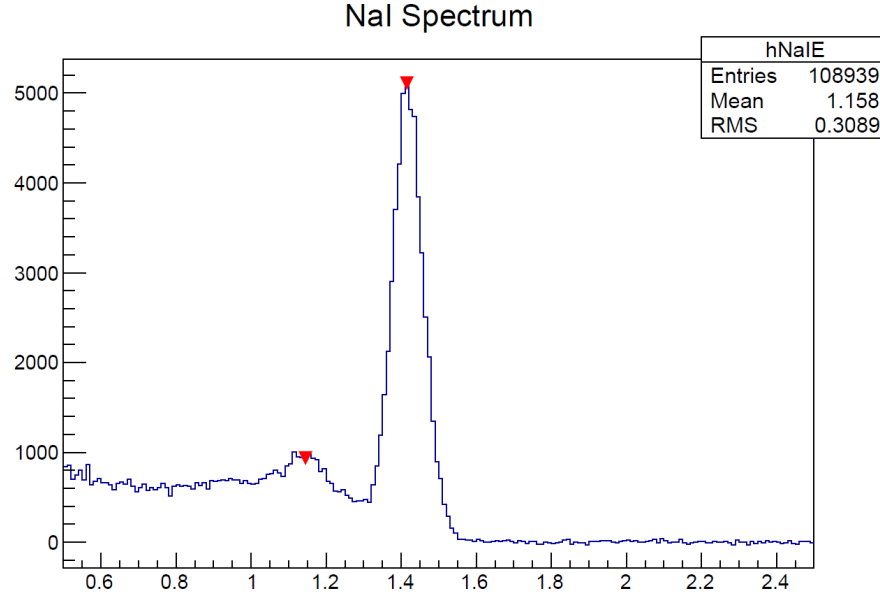
Figure 5.16: The short spectrum peak is found at 1.415 MeV, and the Compton edge at 1.145 MeV.

implemented as described above. The recalibrated data will be used in all subsequent plots.

5.2.4 Fit to background

A major issue with the previous VIAL fits is that there appears to be an extra component in the background from some other source. The leading candidate for this source is the lead bricks in the detector shielding, which we know to have been irradiated by high-energy beams in the past. To counter this, we can make use of the extra information that we have from the dedicated background runs from the 2014-2015 run cycle. The spectra from the background runs were prepared in a similar way to the signal data and are plotted in Figure 5.17. Notice that there is an exponential-like shape to the spectra which matches the extraneous component found in the previous plots.

There are two ways that we could possibly implement the background spectra into the
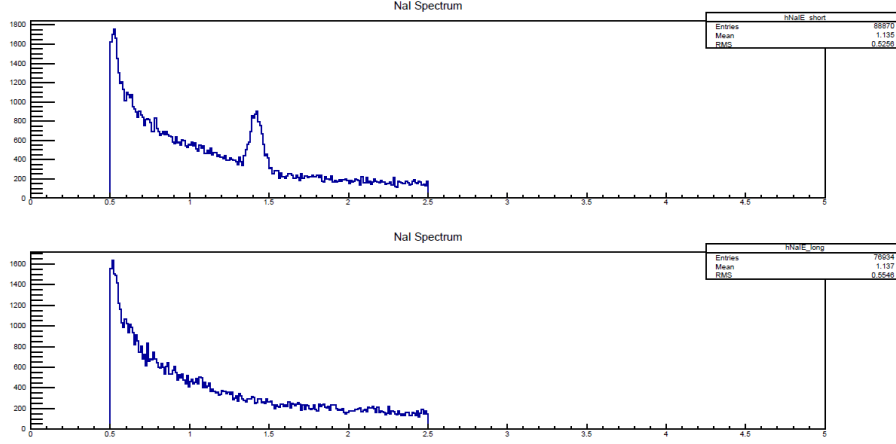
Figure 5.17: Spectra from long and short background runs.

VIAL fit. The first is to perform a direct subtraction from the respective triplet runs to determine an experimental signal plot, and fit that resultant plot to the VIAL function. The results are shown in Figure 5.18, but noticeably do not converge properly; the Al and I contributions are both negligible in this fit result, lending doubt to its accuracy. Aside from computing errors, the main reason why this fit may be so bad is likely to be that the lowered background causes the Compton edge to contribute more prominently to the data; the absence of a Compton edge in the V spectrum will cause the VIAL fit to fail.

The second and more robust way of implementing the background spectra is to create an extended VIAL (eVIAL) function with the uncategorized contribution from the background added as an additional (potentially time dependent) term $a_u u(x,t)$ in the parameterization. The tradeoff in this is that the fourth parameter will complexify the calculation and result in greatly increased computation times. However, we can begin with a reduced eVIAL function which forces $a_{Al}=0$ and performs the fit in the absence of the aluminum. This term will necessarily need to be added back in for the short run eVIAL fit, but the reduced fit should demonstrate approximate values to restrict the parameter space to speed up subsequent calculations. For this run, the resulting fit can be seen to fit extremely well as

78
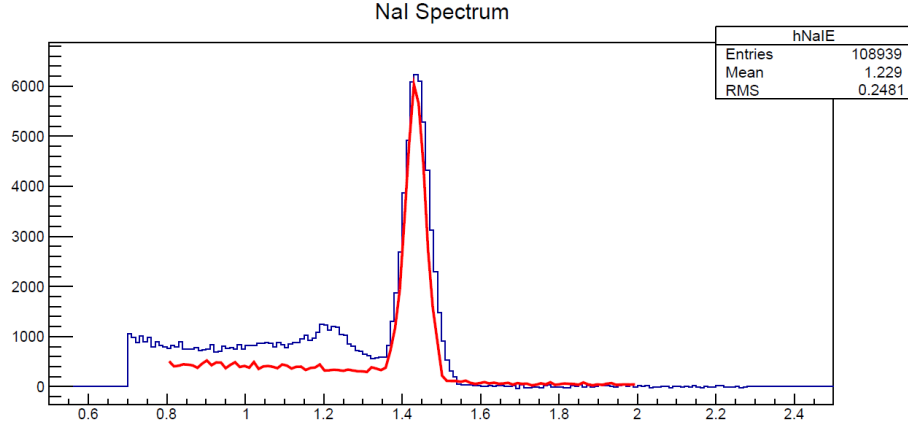
Figure 5.18: Fit to the background-subtracted spectrum from the short run data. Long run fit is comparably poor.
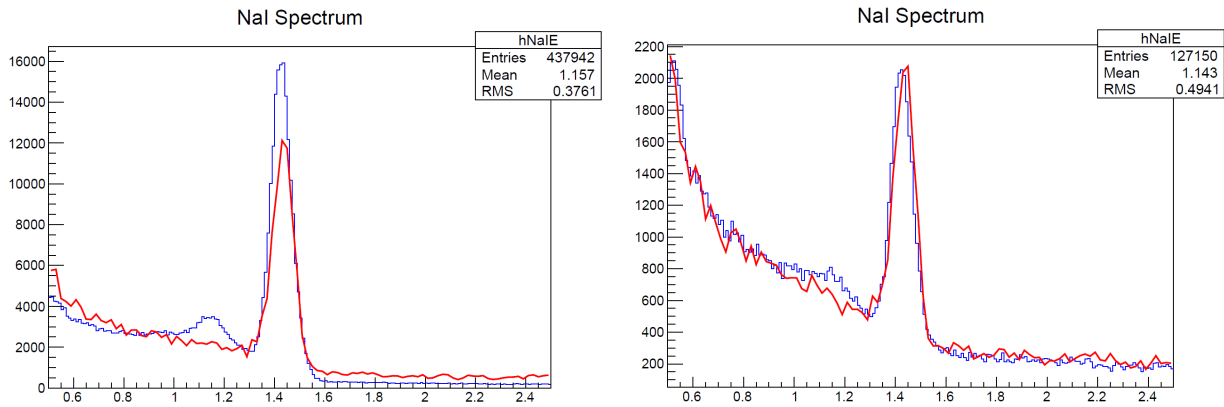
Figure 5.19: Extended VIAL fits it to constituent spectra of all short runs (Left) and all long runs (Right).

in Figure 5.19. Repeating this task with the short runs yields a slightly less good but still reasonable (given the lack of compton edge on the vanadium constituent) fit to the data. The values of the components of these fits can be found in Table 5.2. In particular, we see that the iodine component is extremely small, with an upper bound within error showing as 0.0175% of the total spectrum. This is likely to cause negligible deviation from the actual lifetime value, but this will be investigated in the later computation of the lifetime.

It is also worth noting that we can see the variation in the contribution from the

79

uncategorized backgrounds, which Figure 5.17 indicates should have little to no time variation outside of Vanadium peak contribution. As a means of testing this, two fits were prepared for the background functions. The first looked at fitting the short run background spectrum to an eVIAL function with the contribution from uncategorized background taken from the long run background spectrum. In doing this, we expect to see the components present from the V, I, and Al which are lacking in the final measurement. The resulting fit is displayed in Figure 5.20 and the data are recorded in Table 5.2. The results particularly show that the deviation from the long background is entirely Vanadium within error, with a maximum contribution of the difference capped to 0.38% Iodine and 8.6% Aluminum.[4] From this, we can conclude that the main source of time dependent background comes from the capture of neutrons during the fill, and the contribution from the background is roughly 25%.
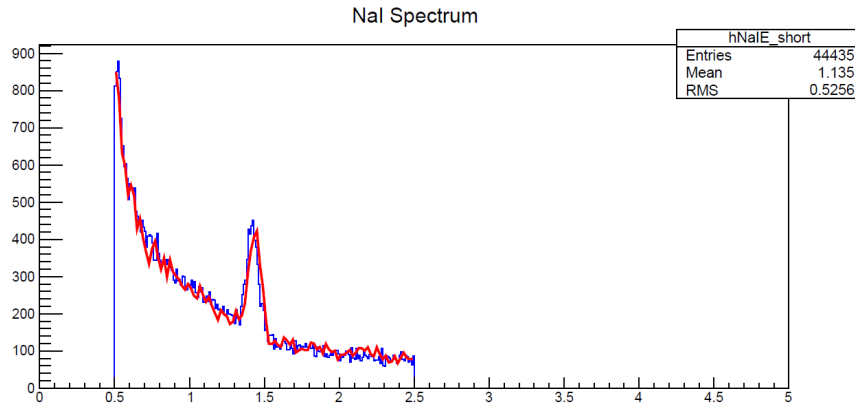
Figure 5.20: Extended VIAL fit to the long run data (corrected). Fit shown in red.

The second study that can be done is to perform a fit on the difference between the short and long backgrounds. Since the counting time is not varied, the long run backgrounds would demonstrate a reduction in signal exclusively from the time-dependent components

---

[4]These values are given relative to the contribution from sources aside from the miscellaneous background. The percentage values (not included explicitly in Table 5.2) for these contributions are 96.30±5.77 Vanadium, $3.5 \times 10^{-8} \pm 0.38$ Iodine, and 3.73 ± 4.86 Aluminum.

Spectrum	Vanadium	Iodine	Aluminum	Misc. BG
Long Run, Al=0	46.75 ± 0.45	$1\times10^{-18} \pm 0.018$	0	53.25 ± 0.34
Short Run	66.42 ± 0.23	$5\times10^{-12} \pm 0.00012$	0	$33.576 \pm .065$
Short BG	24.47 ± 0.73	$9\times10^{-9} \pm 0.097$	0.95 ± 1.23	74.58 ± 1.4
BG Diff.	100 ± 17.2	$1\times10^{-11} \pm 0.17$	$4\times10^{-12} \pm 0.28$	0

Table 5.2: Coefficients (a_i) of various fits. All values given as percentages

of the background in comparison to the short run backgrounds. We expect from comparing the spectra in Figure 5.17 that there should be little by way of time variation between the backgrounds. The actual fit that we get when fixing $a_U = 0$ is shown in Figure 5.21. This fit confirms the notion that the time dependence in the background is largely composed of Vanadium with other contributions constrained to less than a quarter of a percent. However, we can see that there is a discrepancy in the fit at the peak, which may well point to the suggestion that the uncategorized background contains a non-vanadium component at a potentially nontrivial level. It may be necessary to free the a_U component to investigate the relative size of the variation in non-vanadium background.
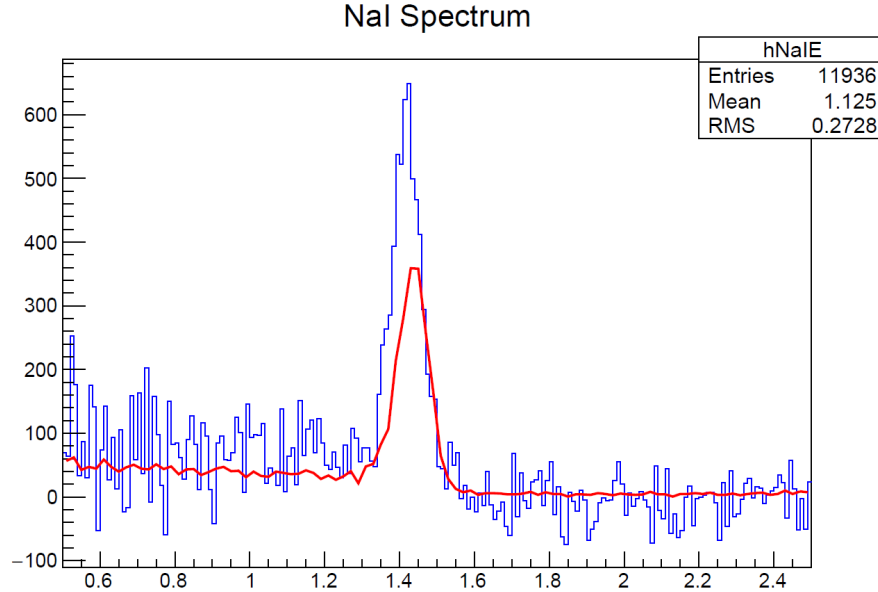
Figure 5.21: Extended VIAL fit to the difference between the short and long background spectra. Fit shown in red.

5.3 Lifetime calculation

5.3.1 Lifetime Extraction Script

We can compute the lifetime rather simply from knowing the number of neutrons in the trap at time t, $N_0(t)$ for two points in time t_1 and t_2 using:

$$\tau = \frac{t_2 - t_1}{\log\left(\frac{N_0(t_1)}{N_0(t_2)}\right)} \tag{5.7}$$

We can take $t_1 = 0$ without loss of generality, and take the change in time to be $t = t_2 - t_1 = t_2$. If we presume that each N_0 is derived from subtracting the background from a given measured signal, each of which has an uncertainty which goes as $\sqrt{n}$, then the uncertainty for the lifetime becomes:

$$\sigma\tau = \frac{\tau^2}{t}\sqrt{\frac{1 + e^{t/\tau_V}}{N_0(0)}} \tag{5.8}$$

We can then extract the lifetime from the data by specifying a counting period, say 1000s, and integrating over the counting time for each appropriate time. The energy cuts which are applied to the data are performed after scaling the energy peak to the theoretical value. This integral can be used to reconstruct the N_0 for that counting time. In principle, the data can be sent to the VIAL fit routine to extract the signal-to-background ratios and adjust the measured counts accordingly; otherwise, these ratios may be manually entered as inputs. With such a counting method, the background subtraction should be carried out bin-by-bin of the time histogram in order to account for the change in signal of the decaying components appropriately. A correction term is then applied to correct for any changes in the storage time t for the long storage runs. Finally, the above equations are used to determine the lifetime with statistical uncertainty. The result from the VIAL

fitting suggests that the value arrived at here does not need any additional correction due to time dependent backgrounds, as the measured background for each run is sufficient to determine its influence on the measured signal. As such, the results presented in Figure 5.6 can be taken as an accurate calculation of the background subtraction.

5.3.2 Deadtime correction

One area which may require additional correction to the lifetime value is the existence of sporadic dead time in the code due to pileup in the signal. This is apparent in the data as the analysis software is set to record a zero energy event in this scenario. One way to gain insight into this effect and determine the necessary correction is to investigate the impact of a software deadtime. In the ROOT conversion script, a deadtime is implemented by performing a check between consecutive events for $t_{new} - t_{old} > T_{dead}$ prior to filling the histograms. The lifetime is then calculated according to this incomplete set of data and assuming the background values determined from the preceding scan. When analyzing the impact of the deadtime, there is a feature at low deadtime (t<40 ns) as seen in Figure 5.22. There is no noticeable functional form to the lifetime values as the deadtime approaches zero at this scale, with the most likely explanation being the recording of random data in the event of a buffer overflow, as the DAQ system is known to do. Should a non-negligible fraction of this 'junk" data persist through the coincidence routine, there will be such random offsets as shown in the deadtime scan. To remedy this, we set a minimum deadtime of 40 ns and select a series of deadtime values across the region where the lifetime is linear. The lifetime at each selected deadtime value is calculated and a linear fit is made with the y-intercept being taken as the real lifetime value for that measurement. This process resulted in a shift in lifetime value of 2.1s.
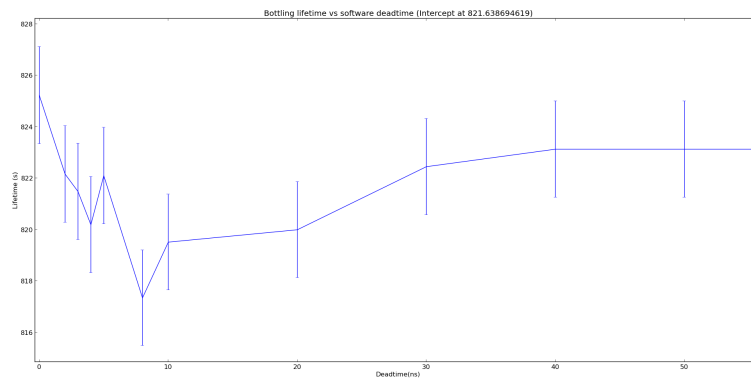
Figure 5.22: Lifetime value from one triplet as a function of software deadtime. Above 40 ns, the lifetime result is linear.

CHAPTER 6

CONCLUSION

The UCNτ experiment presents new innovations in the field of UCN bottling measurements. The novel open topped design allows for in situ detection to eliminate systematic errors associated with draining the trap. One feature of maximizing the precision of measurement for this experiment is an effective and well understood transport system for the UCN. Analysis of the guide parameters using the Geant4 Monte Carlo simulation toolkit allowed us to assess the quality of the guides and the efficiency of the guide system as it was laid out in the first run of the experiment. This simulation further enabled the testing of new cross assembly designs which showed an order of magnitude improvement of the trap population resulting from reduced depolarization and improved phase space mixing. Furthermore, the development of new detectors utilizing boron capture allowed for extremely low background UCN detectors with a high degree of flexibility. The data collected from the first lifetime measurement run cycle at the start of 2015 provided an opportunity to explore the measurement technique and possibly produce a competitive neutron lifetime value.

Analysis of the 2015 data allowed us to investigate the various approaches to extracting the UCN lifetime. UCN polarization in the trap was demonstrated to be conserved sufficiently for storage. The background measurement was not sufficiently understood during the data

taking. While simulation provided several candidates for the background sources, the background spectrum showed the sole time dependent component arising from erroneously captured neutrons on the vanadium foil. Consequently, the use of direct background subtraction using dedicated background measurements sufficed to produce accurate counting. Measurements of the drift in energy normalization per run as a result of ambient conditions on the detectors and deadtime arising from signal pileup in the data acquisition system yielded corrections to the lifetime value. These corrections allowed us to improve upon the initial vanadium lifetime measurement of $877.9 \pm 6.7_{stat} \pm 1.1_{syst}$ seconds. Limitations on the cleaning reliability and phase space evolution limit the accuracy of this measurement as a neutron lifetime.

Following the 2015 measurement, we have implemented many changes to the UCNτ apparatus for the sake of improving the precision during future measurements. Among the most significant changes was the replacement of the vanadium detector system. The delayed measurement of the vanadium decays, which allowed for a long period of potentially time dependent background, residual activation between runs, long counting times, and compounding error as a result of fitting algorithms resulted in fundamental limitations to the accuracy of the vanadium measurement. The new detector system instead utilizes a modified ZnS detector in which a flat light guide of comparable dimension to the vanadium foil is coated on either side with boron-coated ZnS films and the light that is collected from the neutron signal is routed through wavelength shifting fibers to two PMTs in hardware sum. In addition to the reduced background rate, the immediacy of the real time detection signal allows for a much more sophisticated measurement of in trap systematics such as cleaning height and UCN height density.

Another major change was an improvement of the spectral cleaning apparatus. The roles of the moving cleaner and the stationary large cleaner were combined into a single movable

large cleaner which had a much higher reliability in cleaning due to the higher proportion of marginally trapped phase space covered by the cleaner. The improved cleaner in tandem with the real-time in-situ detection allowed for the measurement of the trap population at multiple heights in a single fill, yielding accurate measurements of the cleaning reliability and the effects of phase-space evolution of trapped UCN. The LANSCe facility also underwent renovations to the UCN source with the resulting UCN production rate much higher than in the previous runs. This in tandem with the greatly reduced run duration due to the upgraded detector resulted in a vast improvement of statistics per run time in the most recent measurement cycle. Finally, a blinding factor was introduced to the data collection to mitigate any effect of bias on run vetting. This blinding was possible due to the consistency and trustworthiness of the experimental setup which was developed during the 2015 measurement run. The unblinding and analysis of this new data set is underway, producing a neutron lifetime value with a total uncertainty below 1 s.

BIBLIOGRAPHY

[1]   A. Pichlmaier et al. "Neutron lifetime measurement with the UCN trap-in-trap MAMBO II". In: *Physics Letters B* 963 (2010).

[2]   A.P. Serebrov et al. "Neutron lifetime measurements using gravitationally trapped ultracold neutrons". In: *Physics Letters B* 605 (2005).

[3]   A.T. Yue et al. "Improved Determination of the Neutron Lifetime". In: *Phys. Rev. Lett.* 111 (2-13).

[4]   C.M. Lavelle et al. "Ultracold-neutron production in a pulsed-neutron beam line". In: *Phys. Rev. C* 82 (2010).

[5]   D.J. Salvat et al. "Storage of ulstracold neutrons in the magneto-gravitational trap of the UCNτ experiment". In: *Physical Review C* 89 (2014).

[6]   Gabriele Cosmo et al. *Geant4UCN*. 2001. URL: https://github.com/rayrios/Geant4UCN.

[7]   P.L. Walstrom et al. "A magneto-gravitational trap for the absolute measurement of the ultra-cold neutron lifetime". In: *Nucl. Inst. and Meth. in Phys. Res. A* 599 (2009).

[8]   R.Chytracek et al. *Geometry Description Markup Language for Physics Simulation and Analysis Applications*. 2008. URL: https://gdml.web.cern.ch/GDML/.

[9]   S Agostinelli et al. "Geant4 - a simulation toolkit". In: *Nuclear Instruments and Methods in Physics Research A* (2003).

[10] W. Mampe et al. "Neutron Lifetime Measured with Stored Ultracold Neutrons". In: *Phys. Rev. Lett.* 63.6 (1989).

[11] Z. Wang et al. "A multilayer surface detector for ultracold neutrons". In: *Nucl. Inst. and Meth. in Phys. Res. A* 798 (2015).

[12] J. Chadwick and M. Goldhaber. "A 'Nuclear Photo-effect': Disintegration of the Diplon by g-Rays". In: *Nature (London)* 134.237 (1934).

[13] Yang Dong and Huo Junde. *Nuclear Data Sheets 128, 185.* 2015. URL: https://www.nndc.bnl.gov/chart/.

[14] R Golub, D Richardson, and S K Lamoreaux. *Ultra-Cold Neutrons.* New York, NY: Taylor and Francis Group, 1991.

[15] Glenn F. Knoll. *Radiation Detection and Measurement.* Hoboken, NJ: John Wiley and Sons, 2000.

[16] W.J. Marciano and A. Sirlin. "Improved Calculation of Electroweak Radiative Corrections and the Value of V_{ud}". In: *Phys. Rev. Lett.* 96 (2006).

[17] J. Beringeri et al. (Particle Data Group). *PR D86, 010001.* 2012. URL: http://pdg.lbl.gov.

[18] F.E. Wietfeldt and G.L. Greene. "Colloquium: The neutron lifetime". In: *Rev. Mod. Phys.* 83.4 (2011).

[19] James F. Ziegler. *The Stopping and Range of Ions in Matter.* 2008. URL: srim.org.

APPENDIX A

LIFETIME UNCERTAINTY - NONZERO BACKGROUND

Now suppose that there is some background $B(t)$ such that $B(t_i) \equiv B_i$. In this case, we must subtract the background to obtain the lifetime:

$$\tau = \frac{t_2 - t_1}{\log \frac{N_1 - B_1}{N_2 - B_2}} \tag{A.1}$$

We can define our signal terms as $S_i \equiv N_i - B_i$, with uncertainty $\sigma S_i = \sqrt{\sigma N_i^2 + \sigma B_i^2} = \sqrt{N_i + B_i}$. In this case, we have that:

$$\tau = \frac{t_2 - t_1}{\log \frac{S_1}{S_2}} \tag{A.2}$$

Since this take an identical form to Equation (1), we can immediately conclude that:

$$\sigma\tau^2 = \frac{1}{log\left(\frac{S_1}{S_2}\right)}\left[\sigma t^2 + \frac{t^2}{log\left(\frac{S_1}{S_2}\right)}\left(\frac{\sigma S_1^2}{S_1^2} + \frac{\sigma S_2^2}{S_2^2}\right)\right]$$

$$= \frac{\tau^2}{t^2}\left[\sigma t^2 + \tau^2\left(\frac{N_1 + B_1}{(N_1 - B_1)^2} + \frac{N_2 + B_2}{(N_2 - B_2)^2}\right)\right] \tag{A.3}$$

$$\Rightarrow \sigma\tau = \frac{\tau}{t}\sqrt{\sigma t^2 + \tau^2\left(\frac{N_1 + B_1}{(N_1 - B_1)^2} + \frac{1}{N_2 - B_2} + \frac{2B_2}{(N_2 - B_2)^2}\right)} \tag{A.4}$$

Again, we can use the fact that the signal should follow an exponential decay, $S_2 = S_1 e^{\frac{-t}{\tau}}$, to simplify this equation as:

$$\sigma\tau = \frac{\tau}{t}\sqrt{\sigma t^2 + \tau^2\left(\frac{N_1 + B_1}{(N_1 - B_1)^2} + \frac{e^{\frac{t}{\tau}}}{(N_1 - B_1)} + \frac{2B_2 e^{\frac{2t}{\tau}}}{(N_1 - B_1)^2}\right)}$$

$$\sigma\tau = \frac{\tau}{t}\sqrt{\sigma t^2 + \frac{\tau^2}{S_1^2}\left((N_1 + B_1) + S_1 e^{\frac{t}{\tau}} + 2B_2 e^{\frac{2t}{\tau}}\right)} \tag{A.5}$$

Let us define $D \equiv N_1 + B_1$ to simplify the expression. Suppose the background varies as $B(t) = B_1 + \widetilde{B}(t)$. We now can differentiate:

$$\frac{\partial \sigma\tau}{\partial t} = \frac{-\tau}{t^2}\sqrt{\sigma t^2 + \frac{\tau^2}{S_1^2}\left((N_1 + B_1) + S_1 e^{\frac{t}{\tau}} + 2B_2 e^{\frac{2t}{\tau}}\right)} +$$

$$+ \frac{\tau \frac{\tau^2}{S_1^2}\left(\frac{S_1}{\tau}e^{\frac{t}{\tau}} + \frac{4B_2}{\tau}e^{\frac{2t}{\tau}} + 2\frac{\partial\widetilde{B}}{\partial t}e^{\frac{2t}{\tau}}\right)}{2t\sqrt{\sigma t^2 + \frac{\tau^2}{S_1^2}\left((N_1 + B_1) + S_1 e^{\frac{t}{\tau}} + 2B_2 e^{\frac{2t}{\tau}}\right)}}$$

$$= \frac{\tau^3\left(-2\left(\left(\frac{S_1\sigma t}{\tau}\right)^2 + D + S_1 e^{\frac{t}{\tau}} + 2B_2 e^{\frac{2t}{\tau}}\right) + \frac{t}{\tau}\left(S_1 e^{\frac{t}{\tau}} + 4B_2\left(1 + \frac{\tau}{2B_2}\frac{\partial\widetilde{B}}{\partial t}\right)e^{\frac{2t}{\tau}}\right)\right)}{2t^2 S_1^2\sqrt{\sigma t^2 + \frac{\tau^2}{S_1^2}\left((N_1 + B_1) + S_1 e^{\frac{t}{\tau}} + 2B_2 e^{\frac{2t}{\tau}}\right)}} \tag{A.6}$$

As before, we can take $\frac{S_1 \sigma t}{\tau} \ll 1$. We also define $x \equiv \frac{t}{\tau}$ as before and $I \equiv 1 + \frac{\tau}{2B_2} \frac{\partial \widetilde{B}}{\partial t}$[1].

Setting the numerator equal to zero yields the minimum uncertainty:

$$0 = -2\left(D + S_1 e^x + 2B_2 e^{2x}\right) + x\left(S_1 e^x + 4B_2 I e^{2x}\right) \tag{A.7}$$

$$\Rightarrow 2B_2(2x - 2)e^{2x} + S_1(x - 2)e^x - 2D = 0 \tag{A.8}$$

$$\Rightarrow 2B_2(2x - 2)e^{2x-2} + S_1(x - 2)e^{x-2} - \frac{2D}{e^2} = 0 \tag{A.9}$$

This equation is unable to be solved using simple analytical methods, to the best of our knowledge. However, if we define the backgrounds and the t_1 measurements, it is straightforward to determine a numerical solution.[2]

A.1 No Background, Revisited

We verify that setting $B_1 = B_2 = 0$ yields $S_1 = D = N_1$, and hence

$$N_1(x - 2)e^{x-2} - \frac{2N_1}{e^2} = 0 \tag{A.10}$$

which is identical to Equation (16). Thus, we recover the background-less result of $t_2 = t_1 + 2 + W\left(\frac{2}{e^2}\right)$

---

[1]For the constant background case, $\frac{\partial \widetilde{B}}{\partial t} = 0$ and hence $I = 1$. This generalizes the result with minimal additional complexity. It is worth noting that we reduce to $I \approx 1$ whenever $\frac{\partial \widetilde{B}}{\partial t}\big|_{t_2 - t_1} \ll \frac{2B_2}{\tau} \approx 0.00227 B_2$, which is somewhat more general than the constant background case while yielding the same result.

[2]From an experimental standpoint, this is sufficient for a solution, since it is possible to obtain all the necessary information for the calculation prior to taking the second measurement, provided sufficiently steady background (as already assumed).

A.2 Example solution

Consider a constant background measurement with $B_1 = B_2 = 10$ and $(t_1, N_1) = (200s, 250)$. In this case, Equation (27) becomes:

$$20(2x - 2)e^{2x-2} + 240(x - 2)e^{x-2} - \frac{520}{e^2} = 0 \qquad (\text{A.11})$$

from which we calculate $x \approx 1.7193$. Hence, the uncertainty is minimized when $t_2 = 200 + 1.7193\tau \approx 1713s$.

A.3 Low Background

We attempt to seek a simplification of Equation (27) that will allow for an analytical solution in the case where B_2 is small (in some sense) compared to S_1. We rearrange terms such that

$$((x - 2)S_1 + (x - 1)4B_2 e^x) e^{x-2} = \frac{2D}{e^2} \qquad (\text{A.12})$$

$$\left((x - 1)S_1 \left(1 + \frac{4B_2}{S_1} e^x \right) - S_1 \right) e^{x-2} = \frac{2D}{e^2} \qquad (\text{A.13})$$

Now, we consider the $\left(1 + \frac{4B_2}{S_1} e^x \right)$ factor.[3] If the background is sufficiently small such that, for the eventual value of x, we have $B_2 \ll \frac{S_1}{4} e^{-x}$, then Equation (31) becomes:

$$(x - 2)S_1 e^{x-2} = \frac{2D}{e^2} \qquad (\text{A.14})$$

---

[3]We may run into trouble if we carelessly separate this expression from the rest of the equation; to avoid this, it is necessary that we only look for solutions such that $(x - 2) \not\ll (x - 1)$.

which has the solution

$$x = 2 + W\left(\frac{2(N_1 + B_1)}{e^2(N_1 - B_1)}\right) \tag{A.15}$$

If we also have $B_1 \ll N_1$ we can further conclude:

$$= 2 + W\left(\frac{2}{e^2}\left(\frac{N_1}{N_1 - B_1} + \frac{B_1}{S_1}\right)\right)$$

$$= 2 + W\left(\frac{2}{e^2}\left[\frac{1}{1 - \frac{B_1}{N_1}} + \mathcal{O}\left(\frac{B_1}{S_1}\right)\right]\right)$$

$$= 2 + W\left(\frac{2}{e^2}\left[1 + \mathcal{O}\left(\frac{B_1}{S_1}\right)\right]\right)$$

$$\approx 2 + W\left(\frac{2}{e^2}\right) \tag{A.16}$$

$$\tag{A.17}$$

Which results in Equation (17), the background-less case. We combine Equation (33) with the previously determined background limit to conclude that we are in an effectively background-less situation (with regards to lifetime uncertainty) whenever

$$B_2 \ll \frac{S_1}{4}e^{-2.2177} \approx 0.0272 S_1 \tag{A.18}$$

APPENDIX B

SURFACE MULTILAYER INTERACTIONS OF UCN

When investigating UCN transport, we concern ourselves with the material boundary
interactions of the neutrons with the guide surfaces and other elements of the experimental
apparatus. As a UCN has the potential to interact multiple times with any given surface, it
is important that we have a good understanding of the effective Fermi potential and loss
factor for each surface. One issue that arises when considering these parameters is that
many materials tend to spontaneously form a surface layer by interacting with air, most
commonly one or more oxide layers. The existence of such oxide layers casues an
energy-dependent perturbation of the expected material interaction properties. This applies
equivalently to any instance of consecutive thin layers upon a substrate, and no explicit
distinction between such a case and the oxide layer case will be made in this appendix.

B.1   Infinite Bulk, No Surface Layer(s)

Suppose that the incident neutron encounters a bulk sufficiently thick that the
wavefunction vanishes at $+\infty$. In this case, we can express the potential as an infinite step
function defined as zero for x<0 and $V(x) = \frac{2\pi\hbar^2}{m_N} N(a_R - ia_l) \equiv V - iW$ elsewhere, where
Na is the complex scattering length density. We can divide the wavefunction on these two

segments:

$$\Psi(x, y, z) = \begin{cases} \Psi_0(x, y, z) & if x < 0 \\ \\ \Psi_1(x, y, z) & if x \geq 0 \end{cases} \tag{B.1}$$

By setting the surface normal to be the x-direction, we know that the y and z components are both plane waves with the appropriate wavenumbers; these will not factor into the calculations. For each region, the potential is constant, and as such the Schrödinger equation takes the form:

$$\frac{\hbar^2}{2m} \frac{\partial^2 \Psi_j}{\partial x^2} + (E - V_j + iW_j)\Psi_j = 0 \tag{B.2}$$

This is easily solved for each region to give the wavefunction in terms of exponentials:

$$\Psi_0(x) = e^{ik_0 x} + Re^{-ik_0 x} \tag{B.3}$$

$$\Psi_1(x) = Te^{ik_1 x} \tag{B.4}$$

Where we have defined $k_j = \sqrt{\frac{2m}{\hbar^2}(E - V_j + iW_j)}$ and we have ignored the reflected wave component in the expression for $\Psi_1(x)$. The adjoints to these wavefunctions are easily found to be identical to the above equations with the substitutions $i \to -i$ and $k \to k^*$. The boundary (x=0) continuity equations are simple:

$$1 + R = T \tag{B.5}$$

$$ik_0(1 - R) = ik_1 T \tag{B.6}$$

96

$$R = \frac{2k_0}{k_1 + k_0} = \frac{2\sqrt{E}}{\sqrt{E} + \sqrt{E - V_1 + iW_1}} \tag{B.7}$$

$$T = \frac{k_1 - k_0}{k_1 + k_0} = \frac{\sqrt{E} - \sqrt{E - V_1 + iW_1}}{\sqrt{E} + \sqrt{E - V_1 + iW_1}} \tag{B.8}$$

To obtain the reflection and transmission probabilities, we consider the probability currents into andout of the boundary region $[-\epsilon, \epsilon]$. We can generally solve for the probability current for a plane wave Ae^{ikx} with complex k as:

$$\mathbf{j}_x(x) = \frac{\hbar}{2mi} \left(\Psi^\dagger \frac{\partial \Psi}{\partial x} - \Psi \frac{\partial \Psi^\dagger}{\partial x} \right) = \frac{\hbar}{m} |A|^2 \Re(k) e^{-2\Im(k)x} \tag{B.9}$$

We can identify the incoming wave as the normalized exponential term in Ψ_0, the reflected outgoing wave as the R term, and the transmitted outgoing wave as the T term. Then, the reflection and transmission probabilities p_R and p_T are easily found as:

$$p_R = \lim_{\epsilon \to 0} \left| \frac{\mathbf{j}_{ref}(-\epsilon) \cdot \hat{x}}{\mathbf{j}_{inc}(-\epsilon) \cdot \hat{x}} \right| = \left| \frac{|Q|^2 \Re(k_0)}{\Re(k_0)} \right| = \frac{|k_0 - k_1|^2}{|k_0 + k_1|^2} \tag{B.10}$$

$$p_T = \lim_{\epsilon \to 0} \left| \frac{\mathbf{j}_{trn}(\epsilon) \cdot \hat{x}}{\mathbf{j}_{inc}(-\epsilon) \cdot \hat{x}} \right| = \left| \frac{|S|^2 \Re(k_1)}{\Re(k_0)} \right| = \frac{4|k_0|^2}{|k_0 + k_1|^2} \tag{B.11}$$

Note that we always take the square root value with positive real part, and as such we can ignore the absolute value around the ratio of $\Re(k_i)$'s. It is easily verified that R+T=1. In cases in which the bulk has a high absorption probability such as Boron, we assume all transmitted particles are lost and interpret T as the loss per bounce.

There exists a particular mixture of boron-10 with boron-11 (specifically, 97.08% 10B), for which the real part of the potential vanishes. In this case, $V_B \equiv -iW' = -37.98i$ neV. Letting E/W = K, the reflectivity goes as $R = \left| \frac{1 - \sqrt{1 + i/K}}{1 + \sqrt{1 + i/K}} \right|^2$, which is a monotonically
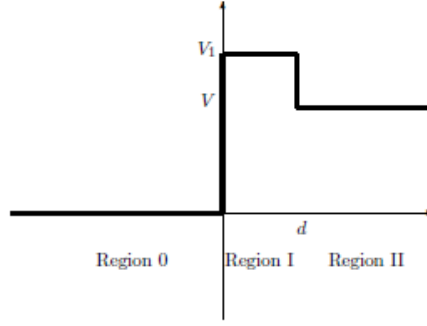
Figure B.1: General shape of a material boundary potential with a monolayer

decreasing curve that acts as $1 - \sqrt{8K}$ for $K \ll 1$ and $1/(16K^2)$ for $K \gg 1$.

B.2 Single Layer on Substrate

We next consider the previous case with an additional layer of thickness d between the vacuum and the bulk, where the bulk is treated as an infinite substrate and the monolayer thickness is small compared to the bulk. We can divide the potential into three regions, where the vacuum is region 0, the monolayer is region 1, and the substrate is region 2, as in Figure B.1.

With the regions defined ins this fashion, the wavefunction is expressed as :

$$\Psi(x,y,z) = \begin{cases} \Psi_0(x,y,z) & if \, x < 0 \\ \Psi_1(x,y,z) & if \, 0 \le x < d \\ \Psi_2(x,y,z) & if \, x \ge d \end{cases} \quad (B.12)$$

For a particle incident on the surface with an energy E_{total} and perpendicular energy $E = E_{total}\cos(\theta)$, we may construct the wavefunctions taking x as the surface normal

98

direction $\Psi(x, y, z) = \Psi(x)e^{ik_y y}e^{ik_z z}$, and subdivide by region:

$$\Psi_0(x) = e^{ik_0 x} + Re^{-ik_0 x} \tag{B.13}$$

$$\Psi_0(x) = Ae^{ik_1 x} + Be^{-ik_1 x} \tag{B.14}$$

$$\Psi_0(x) = Te^{ik_2(x-d)} \tag{B.15}$$

where, as before, $k_j = \sqrt{\frac{2m}{\hbar^2}(E - V_j + iW_j)}$. For regions where $E < V_j$, k_j will be imaginary, and so for those cases it may be helpful to define $\beta_j = -ik_j$ to simplify the expressions. The incoming wave amplitude has been normalized such that R and T correspond to reflection and transmission amplitudes as before.

We apply the continuity and smoothness boundary conditions at each point:

$$\Psi_0(0) = Psi_1(0) \implies 1 + R = A + B \tag{B.16}$$

$$\Psi_0'(0) = Psi_1'(0) \implies ik_0(1 - R) = ik_1(A - B) \tag{B.17}$$

$$\Psi_1(d) = Psi_2(d) \implies Ae^{ik_1 d} + Be^{-ik_1 d} = T \tag{B.18}$$

$$\Psi_1'(d) = Psi_2'(d) \implies ik_1\left(Ae^{ik_1 d} - Be^{-ik_1 d}\right) = ik_2 T \tag{B.19}$$

Solving for the coefficients in the latter two equations in terms of T yields $2A = (1 + k_2/k_1)\, Te^{-ik_1 d}$ and $2B = (1 - k_2/k_1)\, Te^{ik_1 d}$, which can be inserted into the former two equations to yield

$$2 = (A + B) + \frac{k_1}{k_0}(A - B) \tag{B.20}$$

$$= \left(1 + \frac{k_1}{k_0}\right)A + \left(1 - \frac{k_1}{k_0}\right)B \tag{B.21}$$

$$= \left[\left(1 + \frac{k_2}{k_0}\right)\frac{e^{ik_1 d} + e^{-ik_1 d}}{2} + \left(-\frac{k_1}{k_0} - \frac{k_2}{k_1}\right)\frac{e^{ik_1 d} - e^{-ik_1 d}}{2}\right]T \tag{B.22}$$

Which can be solved for T as:

$$T = \frac{2}{M\cos(k_1 d) + N\sin(k_1 d)}, \tag{B.23}$$

where $M = 1 + k_2/k_0$ and $N = -i(k_1/k_0 + k_2/k_1)$. We can abbreviate this result as $T = 2/D$, and conclude the transmission probability as $p_T = |T|^2 = 4/D^* D$.

The reflection amplitude is similarly derived from the difference of the x=0 boundary conditions. We can save some steps by noticing that this is the same as replacing $k_0 \to -k_0$.

$$2 = (A + B) - \frac{k_1}{k_0}(A - B) \tag{B.24}$$

$$= \left[\left(1 - \frac{k_2}{k_0}\right)\frac{e^{ik_1 d} + e^{-ik_1 d}}{2} + \left(\frac{k_1}{k_0} - \frac{k_2}{k_1}\right)\frac{e^{ik_1 d} - e^{-ik_1 d}}{2}\right]T \tag{B.25}$$

This yields, with the definitions $\widetilde{M} = 1 - k_2/k_1$ and $\widetilde{N} = i(k_1/k_0 - k_2/k_1)$,

$$R = \frac{\widetilde{M}\cos(k_1 d) + \widetilde{N}\sin(k1d)}{M\cos(k_1 d) + N\sin(k_1 d)} \tag{B.26}$$

From this, the reflection probability is $p_R = |R|^2 = \frac{\widetilde{D}^* \widetilde{D}}{D^* D}$. Note that R and T are both functions of E, and thus of both E_{total} and incidence angle θ. It is trivial to demonstrate

100

that this result reduces to the infinite layerless bulk case when $d \to 0$.

In addition to the reflection and transmission, is is useful to determine the loss factor η_L for the monolayer. This can be computed by integrating the probability function multiplied by cross section over region 1[14].

$$\eta_L = \int_0^d \left(|N\sigma_L|(x)\right) |\Psi_1(x)|^2 dx \tag{B.27}$$

In general, $N\sigma_L$ may be position dependent; for simplicity, we will assume a uniform structure to the monolayer. With this assumption, the only position dependence comes from the wavefunction. We previously solved for $Psi_1(x)$, and can introduce $K \equiv \frac{k_2}{k_1} = \sqrt{\frac{E-V}{E-V_1}}$. Note that K is either entirely real or entirely imaginary depending on UCN energy. If we swap the limits and define $x' = d - x$, the integrand becomes:

$$|\Psi_1(x')|^2 = \frac{T^2}{4} \left[(1+K^*)e^{ik_1^* x'} + (1-K^*)e^{-ik_1^* x'}\right] \left[(1+K)e^{-ik_1 x'} + (1-K)e^{ik_1 x'}\right] \tag{B.28}$$

$$= \frac{T^2}{4} \left[(1+|K|^2)\left(e^{2\Im(k_1)x'} + e^{-2\Im(k_1)x'}\right) + (K+K^*)\left(e^{2\Im(k_1)x'} - e^{-2\Im(k_1)x'}\right) + \right.$$

$$\left. +(1-|K|^2)\left(e^{2i\Re(k_1)x'} + e^{-2i\Re(k_1)x'}\right) + (K-K^*)\left(e^{2i\Re(k_1)x'} - e^{-2i\Re(k_1)x'}\right)\right] \tag{B.29}$$

$$= \frac{T^2}{4} \left[(1+|K|^2)\cosh(2\Im(k_1)x') + 2\Re(K)\sinh(2\Im(k_1)x') + \right.$$

$$\left. +(1-|K|^2)\cos(2\Re(k_1)x') - 2i\Im(K)\sin(2\Re(k_1)x')\right] \tag{B.30}$$

The reality of k_1 and k_2 strongly influence the form of this result, wiht multiple terms

dropping out depending on the energy. This expression is easily integrated to yield the loss:

$$\eta_L = \frac{N\sigma_L d}{|D|^2}\left[(1+|K|^2)\frac{\sinh(2\Im(k_1)d)}{\Im(k_1)d} + 2\Re(K)\frac{\cosh(2\Im(k_1)d)-1}{\Im(k_1)d} + \right.$$
$$\left. +(1-|K|^2)\frac{\sin(2\Re(k_1)d)}{\Re(k_1)d} + 2\Im(K)\frac{1-\cos(2\Re(k_1)d)}{\Re(k_1)d}\right] \tag{B.31}$$

Notice that the cos and cosh terms will vanish whenever k_2 is real. It is important to remember that σ_L is generally dependent on energy when performing a calculation.

In cases where the bulk has nonzero potential, we can compute the losses from this region based on our knowledge of $\Psi_2(x)$. In the event that $E > V$, any transmitted particle will propogate indefinitely through the bulk and in most calculations will be interpreted as having left the experimental volume; as such the probability of transmission is a component of the loss probability. Otherwise, if the energy is less than the bulk then we perform the loss calculation on a decaying exponential:

$$\eta_2 = N\sigma_L \int_d^\infty dx \left|Te^{-\beta_2(x-d)}\right|^2 = \frac{N\sigma_L d}{|D|^2}\frac{2}{\beta_2 d}. \tag{B.32}$$

B.3   Example Calculations for Monolayer Case

One way this calculation can be used is in the determination of the absorption of a UCN by a finite layer of boron, in which region 0 and 2 are both set to be vacuum and region 1 has the Fermi potential of the desired purity of boron-10. An alternate measurement can be made when region 2 is given the Fermi potential of ZnS to simulate the detector design outlined in Section 4.2. A subset of the results from the computation are shown in Figure 4.5.

Another use for this calculation is in the investigation of the effect of a passivation on the vanadium detector surface. Vanadium passivates by conversion to several species of oxides, with vanadium(IV) oxide (VO_2) being the most common. While other oxides may exist within the passivation layer, we can perform this calculation in the approximation of a uniform passivation. In this case, we consider region 2 to be the Vanadium ($V = V_F = -8.2neV$) and for the thickness to be functionally infinite for the sake of this calculation, and region 1 to be the oxide layer with $V_1 = V_F = 98.2$ neV. Since $E > V$ is guaranteed, there are only two distinct energy regimes to be considered, $E_\perp \in [0, V_1)$ and $E_\perp \in (V_1, \infty)$. The detection efficiency will therefore have an energy dependent factor proportional to p_T

If $E < V1$, then $k_1 = i\beta$ will be imaginary, and the trigonometric coefficients will be $M = 1 + \frac{k_2}{k_0}$ and $N = i(-frack_2\beta + \frac{\beta}{k_0}$. Thus, the transmission probability becomes:

$$|T_-|^2 = \frac{4}{\left(1 + \frac{k_2}{k_0}\right)^2 \cosh^2(\beta d) + \left(\frac{k_2}{\beta} - \frac{\beta}{k_0}\right)^2 \sinh^2(\beta d)} \tag{B.33}$$

There is no obvious analytical simplification, but this suffices for a numerical determination of the transmission.

If $E > V_1$, k is real for all regions, and we have $M = 1 + k_2/k_0$ and N $= -i(k2/k1 + k1/k0)$. This gives a transmission probability of:

$$|T_+|^2 = \frac{4}{\left(1 + \frac{k_2}{k_0}\right)^2 \cos^2(k_1 d) + \left(\frac{k_2}{k_1} + \frac{k_1}{k_0}\right)^2 \sin^2(k_1 d)} \tag{B.34}$$

Figure B.2 shows the plots of the transmission probabilities for VO_2 as well as several other monolayers on vanadium. For a sufficiently thin oxide layer, the transmission rises
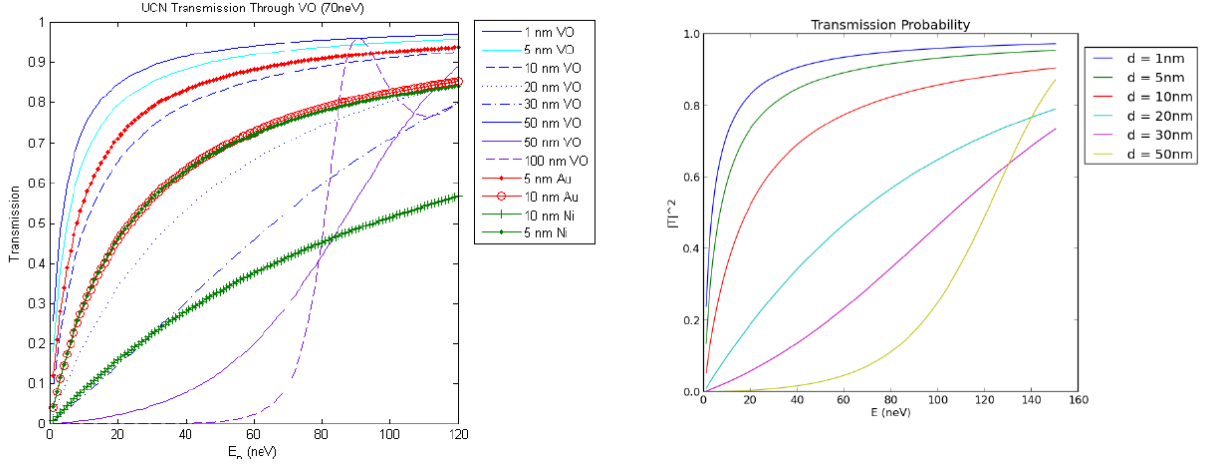
Figure B.2: Transmission vs energy for VO_2 oxide layer (right) and for several other types and thicknesses of coatings including VO (left)

quickly with incident energy and remains mostly above 90% absorption for most energies. Oxide layers thicker than about 5nm have more prominent energy dependence, which would increase detection efficiency coupling to UCN phase space; however, we do not expect the natural passivation to be as thick as that. Loss for films at the 5nm level peak at around 5neV with around 10^{-5} loss per bounce, which is comparable to or better than the other material surfaces in the transport guide system; most non-capture UCN are reflected from the oxide surface. As such, the energy dependence in UCN capture on the passivated vanadium leads to an energy dependent increase to the absorption time. Given the results of both simulations and experimental studies, this is not expected to influence the ability to accurately count the trapped UCN.

B.4 Multilayers

In the event that we must assess the influence of multiple thin layers on a substrate on the UCN reflection and loss properties, we can benefit from generalizing the calculation into a multilayer case. We define N regions of thickness d_n piecewise as before (See Figure B.3),
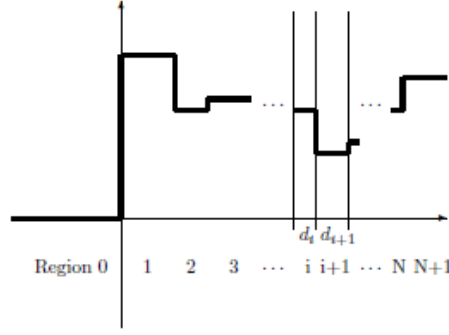
104

Figure B.3: General shape of a material boundary potential with a multilayer

with region 0 being free space and region N+1 being the material bulk. Each region has a corresponding k_n defined as usual, with a corresponding wavefunction $\Psi_n(x) = G_n e i k_n x + H_n e^{-ik_n x}$. This gives us 2N boundary conditions which can be solved for the desired coefficients. Let us denote the boundary positions as z_n such that region n consists of the interval (z_{n-1}, z_n). Then each boundary gives two equations:

$$G_{n+1} e^{ik_{n+1}z_n} + H_{n+1}e^{-ik_{n+1}z_n} = G_n e^{ik_n z_n} + H_n e^{-ik_n z_n} \tag{B.35}$$

$$G_{n+1} e^{ik_{n+1}z_n} - H_{n+1}e^{-ik_{n+1}z_n} = \frac{k_n}{k_{n+1}}\left(G_n e^{ik_n z_n} - H_n e^{-ik_n z_n}\right) \tag{B.36}$$

We can introduce 2×1 matrices $\begin{pmatrix} G_n \\ H_n \end{pmatrix}$ and solve the boundary condition equations to get a recurrence relation:

$$\begin{pmatrix} G_{n+1} \\ H_{n+1} \end{pmatrix} = M_n \begin{pmatrix} G_n \\ H_n \end{pmatrix} \tag{B.37}$$

where

$$M_n = \frac{1}{2}\begin{pmatrix} (1 + \frac{k_n}{k_{n+1}})e^{i(k_n - k_{n+1})z_n} & (1 - \frac{k_n}{k_{n+1}})e^{-i(k_n + k_{n+1})z_n} \\ (1 - \frac{k_n}{k_{n+1}})e^{i(k_n + k_{n+1})z_n} & (1 + \frac{k_n}{k_{n+1}})e^{-i(k_n - k_{n+1})z_n} \end{pmatrix} \tag{B.38}$$

The product of two or more M_n matrices is important for the transmission and reflection calculations, as will be clear later in the calculation. We define the product of the first n

matrices as:

$$\mathbb{M}_n = M_n \cdot M_{n-1} \cdots M_0 = \frac{1}{2} \begin{pmatrix} A_n & B_n \\ C_n & D_n \end{pmatrix} \tag{B.39}$$

It is wort noting that the determinant of each boundary matrix is $det(M_n) = k_n/k_{n+1}$, and therefore $det(\mathbb{M}_n) = k_0/k_{n+1}$.

It can be shown inductively that the general form of the matrix components of $\mathbb{M}_n$ are as follows. Suppose $\mathbf{N} = 1, 2, \ldots, m$ and $\mathbb{S} \subset \mathbf{N}$ is any ordered subset of indices

$(i < j \implies s_i < s_j)$ of $\mathbf{N}$. Recalling that $d_n = z_n - z_{n-1}$, the components are found as:

$$
A_n = e^{i(k_0 z_0 - k_{n+1} z_n)} \sum_{m=0}^{\lfloor n/2 \rfloor} \left[\sum_{|\mathbb{S}|=2m} \left(\prod_{s_j \in \mathbb{S}} k_{s_j}^{(-1)^{j+1}} + \frac{k_0}{k_{n+1}} \prod_{s_j \in \mathbb{S}} k_{s_j}^{(-1)^j} \right) \prod_{s \in \mathbb{S}} i \sin(k_s d_s) \prod_{c \notin \mathbb{S}} \cos(k_c d_c) + \right.
$$
$$
\left. + \sum_{|\mathbb{S}|=2m+1} \left(k_0 \prod_{s_j \in \mathbb{S}} k_{s_j}^{(-1)^j} + \frac{1}{k_{n+1}} \prod_{s_j \in \mathbb{S}} k_{s_j}^{(-1)^{j+1}} \right) \prod_{s \in \mathbb{S}} i \sin(k_s d_s) \prod_{c \notin \mathbb{S}} \cos(k_c d_c) \right] \quad \text{(B.40)}
$$

$$
B_n = e^{-i(k_0 z_0 + k_{n+1} z_n)} \sum_{m=0}^{\lfloor n/2 \rfloor} \left[\sum_{|\mathbb{S}|=2m} \left(\prod_{s_j \in \mathbb{S}} k_{s_j}^{(-1)^{j+1}} - \frac{k_0}{k_{n+1}} \prod_{s_j \in \mathbb{S}} k_{s_j}^{(-1)^j} \right) \prod_{s \in \mathbb{S}} i \sin(k_s d_s) \prod_{c \notin \mathbb{S}} \cos(k_c d_c) + \right.
$$
$$
\left. + \sum_{|\mathbb{S}|=2m+1} \left(-k_0 \prod_{s_j \in \mathbb{S}} k_{s_j}^{(-1)^j} + \frac{1}{k_{n+1}} \prod_{s_j \in \mathbb{S}} k_{s_j}^{(-1)^{j+1}} \right) \prod_{s \in \mathbb{S}} i \sin(k_s d_s) \prod_{c \notin \mathbb{S}} \cos(k_c d_c) \right] \quad \text{(B.41)}
$$

$$
C_n = e^{i(k_0 z_0 + k_{n+1} z_n)} \sum_{m=0}^{\lfloor n/2 \rfloor} \left[\sum_{|\mathbb{S}|=2m} \left(\prod_{s_j \in \mathbb{S}} k_{s_j}^{(-1)^{j+1}} - \frac{k_0}{k_{n+1}} \prod_{s_j \in \mathbb{S}} k_{s_j}^{(-1)^j} \right) \prod_{s \in \mathbb{S}} i \sin(k_s d_s) \prod_{c \notin \mathbb{S}} \cos(k_c d_c) + \right.
$$
$$
\left. + \sum_{|\mathbb{S}|=2m+1} \left(k_0 \prod_{s_j \in \mathbb{S}} k_{s_j}^{(-1)^j} - \frac{1}{k_{n+1}} \prod_{s_j \in \mathbb{S}} k_{s_j}^{(-1)^{j+1}} \right) \prod_{s \in \mathbb{S}} i \sin(k_s d_s) \prod_{c \notin \mathbb{S}} \cos(k_c d_c) \right] \quad \text{(B.42)}
$$

$$
D_n = e^{-i(k_0 z_0 - k_{n+1} z_n)} \sum_{m=0}^{\lfloor n/2 \rfloor} \left[\sum_{|\mathbb{S}|=2m} \left(\prod_{s_j \in \mathbb{S}} k_{s_j}^{(-1)^{j+1}} + \frac{k_0}{k_{n+1}} \prod_{s_j \in \mathbb{S}} k_{s_j}^{(-1)^j} \right) \prod_{s \in \mathbb{S}} i \sin(k_s d_s) \prod_{c \notin \mathbb{S}} \cos(k_c d_c) + \right.
$$
$$
\left. + \sum_{|\mathbb{S}|=2m+1} \left(-k_0 \prod_{s_j \in \mathbb{S}} k_{s_j}^{(-1)^j} - \frac{1}{k_{n+1}} \prod_{s_j \in \mathbb{S}} k_{s_j}^{(-1)^{j+1}} \right) \prod_{s \in \mathbb{S}} i \sin(k_s d_s) \prod_{c \notin \mathbb{S}} \cos(k_c d_c) \right] \quad \text{(B.43)}
$$

It is possible that these expressions may be further simplified; however, this sufficiently provides a closed form for any $n > 0$. It is worth mentioning that the case where $n = N$, the boundary conditions are such that $H_{n+1} = 0$ (that is, there is no backwards propagating wave from $+\infty$). As a result, we may freely neglect the exponential factor in this final case. To verify these forms, we consider the calculation of the first boundary matrix $\mathbb{M}_0 = M_0$. Substituting n=0 into the above formulae, all products are empty

products and no set $\mathbb{S}$ exists with odd size. In this case, the values returned are:

$$
\begin{aligned}
A_0 &= e^{i(k_0 z_0 - k_1 z_0)} \left(1 + \frac{k_0}{k_1} \right) \\
B_0 &= e^{-i(k_0 z_0 + k_1 z_0)} \left(1 - \frac{k_0}{k_1} \right) \\
C_0 &= e^{i(k_0 z_0 + k_1 z_0)} \left(1 - \frac{k_0}{k_1} \right) \\
D_0 &= e^{-i(k_0 z_0 - k_1 z_0)} \left(1 + \frac{k_0}{k_1} \right)
\end{aligned}
\tag{B.44}
$$

which is exactly the matrix derived in Equation B.38.

Now that we have derived a closed expression for the boundary transfer matrices, we can easily relate any given coefficient matrix with that of free space:

$$
\begin{pmatrix} G_{n+1} \\ H_{n+1} \end{pmatrix} = \mathbb{M}_n \begin{pmatrix} G_0 \\ H_0 \end{pmatrix} = \mathbb{M}_n \begin{pmatrix} 1 \\ R \end{pmatrix}
\tag{B.45}
$$

In particular, we can write the equation for the bulk coefficients in order to determine T:

$$
\begin{pmatrix} G_{N+1} \\ H_{N+1} \end{pmatrix} = \begin{pmatrix} T \\ 0 \end{pmatrix} = \mathbb{M}_N \begin{pmatrix} 1 \\ R \end{pmatrix}
\tag{B.46}
$$

Multiplying out the matrix on the right, we have:

$$
\begin{pmatrix} T \\ 0 \end{pmatrix} = \frac{1}{2} \begin{pmatrix} A_N + B_N R \\ C_N + D_N R \end{pmatrix}
\tag{B.47}
$$

which yields:

$$T = \frac{2k_0}{k_{N+1} D_N} \tag{B.48}$$

$$R = \frac{-C_N}{D_N} \tag{B.49}$$

The loss can also be computed using the expressions for the intermediate coefficients. Using Equation B.27, we have for each region:

$$
\begin{aligned}
\eta_n =& N\sigma \int_{z_{n-1}}^{z_n} \left(G_n^* e^{-ik_n^* x} + H_n^* e^{ik_n^* x} \right) \left(G_n e^{-ik_n x} + H_n e^{-ik_n x} \right) dx \\
=& N\sigma \int_{z_{n-1}}^{z_n} dx \left(|G_n|^2 e^{-2\Im(k_n)x} + |H_n|^2 e^{2\Im(k_n)x} + 2\Re \left[G_n^* H_n e^{-2i\Re(k_n)x} \right] \right) \\
=& N\sigma \left(\left(|G_n|^2 e^{-\Im(k_n)(z_n + z_{n+1})} + |H_n|^2 e^{2\Im(k_n)(z_n + z_{n+1})} \right) \frac{\sinh(\Im(k_n)d_n)}{\Im(k_n)} + \right. \\
& + \Re(H_n^* G_n) \frac{\sin(2\Re(k_n)z_n) - \sin(2\Re(k_n)z_{n-1})}{\Re(k_n)} + \\
& \left. + \Im(H_n^* G_n) \frac{\cos(2\Re(k_n)z_n) - \cos(2\Re(k_n)z_{n-1})}{\Re(k_n)} \right)
\end{aligned}
\tag{B.50}
$$

The loss is then just the sum over the loss for each region.

B.5 Multilayer Example - Passivated Copper

Much of the transport guide system utilizes copper surfaces, which passivate into a double oxide layer consisting of a 2.0 nm inner layer of Cu_2O ($V_F = 139.6$ neV) and a 1.3 nm outer layer of CuO ($V_F = 168.3$ neV). It is possible to compute the UCN interaction properties analytically, however, the calculation is lengthy and will be omitted in favor of presenting the results directly. Based on this model of multilayer interaction, we compute energy dependent reflection and loss curves, seen in Figure ??. The energy dependence of
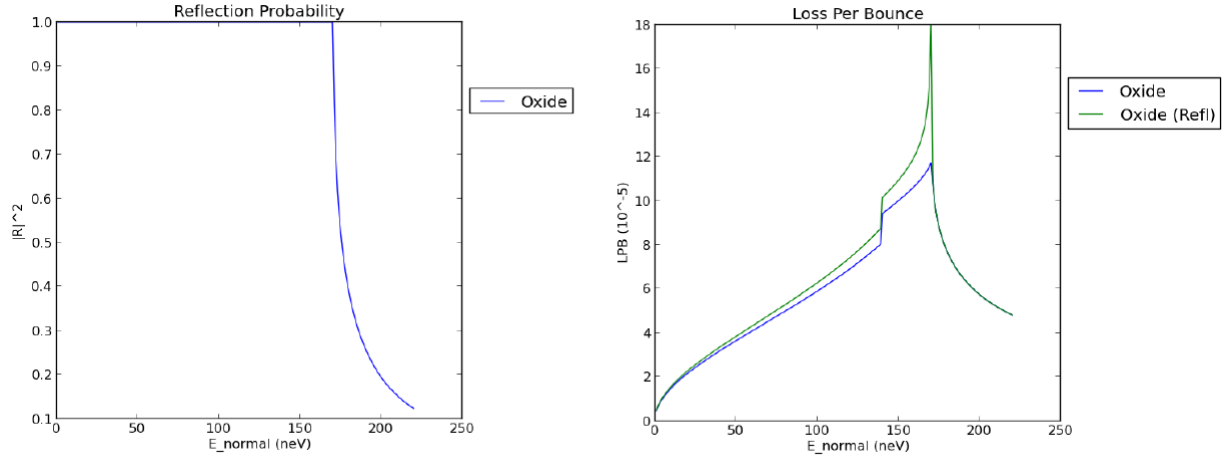
Figure B.4: Reflection and loss per bounce of UCN from passivated copper as a function of incident energy. In the LPB plot, the blue curve represents only the UCN lost in the oxide layer while the green curve includes loss by transmission into the substrate.

the loss per bounce is of particualr note given its strong dependence on energy, particularly at energies between 140 and 170 neV, the Fermi potentials of the oxide layers. These results can be applied to the Geant4 calculation of wall interactions to determine the effect of passivation on transport efficiency.

CURRICULUM VITAE

EDUCATION

Indiana University, Bloomington, IN   8/2010 – 4/2017

Ph.D. in Nuclear Physics

Thesis: Measurement of the Neuton Beta Decay Lifetime Using Magnetically Trapped

 Ultracold Neutrons

Advisor: Chen-Yu Liu

North Carolina State University, Raleigh, NC   8/2006 – 5/2010

B.S. in Physics, B.S. in Mathematics

Thesis: Nanoscale-defined, in-plane oriented molecular deposition

Advisor: Hans Hallen

RESEARCH EXPERIENCE

Research Assistant under Chen-Yu Liu, Indiana University.   5/2011 – 4/2017

   Storage measurement of the free neutron beta decay lifetime using ultracold neutrons

   at the Los Alamos Neutron Science Source at Los Alamos National Laboratory, with

   focus on data analysis and simulation.

Undergraduate Research under Albert Young, N.C. State University   5/2010 – 7/2010

   Modeling the efficiency of scintillation detectors for the UCNA Experiment.

Undergraduate Research under Hans Hallen, N.C. State University   1/2007 – 5/2010

Development of electronic devices through molecular deposition using near-field scanning optical microscopy.

NSF-REU Program under Chung Kao, University of Oklahoma $\qquad$ 5/2009 – 7/2009

Developed MadGraph/MadEvent analysis simulation for investigating detection of Higgs-moderated tau decays.

PUBLICATIONS

"A multilayer surface detector for ultracold neutrons"

Z. Wang, et al., Nucl. Instrum. Methods Phys. Res. A 798, 30-35 (2015).

"Storage of ultracold neutrons in the magneto-graviational trap of the UCN experiment"

D. J. Salvat, et al., Phys. Rev. C 89, 5 (2014).

"Upscattering ultracold neutrons from the polymer [C6H12]n"

E. I. Shapirov et al., Phys. Rev. C 88, 6 (2013).

"Measurements of ultracold neutron upscattering and absorption in polyethylene and vanadium"

E. I. Shapirov et al., Phys. Rev. C 88, 3 (2013).

"A boron-coated ionization chamber for ultra-cold neutron detection"

D.J. Salvat, et al., Nucl. Instrum. Methods Phys. Res. A 691, 109-112 (2012).

PRESENTATIONS

NIST, Gaithersburg, MD, Invited Talk $\qquad$ 28 Feb 2017

"An Improved Ultracold Neutron Bottle for Measuring the Neutron Lifetime"

Brookhaven National Laboratory, Upton, NY, Invited Talk $\qquad$ 10 Nov 2016

"An Improved Ultracold Neutron Bottle for Measuring the Neutron Lifetime"

APS Division of Nuclear Physics Fall Meeting 2015, Santa Fe, NM $\qquad$ 31 Oct 2015

"Analysis of the 2014-2015 Neutron Lifetime Data from the UCN Experiment"

APS April Meeting 2015, Baltimore, MD   13 Apr 2015

   "Overview of the UCNτ Experiment"

APS Division of Nuclear Physics Fall Meeting 2013, Newport News, VA   24 Oct 2013

   "Simulation of UCN Transport in the UCN Experiment"

APS Division of Nuclear Physics Fall Meeting 2012, Newport Beach, CA   26 Oct 2012

   "Neutron Tracking Simulation for the UCN Experiment"

TEACHING EXPERIENCE

   PHYS-P202L – General Physics II Lab Teaching Assistant, Indiana University   8/2010
–12/2010

   PHYS-P201L – General Physics I Lab Teaching Assistant, Indiana University   1/2011 –
5/2011

   MA 114 – Introduction to Finite Mathematics Grader, NC State University   1/2010 –
5/2010

   MA 241 – Calculus II Undergraduate Lecture Assistant, NC State University   8/2009 –
12/2009

   Ross Mathematics Program – Counselor/Instructor, Ohio State Univeristy   5/2007 –
7/2007

                                                                5/2008 7/2008

HONORS and AWARDS

   Indiana University College of Arts and Sciences Travel Award (2015)

   Valedictorian, North Carolina State University (2010)

   NCSU Undergraduate Research Grant (2009)

NCSU 2nd Place in W. L. Putnam Mathematical Competition (2009)

NCSU Study Abroad Merit Scholarship (2008)

John W. Cell Memorial Scholarship (2008)

PROFESSIONAL MEMBERSHIPS

Member, American Physical Society (2010)

Member, Phi Beta Kappa (2009)

Member, Sigma Pi Sigma (2009)